Numerical design of an optical solid-state amplifier

by

Gysbert Johannes van der Westhuizen

Thesis presented in partial fulfillment of the requirements
for the degree of

Master of Science

at the University of Stellenbosch

Supervisor:
Dr. J.P. Burger
Co-supervisor:
Prof. E.G. Rohwer

December 2007

Declaration

I, the undersigned, hereby declare that the work contained in this thesis is my own original work and that I have not previously in its entirety or in part submitted it at any university for a degree.

.....

Signature

.....

Date

Abstract

Theoretical models fulfill an important role in the field of laser research as a result of the time and money required to perform an experiment. In particular, theoretical models may be used as tools in the design of more efficient laser systems and contribute to a better understanding of the physical processes influencing laser media. In the work presented, a solid-state amplifier is modeled according to well known theory for the purpose of designing an amplifier stage, to be used as part of a hybrid fibre-bulk laser system.

Various processes have an influence on the quality of a laser material and only a number of them can realistically be included in a model. Two processes were specifically investigated in this work. The first process is that of amplified spontaneous emission (ASE), whereby the population inversion of a laser material is decreased. The second process involves the nature of beam propagation and is of importance for the precise modeling of light-matter interaction. The background theory and procedures followed to take account of the above mentioned processes are discussed.

The model equations were numerically solved for the case of continuous wave (CW) probe amplification as well as the case of pulsed probe amplification. An experiment was conducted, using readily available equipment, for the purpose of verifying the CW model, whilst the pulse model was validated by means of an analytical approach. In both cases the agreement between the simulated results and those obtained from experiment or theory was acceptable. Possible shortcomings within the models are identified.

Finally the models were used for the design of an Yb:YAG amplifier. The optimum crystal characteristics were identified and the thermal properties of the crystal were evaluated. With limited equipment, a qualitative analysis of the optimum crystal was performed by means of an experimental investigation. The investigation confirmed the CW model as a potential design tool. Improvements to the CW and pulse models are suggested and may lead to additional experiments.

Opsomming

Teoretiese modelle vervul 'n belangrike rol in die veld van laser navorsing as gevolg van die tyd en geld wat benodig word vir die uitvoer van 'n eksperiment. In die besonder kan teoretiese modelle gebruik word as gereedskap in die ontwerp van meer doeltreffende laser sisteme en kan ook bydra tot 'n beter begrip van die fisiese prosesse wat inwerk op 'n laser medium. Die navorsing wat hier voorgedra word, behels die modelering van 'n vaste-toestand, optiese versterker volgens wel bekende teorie met die doel om 'n versterker wat deel vorm van 'n hibried vesel-vaste-toestand laser sisteem te ontwerp.

Verskeie prosesse beïnvloed die kwaliteit van 'n laser materiaal en slegs sekere hiervan kan realisties in 'n model ingesluit word. Twee spesifieke prosesse was as prioriteit beskou in hierdie navorsing. Die eerste proses genaamd, versterkte spontane emissie (ASE), is 'n proses wat lei tot die afname in die populasie inversie van die laser materiaal. Die tweede proses behels die voortplantings kenmerke van 'n lig bundel en is van belang vir die akkurate modelering van die interaksie tussen lig en 'n voorwerp. Die teorie en die maatreëls wat gevolg is om beide bo-genoemde prosesse in te reken, word bespreek.

Die model vergelykings is numeries opgelos vir die versterking van 'n kontinue intree bundel (CW) en vir die versterking van 'n gepulsde intree bundel. 'n Eksperiment met die doel op die verifikasie van die CW model is uitgevoer deur gebruik te maak van beskikbare toerusting, terwyl 'n analitiese benadering gevolg is om die puls model te ondersoek. In beide gevalle is die ooreenstemming tussen die gesimuleerde resultate en die resultate wat deur middel van die eksperiment of analitiese benadering verkry is, bevredigend. Moontlike tekortkominge in die model is geïdentifiseer.

Die modelle is ten slotte gebruik in die ontwerp van 'n Yb:YAG versterker. Die optimale kristal karakteristieke is geïdentifiseer, waarna die kristal se termiese eienskappe ontleed is. 'n Kwalitatiewe ondersoek na die optimale kristal is deur middel van 'n eksperimentele opstelling bewerkstellig. Die ondersoek het die CW model as 'n potensiële gereedskap stuk, in die ontwerp van versterkers, bevestig. Verbeteringe aan die CW, asook die pulsmodel word voorgestel en kan lei tot verdere eksperimente.

Acknowledgments

I would like to thank the following people:

- Dr. J.P. Burger for his supervision of this work and countless useful discussions.
- Prof. E.G. Rohwer for contributing his knowledge and experience to the project.
- Dr. J-N Maran for his guidance and inspiring approach to research.
- Mr. A.S. Botha and Mr. E. Shields for their technical assistance.
- Mr. D. Spangenberg for the source code of a ray tracing algorithm used in this work.
- My fellow students, especially Gurthwin Bosman and Pieter Neethling, who listened to all my problems.
- Miss F.H. Mountfort and Miss M. Van Zyl who took the time to read this thesis.
- My parents for their support and patience.
- Last, but not least, Marguerite for her love and countless airplane tickets.

My M.Sc studies were funded by the National Research Foundation (NRF) and DefenceTek (CSIR).

Contents

List of Figures

List of Tables

Introduction

The continuous search for better materials and a more comprehensive understanding of the underlying principles in the field of lasers and optics relies on two methods. The first and historically primary method of evaluating a material and its properties is an experiment. Experimental investigations are very good in the sense that they give an exact account of the physical processes governing the material. Often it is difficult to identify the relative significance of the processes influencing a specific experiment. In addition, the experimental evaluation of a number of materials is not always practical due to the high cost of such materials and the time it takes to manufacture them. As a result of such difficulties, the second method of evaluating a material, a theoretical model, plays an important role in the research environment. Apart from the fact that theoretical models can be implemented as tools in the design of laser materials for specific purposes, the models also lead to an improved understanding of the processes governing the usefulness of a material. The use of theoretical models is common in the literature and finds application in various branches of laser physics. Optical amplifiers specifically have received much attention in the fields of semiconductor science [1, 2, 3, 4], fibre optics [5] and solid-state (SS) laser engineering, in both the single [6, 7] and multi-pass [8] regimes. As far as lasers are concerned, theoretical models similarly continue to contribute to semiconductor science [9] as well as SS engineering [10]. Although numerical methods are often used to solve the equations governing the dynamics inside the laser materials, analytical solutions are available under certain assumptions [11, 12].

The work presented in this thesis forms part of a project dedicated to the development of a laser system in the pulsed regime. The laser system is required to deliver ps-pulses with an energy per pulse in the mJ-range and a repetition rate of at least 1 kHz. The pulsed probe beam is provided by a fibre oscillator (Yb:glass). Fibre lasers have a number of advantages over conventional bulk SS lasers. Due to a large surface-to-volume ratio, fibre lasers dissipate heat very effectively and require no external cooling. In addition, fibre lasers are compact with high mechanical stability and produce outputs with exceptional beam quality. The disadvantages of fibre lasers are high non-linear effects and the possibility of optical damage, arising from the large intensities within the small fibre core [13]. It was decided to use a SS amplifier (Yb:YAG) to scale the output from the fibre oscillator up to the mJ-range. Solid-state amplifiers have energy storage capacities superior to that of fibre lasers and are frequently used to achieve high energy pulses [13]. Yb:YAG is preferred as laser material due to its properties contributing to high pulse energies and has been the subject of numerical analysis for some time now, whether as a laser [14, 15] or amplifier [16, 17].

The excellent thermal properties and bandwidth of Yb:YAG enables the generation of ps-pulses at high repetition rates. Although materials such as Nd:glass or Ti:Sapphire are widely used for short pulse generation, the low thermal conductivity associated with Nd:glass and the low laser efficiency of Ti:Sapphire deems it necessary to investigate other materials.

In contribution to the development of this hybrid fibre-bulk laser system, the research presented here is aimed at the design of a SS amplifier.
The design is based on a numerical approach, whereby the population rate equations are solved using a Runga-Kutta method. The numerical calculations are executed in MATLAB. Although the continuous wave (CW) scenario has been a priority, solutions to the time-dependent equations are obtained by means of a finite difference method. The purpose of the numerical design is two-fold. The first purpose is to develop a design tool capable of predicting the gain that can be expected from a certain SS amplifier under given boundary conditions, whilst the second is to investigate the influence of amplified spontaneous emission (ASE) at high gain.

In Chapter 1 the theory leading up to the population rate equations is discussed with emphasis on the assumptions used in the derivation. Chapter 2 shows the manipulation of the population rate equations to account for additional effects and also describes the algorithms on which the various models are based. The validity of the models are evaluated in Chapter 3, making use of experimental procedures as well as known analytical solutions. The models are applied to the design of an optimum Yb:YAG crystal in Chapter 4, also serving as final verification of the simulation algorithm.

Chapter 1

The semi-classical approach to light-matter interaction

The design of any laser or amplifier requires a fundamental understanding of the way in which light and matter interacts. The purpose of this chapter is to briefly illustrate the most important aspects of the theory eventually leading to the population rate equations. The light-matter interaction will be explained at the hand of the semi-classical approach. This means that the light (electromagnetic wave) is described classically (Maxwell), whilst the matter is described quantum mechanically. For the most part, the approach of Milonni and Eberly [18] shall be followed.

1.1 The wave equation

When dealing with electromagnetic fields, the most fundamental description is given by Maxwell's equations. By using simple vector calculus, the inhomogeneous wave equation results from rewriting Maxwell's equations for a neutral dielectric medium and assuming that the medium is non-magnetic.

$$\nabla^2 \vec{E} - \frac{1}{c^2}\frac{\partial^2 \vec{E}}{\partial t^2} = \frac{1}{\epsilon_0 c^2}\frac{\partial^2 \vec{P}}{\partial t^2} \tag{1.1}$$

$\vec{E}$ and $\vec{P}$ denotes the electric field and the polarization (also called the dipole moment density) respectively, whilst c is the velocity of light in vacuum.

The inhomogeneous wave equation is satisfied by transverse fields (fields transverse to the propagation direction). An example of a transverse field is a monochromatic plane wave of single frequency ω and amplitude E_0 which are independent of t or z (time and space coordinate in propagation direction).

$$\vec{E} = \hat{\varepsilon} E_0 \cos\omega\left(t - n(\omega)\frac{z}{c}\right) \tag{1.2}$$

The unit vector $\hat{\varepsilon}$ indicates the orientation of the polarization for this monochromatic plane wave and $n(\omega)$ is the refractive index of the medium at the frequency specified by ω.

1.2 Classical picture of absorption

Prior to the development of quantum mechanics, the theory that was used to predict an atom's interaction with an external electromagnetic field is called the electron oscillator model. The electron oscillator model (Lorentz model) makes use of the dipole approximation and basically comprises of Newton's equation of motion for the relative electron-nucleus displacement coordinate ($\vec{x}$) subject to a binding force $\vec{F}_{en}$ (exerted by the presumably stationary nucleus on the electron) as well as the Lorentz force $\vec{F} = e\vec{E}$ (describing the interaction of the charged electron with the external field). Asserting that the binding force may be modeled according to a spring with constant k_s, the Lorentz-model equation is given by:

$$m\frac{d^2\vec{x}}{dt^2} = e\vec{E}\left(\vec{R},t\right) - k_s\vec{x} \tag{1.3}$$

The parameters m and $\vec{R}$ denote the reduced mass and centre of mass of the electron-nucleus system, respectively.

When the equation of motion, given in equation 1.3, is subject to a frictional force, caused by inter-atomic elastic collisions, it is found that the dipoles (electron-nucleus pairs) experience a phase lag relative to that of the driving field. The phase lag effectively dampens the dipoles' oscillations. Solving the Lorentz-model equation including damping, for nearly resonant radiation (the field frequency ω corresponds to a natural oscillation frequency of the atom ω_0), leads to the classical theory of absorption. According to the classical theory of absorption the intensity of the external field exponentially decays to zero with propagation distance at a rate proportional to the absorption coefficient. Although the classical theory of absorption correctly describes the lineshape broadening with respect to the absorption coefficient's dependence on frequency (in the presence of damping), a parameter f, called the oscillator strength, has to be assigned to each natural oscillation frequency of the medium to compensate for discrepancies between the theory and experiment.

1.3 Quantum mechanical description of matter

The purpose of this section is to describe a theory able to predict how matter responds to an external electromagnetic field. Specifically of interest is the transitions an atomic medium can undergo when subject to such an external field. Due to the statistical nature of quantum mechanics, one can only assign a probability or expectation value for a system to be found in a discrete energy state. Using the time-dependent Schrödinger equation as starting point, the mathematical structure and assumptions necessary to arrive at the probability amplitudes are explained. The probability amplitudes play an important role in the derivation of the population rate equations.

1.3.1 The time-dependent Schrödinger equation

The Schrödinger equation for a particle in a time-independent potential $V(\vec{r})$ is given by

$$i\hbar\frac{\partial \mathbf{\Psi}}{\partial t} = \left[-\frac{\hbar^2}{2m}\nabla^2 + V(\vec{r})\right]\mathbf{\Psi} \tag{1.4}$$

where $\hbar = h/2\pi$ is Planck's constant and the wave function is labeled $\mathbf{\Psi}$. The solutions to equation 1.4 are of the form

$$\mathbf{\Psi}(\vec{r},t) = \mathbf{\Phi}(\vec{r})\, e^{-iEt/\hbar} \tag{1.5}$$

where the space dependent functions, $\mathbf{\Phi}(\vec{r})$, are called the stationary states. The scalar E simply represents the allowed energy states of the particle. The stationary states must satisfy the time-independent Schrödinger equation, with $\hat{H}$ denoting the Hamiltonian (operator representing the kinetic and potential energy of the particle).

$$\hat{H}\mathbf{\Phi}(\vec{r}) = E\mathbf{\Phi}(\vec{r}) \tag{1.6}$$

Every stationary state is associated with a specific energy and a specific the probability density of the particle in space.

When a particle finds itself in an external time-dependent potential ($V_{ext}(\vec{r},t)$), a new Hamiltonian may be defined as,

$$\hat{H} = \hat{H}_a + V_{ext}(\vec{r},t) \tag{1.7}$$

where $\hat{H}_a$ is the atomic (unperturbed particle's) Hamiltonian. For a Hamiltonian defined by equation 1.7 the time-dependent Schrödinger equation is given by:

$$i\hbar\frac{\partial \mathbf{\Psi}}{\partial t} = \left[-\frac{\hbar^2}{2m}\nabla^2 + V(\vec{r}) + V_{ext}(\vec{r},t)\right]\mathbf{\Psi} \tag{1.8}$$

Due to the completeness of the functions $\mathbf{\Phi}_n(\vec{r})$, a solution to the wave function satisfying the time-dependent Schrödinger equation may be expressed as a linear combination of the stationary states.

$$\mathbf{\Psi}(\vec{r},t) = \sum_n a_n(t)\,\mathbf{\Phi}_n(\vec{r}) \tag{1.9}$$

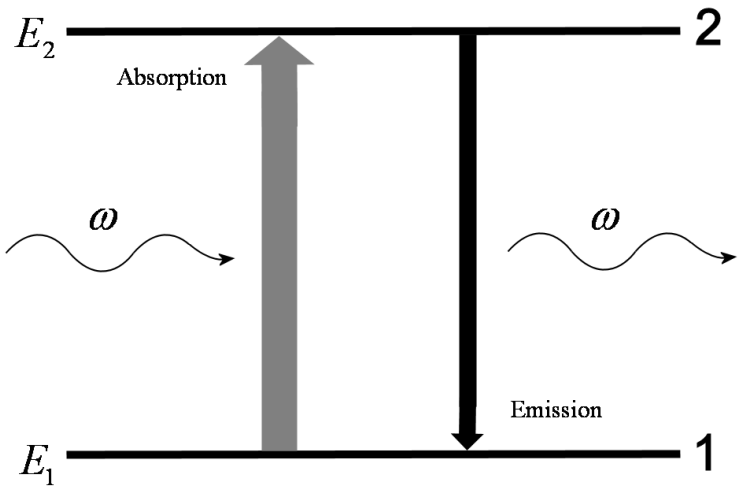

Figure 1.1: The processes of absorption and emission for a two-state atom having $\Delta E = \hbar\omega$.

Equation 1.9 requires the solutions to the time-dependent coefficients $a_n(t)$, known as probability amplitudes.

1.3.2 A two-state quantum system

When a monochromatic plane wave of frequency ω is incident upon an atom with two electronic energy levels such that $\Delta E = E_2 - E_1 = \hbar\omega$, a photon will be absorbed. Conversely, if for some reason the atom's energy is decreased from E_2 to E_1, a photon of energy $E = \hbar\omega$ will be emitted (Figure 1.1).

Since only two states are assumed, the probability of the atom being in any one of the two states should be unity:

$$|a_1(t)|^2 + |a_2(t)|^2 = 1 \tag{1.10}$$

From equation 1.9 the wave function for this two-state system is given by:

$$\mathbf{\Psi}(\vec{r},t) = a_1(t)\,\mathbf{\Phi}_1(\vec{r}) + a_2(t)\,\mathbf{\Phi}_2(\vec{r}) \tag{1.11}$$

The solution to the wave function given by equation 1.11 is now substituted into equation 1.8.

After using the time-independent Schrödinger equation together with the fact that the functions $\mathbf{\Phi}_n(\vec{r})$ are orthogonal, a time-dependent Schrödinger equation for each of the states arises[1]:

$$\begin{aligned} i\hbar\dot{a}_1(t) &= E_1 a_1(t) + V_{12} a_2(t) \\ i\hbar\dot{a}_2(t) &= E_2 a_2(t) + V_{21} a_1(t) \end{aligned} \tag{1.12}$$

The symbols V_{12} and V_{21} denote the matrix elements of the external potential arising from the electromagnetic field. Although there are two more matrix elements for this system (V_{11} and V_{22}), they are required to be zero by the parity selection rule. In the electric dipole approximation every matrix element $V_{ab}(t)$ is related to the electric field (in complex notation) by[2]

$$V_{ab}(t) = -e\vec{r}_{ab} \cdot \frac{1}{2}\left(\hat{\varepsilon} E_0 e^{-i\omega t} + \text{complex conjugate}\right) \tag{1.13}$$

where $\vec{r}_{ab}$ is known as the coordinate matrix element for the electron displacement (see $\vec{x}$ in Lorentz model). The equations in 1.12 may be therefore be rewritten as[3]:

$$\begin{aligned} i\dot{a}_1(t) &= -\frac{1}{2}\left(\chi_{12} e^{-i\omega t} + \chi_{21}^* e^{i\omega t}\right) a_2(t) \\ i\dot{a}_2(t) &= \omega_{21} a_2(t) - \frac{1}{2}\left(\chi_{21} e^{-i\omega t} + \chi_{12}^* e^{i\omega t}\right) a_1(t) \end{aligned} \tag{1.14}$$

The frequency corresponding to the energy of the upper state has been defined as $\omega_{21} = E_2/\hbar$ (assuming E_1 to be the ground state), while $\chi_{ab} = e(\vec{r}_{ab} \cdot \hat{\varepsilon}) E_0/\hbar$ is defined as the Rabi frequency.

Due to the fact that absorption takes place whenever the external field is resonant to the natural oscillation frequency, the case for which $\omega \approx \omega_{21}$ is of specific interest. The trial solutions $a_1(t) = c_1(t)$ and $a_2(t) = c_2(t) e^{-i\omega t}$ allow the time-dependent Schrödinger equations to be rewritten as:

$$\begin{aligned} i\dot{c}_1(t) &= -\frac{1}{2}\left(\chi_{12} e^{-2i\omega t} + \chi_{21}^*\right) c_2(t) \\ i\dot{c}_2(t) &= (\omega_{21} - \omega) c_2(t) - \frac{1}{2}\left(\chi_{21} + \chi_{12}^* e^{2i\omega t}\right) c_1(t) \end{aligned} \tag{1.15}$$

The rotating-wave approximation states that the terms described by $e^{\pm 2i\omega t}$ may now be taken to average to zero, since their variation with time is so rapid in comparison to that of the other terms.

[1] The mathematical notation of a dot is used to indicate the time derivative of the quantity a.
[2] The subscripts a and b refer to 1 and 2 or vice versa.
[3] An asterisk is used to indicate a quantity's complex conjugate.

If one takes $\chi = \chi_{21}$ and define the detuning from resonance as $\Delta = \omega_{21} - \omega$, the final form of the time-dependent Schrödinger equations are given by:

$$\begin{aligned} i\dot{c}_1(t) &= -\frac{1}{2}\chi^* c_2(t) \\ i\dot{c}_2(t) &= \Delta c_2 - \frac{1}{2}\chi c_1(t) \end{aligned} \tag{1.16}$$

1.3.3 The density matrix

Using the definition of the expectation value and the solution to the two-state system's wave function, the quantum mechanical electron displacement is found to be:

$$\begin{aligned} \langle\vec{r}\rangle &= \int_{\text{all space}} \mathbf{\Psi}^\star(\vec{r},t)\,\vec{r}\mathbf{\Psi}(\vec{r},t)\,d^3r \\ &= \int_{\text{all space}} (a_1^*\mathbf{\Phi}_1^* + a_2^*\mathbf{\Phi}_2^*)\,\vec{r}\,(a_1\mathbf{\Phi}_1 + a_2\mathbf{\Phi}_2)\,d^3r \\ &= \vec{r}_{12}a_1^*(t)\,a_2(t) + \text{complex conjugate} \end{aligned} \tag{1.17}$$

Analogous to the Lorentz model, an equation of motion for the expectation value of the electron displacement may now be derived using the time-dependent Schrödinger equations of 1.12. For linearly polarized light and a real valued $\vec{r}_{12}$, the equation of motion may be written as:

$$\left(\frac{d^2}{dt^2} + \omega_0^2\right)\langle\vec{r}\rangle = \frac{2e\omega_0}{\hbar}\vec{r}_{12}\left(\vec{r}_{21}\cdot\vec{E}\right)\left(|a_1(t)|^2 - |a_2(t)|^2\right) \tag{1.18}$$

Under the assumption that the excited state occupation probability is very small, the quantum mechanical equation of motion (1.18) reduces to the Lorentz-model equation of 1.3 and enables fundamental atomic parameters to be assigned to the oscillator strength. Comparing equations 1.18 and 1.3, the necessity for the parameter f becomes apparent. Equation 1.3 shows an electron responding to an electric field independent of orientation, while equation 1.18 uses the scalar product to determine the degree to which the dipole is aligned with the external field, thereby assigning a strength to the oscillators.

The preceding discussion regarding the quantum mechanical equivalent to the Lorentz model is extremely useful since it provides the incentive (via the position expectation value) to work with the products $c_1^*c_2$ and $c_1c_2^*$, rather than the isolated c's.

For this reason, the density matrix elements of a two-state system may be defined as:

$$\begin{aligned}\rho_{12} &= c_1 c_2^* \\ \rho_{21} &= c_2 c_1^* \\ \rho_{11} &= c_1 c_1^* = |c_1(t)|^2 \\ \rho_{22} &= c_2 c_2^* = |c_2(t)|^2 \end{aligned} \tag{1.19}$$

The first two equations of 1.19 represent the complex amplitudes of the expectation value $\langle \vec{r} \rangle$, while the last two equations are simply the occupation probabilities of the states. Writing the time-dependent Schrödinger equations of 1.16 in terms of the density matrix elements of equations 1.19, the following equations of motion are obtained:

$$\begin{aligned}\dot{\rho}_{12} &= i\Delta\rho_{12} + i\frac{\chi^*}{2}(\rho_{22} - \rho_{11}) \\ \dot{\rho}_{21} &= -i\Delta\rho_{21} - i\frac{\chi}{2}(\rho_{22} - \rho_{11}) \\ \dot{\rho}_{11} &= -\frac{i}{2}(\chi\rho_{12} - \chi^*\rho_{21}) \\ \dot{\rho}_{22} &= \frac{i}{2}(\chi\rho_{12} - \chi^*\rho_{21}) \end{aligned} \tag{1.20}$$

1.3.4 Elastic and inelastic collisions

The equations of 1.20 must now be modified to accommodate processes such as inelastic and elastic collisions (as was discussed in Section 1.2). Although proper statistical mathematics may be used to derive the extra terms due to collisions, these terms will simply be introduced along with a discussion of their meanings. It is however important to note that from this point onwards, the equations of motion for the ρ's represent an average atom.

As the name "inelastic collision" suggests, it is accompanied by energy loss. The energy loss translates into changes in the occupation probabilities ρ_{11} and ρ_{22}:

$$\begin{aligned}\dot{\rho}_{11} &= -\Gamma_1\rho_{11} + A_{21}\rho_{22} - \frac{i}{2}(\chi\rho_{12} - \chi^*\rho_{21}) \\ \dot{\rho}_{22} &= -(\Gamma_2 + A_{21})\rho_{22} + \frac{i}{2}(\chi\rho_{12} - \chi^*\rho_{21}) \end{aligned} \tag{1.21}$$

The terms $-\Gamma_1\rho_{11}$ and $-\Gamma_2\rho_{22}$ are a result of inelastic collisions leading to an exponential decay of the occupation probability from the lower and upper energy levels respectively, into other energy levels of the atom. Similarly, $\pm A_{21}\rho_{22}$ denotes spontaneous emission and signifies exponential decay from the upper energy level into the lower level, whilst emitting a photon. The third term in both equations are the contribution from the Schrödinger equations (as in 1.20).

In contrast to inelastic collisions, elastic collisions conserve the energy involved, thereby not influencing the occupation probabilities. Elastic collisions do however lead to a phase lag, as was previously discussed, and for this reason have an effect on the quantum mechanical electron displacement (ρ_{12} and ρ_{21}). Although elastic collisions do not influence ρ_{11} and ρ_{22}, inelastic collisions also affect ρ_{12} and ρ_{21}:

$$\begin{aligned} \dot{\rho}_{12} &= -(\beta - i\Delta)\,\rho_{12} + i\frac{\chi^*}{2}(\rho_{22} - \rho_{11}) \\ \dot{\rho}_{21} &= -(\beta + i\Delta)\,\rho_{21} - i\frac{\chi}{2}(\rho_{22} - \rho_{11}) \end{aligned} \tag{1.22}$$

In the equations of 1.22, β denotes the total relaxation rate, given by: $\beta = \frac{1}{\tau} + \frac{1}{2}(\Gamma_1 + \Gamma_2 + A_{21})$. The term $-\frac{1}{\tau}\rho_{21}$ gives the rate at which elastic collisions occur, whilst the inelastic terms included in β arise from the fact that the density matrix element ρ_{12} (for example) is related to elements ρ_{11} and ρ_{22} by:

$$|\rho_{12}| = \sqrt{\rho_{11}\rho_{22}} \tag{1.23}$$

Elastic collisions will often dominate and for the remainder of this document $\beta \approx \frac{1}{\tau}$ is approximated.

1.3.5 The population rate equations

In the case where the total relaxation rate (β) is dominated by the elastic collision rate $\frac{1}{\tau}$, it is found that the atom's response to the external field is no longer oscillatory. In fact, external forces only produce a quasi steady-state increase or decrease in the occupation probabilities. This increase or decrease corresponds to the terms stimulated emission and absorption respectively. Although the expressions for the absorption and stimulated emission coefficients as well as the spontaneous emission coefficient (first introduced by Einstein) shall not be derived here, the origins of the coefficients will be explained at the hand of the equations of motion for the density matrix elements.

The elastic collisions responsible for the fast decay in the atom's response to an external field is only located in the equations given by 1.22. This means that the elements ρ_{12} and ρ_{21} very quickly reach a quasi steady-state and their time-derivatives may be set to zero, yielding the following:

$$\begin{aligned} \rho_{12} &= \frac{i\chi^*/2}{\beta - i\Delta}(\rho_{22} - \rho_{11}) \\ \rho_{21} &= \frac{-i\chi/2}{\beta - i\Delta}(\rho_{22} - \rho_{11}) \end{aligned} \tag{1.24}$$

The process whereby the time-derivatives are set to zero is called the adiabatic approximation.

Substituting the expressions for ρ_{12} and ρ_{21} (equations 1.24) into the equations of 1.21, gives the population rate equations:

$$\begin{aligned}\dot{\rho}_{11} &= -\Gamma_1\rho_{11} + A_{21}\rho_{22} + \frac{|\chi|^2\beta/2}{\Delta^2+\beta^2}(\rho_{22}-\rho_{11}) \\ \dot{\rho}_{22} &= -(\Gamma_2 + A_{21})\rho_{22} - \frac{|\chi|^2\beta/2}{\Delta^2+\beta^2}(\rho_{22}-\rho_{11})\end{aligned} \tag{1.25}$$

The first two terms in both expressions of 1.25 have already been discussed in the previous section, while the last two terms indicate stimulated emission and absorption respectively. Since the last two terms are equivalent except for a change in sign, the coefficient $\frac{|\chi|^2\beta/2}{\Delta^2+\beta^2}$ is written more compactly as $R = \sigma\phi$, where $\sigma(\Delta)$ is either the emission or absorption cross section and $\phi = I/\hbar\omega$ is called the photon flux. Multiplying the occupation probabilities by N, the density of atoms, and defining the gain coefficient $g(\Delta) = \sigma(\Delta)(N_2 - N_1)$, the final form of the population rate equations becomes:

$$\begin{aligned}\dot{N}_1 &= -\Gamma_1 N_1 + A_{21}N_2 + g\phi \\ \dot{N}_2 &= -\Gamma_2 N_2 - A_{21}N_2 - g\phi + K\end{aligned} \tag{1.26}$$

The symbol K in the upper-state rate equation represents the pumping rate. The pumping mechanism is responsible for creating a population inversion $(N_2 - N_1)$ and will be discussed in Chapter 2.

1.4 The continuity equation

The purpose of this section is to obtain an equation describing the amplification of light. For this, use shall be made of Poynting's theorem in one dimension. The energy density within a light wave is defined as the intensity (modulus squared of the electric field's amplitude) divided by the velocity of the wave, $u(z) = I/c$.

The electromagnetic power transported by a plane wave across some plane of area A at position z, is given by $I(z)A$. Similarly, the power transported across a plane at position $z+\Delta z$ is given by $I(z+\Delta z)A$. According to the definition of the derivative, the change in the power with respect to the z-coordinate is:

$$\begin{aligned}\frac{\partial}{\partial z}(IA) &= [I(z+\Delta z) - I(z)]A/\Delta z \\ \frac{\partial}{\partial z}(IA)\Delta z &= [I(z+\Delta z) - I(z)]A\end{aligned} \tag{1.27}$$

The change in power should however be consistent with the rate at which electromagnetic energy leaves the volume $A\Delta z$:

$$-\frac{\partial}{\partial t}\left(uA\Delta z\right) = \frac{\partial}{\partial z}\left(IA\right)\Delta z \tag{1.28}$$

Rewriting equation 1.28, the equation of continuity results:

$$\frac{1}{c}\frac{\partial}{\partial t}I + \frac{\partial}{\partial z}I = 0 \tag{1.29}$$

Although the right-hand side of equation 1.29 corresponds to a vacuum, it may easily be replaced by rates responsible for the change in electromagnetic energy in a so-called gain medium (two-state system for example). When a monochromatic plane wave of frequency ω propagates in the z-direction through a medium with a resonance frequency at ω, the absorption of radiation will create a population inversion. The upper state population may be stimulated by an external radiation source to emit photons and the net result is amplification of the radiation as quantified by the gain coefficient, $g\left(\Delta\right)$. The equation of continuity thus becomes:

$$\frac{1}{v}\frac{\partial}{\partial t}I + \frac{\partial}{\partial z}I = g\left(\Delta\right)I \tag{1.30}$$

The parameter v replaces c and denotes the velocity of the electromagnetic wave in a medium ($v \leq c$).

Equation 1.30, together with the population rate equations of 1.26 forms the basis of the theory of light-matter interaction in the semi-classical approach and will be discussed to detail in the next chapter.

Chapter 2

Numerical models

The population rate equations and the differential equation describing the dynamics of the field intensity are coupled by the population densities N_1 and N_2. Many textbooks show how these coupled equations can be solved analytically under certain (often crude) approximations. The fact of the matter remains that these coupled equations can not be solved analytically without such approximations and therefore the use of a numerical approach is required. In this chapter a numerical model capable of predicting the gain that can be expected from a continuous wave (CW) amplifier as well as a pulse amplifier will be described. Since not all effects can realistically be accounted for, the model is based on a number of approximations and certain phenomena are made a priority.

2.1 Adjusting the population rate equations

2.1.1 Assumptions

The equations of 1.26 and 1.30 were derived for a hypothetical two-state system. In such a system the radiation absorbed from an external electromagnetic wave, corresponding to the resonance frequency of the medium, also leads to stimulated emission of radiation at the same frequency. In addition, the effect of spontaneous emission and other possible inelastic collisions contribute to the de-population of the upper state, making a positive population inversion ($N_2 - N_1$) impossible to obtain. The use of gain media consisting of three or more active states are therefore required to obtain laser action [18].

Figure 2.1 shows a typical four-state system. For a four-state system a pump (previously labeled K) with radiation at frequency ω_p is used to excite atoms from energy level $|1\rangle$ to level $|4\rangle$. The energy of the system is then lowered from $|4\rangle$ to $|3\rangle$ by what is assumed to be very fast non-radiative transitions. The mechanism of fast non-radiative transitions populates $|3\rangle$. In the presence of a probe with radiation at frequency ω_s, corresponding to the energy difference $\Delta E_{23} = \hbar\omega_s$ between $|2\rangle$ and $|3\rangle$, energy level $|3\rangle$ is partially depopulated by stimulated emission (ω_s) and spontaneous emission, leading to amplification of the probe wave.

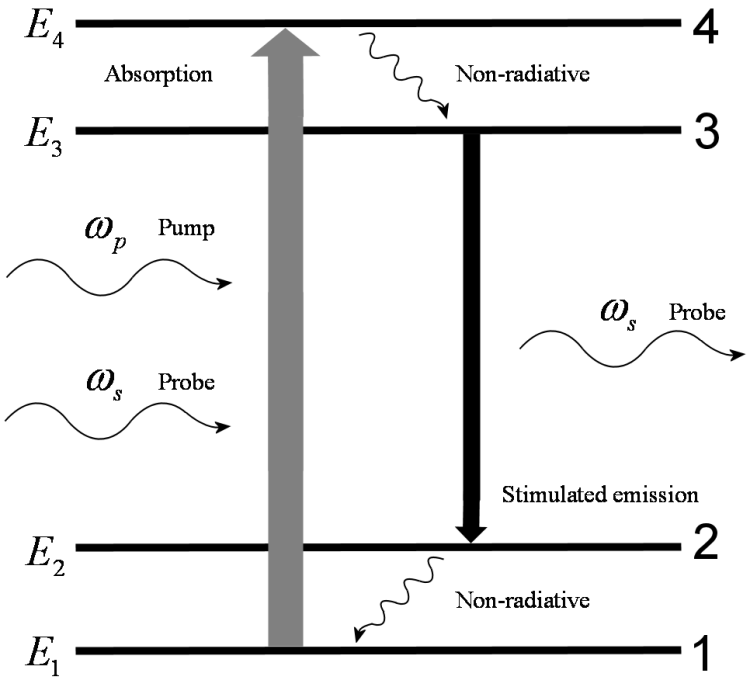

Figure 2.1: A four-state system showing the mechanisms responsible for laser action.

Although the process whereby amplification takes place results in the atom lowering its energy from $|3\rangle$ to $|2\rangle$, fast non-radiative transitions once again decreases the atom's energy to $|1\rangle$ [18, 19].

The efficiency of a laser scheme depends heavily on the rate at which the fast non-radiative transitions depopulate $|4\rangle$ and $|2\rangle$. If the de-population rates are sufficiently fast, the pump may be treated as though it excites atoms to $|3\rangle$ instead of $|4\rangle$, while the stimulated and spontaneous emission may be treated as though it de-excites atoms directly to $|1\rangle$. Since none of the atoms get trapped in $|4\rangle$ and $|2\rangle$, the rapid de-population effectively prevents the pump and probe waves of acting in reverse to repopulate $|1\rangle$ and $|3\rangle$ respectively. The four-state system of Figure 2.1 may therefore be viewed as a two-state system consisting of levels $|1\rangle$ and $|3\rangle$, whilst keeping in mind that the frequencies of the pump and the probe are different from each other (Figure 2.2). The approximation of a two-state system does not imply a loss of information, since the multi-level structure of the energy diagram is contained within the respective absorption and emission cross sections of a given transition. For simplicity the levels previously labeled as $|1\rangle$ and $|3\rangle$ are now denoted as levels as $|1\rangle$ and $|2\rangle$, respectively.

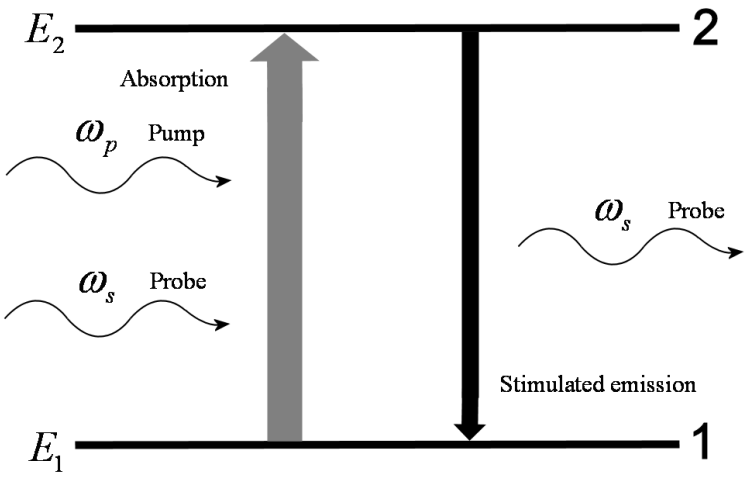

Figure 2.2: Simplified "four-state" system as a result of assuming fast non-radiative transitions.

With the simplifications as illustrated in Figure 2.2, the appropriate rate equations are very similar to that of equation 1.26. Inelastic collisions may be neglected as a result of its relative magnitude, with respect to the stimulated processes and spontaneous emission, yielding the rate equations given by:

$$\begin{aligned} \dot{N}_1 &= A_{21}N_2 + (\sigma_{21}^p\phi^p + \sigma_{21}^s\phi^s)\,N_2 - (\sigma_{12}^p\phi^p + \sigma_{12}^s\phi^s)\,N_1 \\ \dot{N}_2 &= -A_{21}N_2 - (\sigma_{21}^p\phi^p + \sigma_{21}^s\phi^s)\,N_2 + (\sigma_{12}^p\phi^p + \sigma_{12}^s\phi^s)\,N_1 \end{aligned} \tag{2.1}$$

A comparison between the sets of equations given by 1.25, 1.26 and 2.1 shows the way in which the gain coefficient now consists of contributions from four different cross sections (σ_{21}^p, σ_{21}^s, σ_{12}^p and σ_{12}^s). Furthermore, the equations of 2.1 is subject to two distinct photon flux contributions ($\phi^p$and ϕ^s). The cross section subscript 21 denotes stimulated emission from $|2\rangle$ to $|1\rangle$, while 12 denotes absorption from $|1\rangle$ to $|2\rangle$. A p-superscript for the cross sections and photon flux refers to radiation at the pump frequency (ω_p) and an s-superscript to that at the probe frequency (ω_s). Adding the two equations of 2.1, it is found that the total population density is time-independent and that the sum of the level population densities therefore remains constant.

$$N_1 + N_2 = N \tag{2.2}$$

The symbol N was previously defined as the density of atoms. From the relation between N_1 and N_2 (2.2), the two equations of 2.1 may conveniently be expressed only in terms of the upper-state population rate equation and the density of atoms:

$$\dot{N}_2 = -A_{21}N_2 - (\sigma_{21}^p\phi^p + \sigma_{21}^s\phi^s)\,N_2 + (\sigma_{12}^p\phi^p + \sigma_{12}^s\phi^s)\,(N - N_2) \tag{2.3}$$

For the purpose of simulating the gain dynamics of an amplifier in CW mode, a temporal steady-state is assumed. A temporal steady-state implies that the time derivative of equation 2.3 is taken as zero. Applying the relation between the photon flux and intensity and rewriting the frequency as $\nu = \omega/2\pi$, the solution to the steady state rate equation becomes:

$$N_2 = \frac{\left(\frac{\sigma_{12}^p I^p}{h\nu_p} + \frac{\sigma_{12}^s I^s}{h\nu_s}\right) N}{\left[\left(\frac{\sigma_{12}^p I^p}{h\nu_p} + \frac{\sigma_{12}^s I^s}{h\nu_s}\right) + \left(\frac{\sigma_{21}^p I^p}{h\nu_p} + \frac{\sigma_{21}^s I^s}{h\nu_s}\right) + \frac{1}{\tau}\right]} \tag{2.4}$$

The term $\frac{1}{\tau}$, with τ being the spontaneous emission lifetime, replaces A_{21}.

Since the system is subject to two radiation fields (pump and probe), the dynamics of the intensity of both the radiation fields must be described by its own differential equation in analogy with equation 1.30. Again, the gain coefficient as defined at the end of Chapter 1 is no longer applicable and is replaced by the appropriate cross section terms. Using the temporal steady-state, the differential equations for the radiation fields are given in terms of intensity by the following:

$$\begin{aligned} \frac{\partial I^p}{\partial z} &= \left[\sigma_{21}^p N_2 - \sigma_{12}^p (N - N_2)\right] I^p \\ \frac{\partial I^s}{\partial z} &= \left[\sigma_{21}^s N_2 - \sigma_{12}^s (N - N_2)\right] I^s \end{aligned} \tag{2.5}$$

The equations of 2.5, together with equation 2.4, are the most general form of the equations that shall be used to describe the CW mode amplification of light. Section 2.1.2 deals with the modification of these general equations to also include other aspects of amplifier theory.

2.1.2 Focusing effects

When dealing with SS amplifiers, diode pumping is often preferred due to its relative simplicity and high output power. As will be discussed in detail in Chapter 3, these diode modules are fibre coupled and have a multiple transverse mode output. A multi-mode output is characterized by a non-ideal beam quality factor ($M^2 > 1$), resulting in a number of complications with respect to optical design [19, 20]. The beam quality factor is essentially a measure of how tightly a laser beam can be focused under certain conditions and gives an idea of the extent to which the beam is diffraction limited [21]. To appreciate the implications of such a non-ideal beam, it is necessary to take a look at the physical properties of Gaussian beams.

A Gaussian beam propagating in the z-direction, is defined by an intensity profile given by [18]

$$I(x, y, z) = |A|^2 e^{-2\left(x^2+y^2\right)/w^2} \tag{2.6}$$

where A is the complex scalar wave amplitude, x and y the transverse position coordinates and w the spot size radius of the beam (lateral position from the z-axis where the intensity decrease by a factor of $\frac{1}{e^2}$).

The amplitude, A, may be expressed in terms of the complex radius of curvature, given by:

$$\frac{1}{q(z)} = \frac{1}{R(z)} + \frac{i\lambda}{\pi w^2(z)} \tag{2.7}$$

$R(z)$ is the radius of curvature of the wavefront. The parameter $q(z)$ has the additional property that $q(z) = q_0 + z$, where $q_0 = q(0) = \frac{i\lambda}{\pi w_0^2}$, since $R_0 = R(0) = \infty$ (plane). $w_0 = w(0)$ is defined as the beam waist, since it represents the minimum spot size radius along the beam propagation path (Figure 2.3). In the case of $M^2 \neq 1$, the two expressions for $q(z)$ may be equated and the real and imaginary parts respectively yield:

$$R(z) = z + \frac{z_0^2}{(M^2)^2 z} \tag{2.8}$$

$$w(z) = w_0\sqrt{1 + \frac{(M^2)^2 z^2}{z_0^2}} \tag{2.9}$$

The new parameter, $z_0 = \frac{\pi w_0^2}{\lambda}$, is defined as the Rayleigh range and is a measure of the length over which the beam may be assumed to be collimated about the waist region (Figure 2.3). With the factor $\left(M^2\right)^2$ included, the spot size radius will diverge at a rate linearly proportional to the beam quality factor (M^2) and will also be larger for a smaller beam waist.

When considering the derivative of the intensity with respect to the position coordinate along the optical axis (say z), as in equations 2.5, the following is found:

$$\begin{aligned} \frac{dI}{dz} &= \frac{d}{dz}\left(\frac{P}{A}\right) \\ &= \frac{1}{A}\frac{dP}{dz} + P\frac{d}{dz}\left(\frac{1}{A}\right) \\ &= \frac{1}{A}\frac{dP}{dz} + \frac{2I\pi w}{A}\frac{dw}{dz} \end{aligned} \tag{2.10}$$

The first term represents so-called power gain and gives the change in intensity as a result of a change in power, with $A = \pi w^2$ labeling the cross-sectional area of the beam. The second term is denoted the geometrical gain, since it gives the change in intensity resulting from a change in the spot size radius of the beam (focusing or de-focusing).

The differential equations describing the dynamics of the intensities of the pump and probe beams (equations 2.5) only take account of intensity changes due to changes in power. The fact that the intensity at a given z-position is dependent on the spot size radius of the beam at that position, motivates the inclusion for a term describing the beam propagation dynamics, especially in the event of a high M^2-beam (like that of a diode).

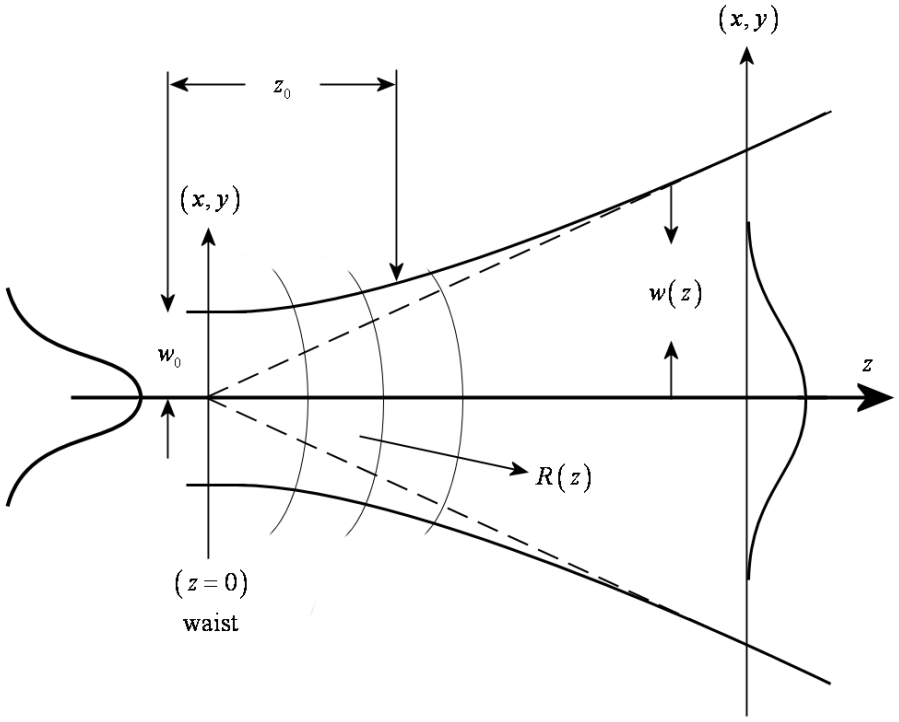

Figure 2.3: Definition of the relevant quantities of a Gaussian beam diverging away from its waist [18, 19].

The equations in 2.5 may then be rewritten as:

$$\frac{\partial I_p}{\partial z} = \left[\sigma_{21}^p N_2 - \sigma_{12}^p \left(N - N_2\right)\right] I_p - \frac{2 I_p M_p^4 \lambda_p^2 z}{\left(\pi w_{0p}^4 + M_p^4 \lambda_p^2 z^2\right)} \tag{2.11}$$

$$\frac{\partial I_s}{\partial z} = \left[\sigma_{21}^s N_2 - \sigma_{12}^s \left(N - N_2\right)\right] I_s - \frac{2 I_s M_s^4 \lambda_s^2 z}{\left(\pi w_{0s}^4 + M_s^4 \lambda_s^2 z^2\right)} \tag{2.12}$$

Once again a subscript p or s indicate the quantities related to the pump or signal beams respectively.

2.1.3 Amplified spontaneous emission

The final phenomenon that will be included in the rate equation approach, used in the numerical model to follow, is that of amplified spontaneous emission (ASE). As the name suggests, ASE is the mechanism whereby the spontaneous emission, resulting from the spontaneous de-excitation of the upper level atoms, is amplified by stimulating the de-excitation of more atoms. Not all spontaneous emission is amplified, as will be clear from the adjustments made to the model equations.

It is important to consider ASE since, especially at high gain, it has the potential to deplete the excited state population substantially, leading to severe gain saturation.

Amplification of spontaneous emission takes place over the full emission spectrum and in random directions, due to the nature of spontaneous emission [18]. It however follows that only ASE components parallel to the optical axis (forward and backward) are amplified to a significant degree. For simplicity the emission cross sections of the media are modeled according to a Lorentzian lineshape, centered about the peak emission wavelength.

$$\sigma_{21}^{ASE}(\lambda) = \sigma_{21}^{s}(\lambda_0) \frac{\frac{1}{2}\Gamma}{\pi(\lambda-\lambda_0)^2+\left(\frac{1}{2}\Gamma\right)^2} \tag{2.13}$$

In equation 2.13, λ_0 denotes the peak emission wavelength, while Γ is the full width at half maximum (FWHM) of the Lorentzian profile. For the purpose of the numerical calculation the wavelength band is divided into a number of discrete intervals, each corresponding to a certain stimulated emission cross section value.

Propagation equations, describing the intensity evolution for the forward and backward propagating ASE, can be derived from equation 1.30 as were done for the intensities of the pump and probe in equations 2.5.

$$\begin{aligned}\frac{\partial I_{ASE,f}(\lambda_i)}{\partial z} &= \sigma_{21}^{ASE}(\lambda_i) N_2 I_{ASE,f}(\lambda_i) + \\ &\frac{2N_2 h\nu_{ASE}(\lambda_i)}{\tau}\frac{A_1}{4\pi L^2}\frac{\nu_{ASE}^4(\lambda_i)\sigma_{21}^{ASE}(\lambda_i)}{\sum_{\lambda_i}\nu_{ASE}^4(\lambda_i)\sigma_{21}^{ASE}(\lambda_i)}\end{aligned} \tag{2.14}$$

$$\begin{aligned}\frac{\partial I_{ASE,b}(\lambda_i)}{\partial z} &= \sigma_{21}^{ASE}(\lambda_i) N_2 I_{ASE,b}(\lambda_i) + \\ &\frac{2N_2 h\nu_{ASE}(\lambda_i)}{\tau}\frac{A_2}{4\pi L^2}\frac{\nu_{ASE}^4(\lambda_i)\sigma_{21}^{ASE}(\lambda_i)}{\sum_{\lambda_i}\nu_{ASE}^4(\lambda_i)\sigma_{21}^{ASE}(\lambda_i)}\end{aligned} \tag{2.15}$$

Subscripts f and b are used to denote the forward and backward propagating ASE components, respectively, whilst the index i simply refers to the relevant wavelength interval for which the ASE components are solved. The first term on the right-hand side of equations 2.14 and 2.15 represents amplification of the ASE intensities at the various wavelength intervals, whilst the second term gives the contribution to the ASE intensities due to spontaneous emission [22]. The first factor in the second term, $N_2 h\nu_{ASE}(\lambda_i)/\tau$, has units of power per unit volume and therefore represents the energy per unit time, per unit volume, spontaneously emitted from the excited state in the form of photons. The fraction of the spontaneously emitted photons that will be amplified is given by the solid angle $A_{1,2}/4\pi L^2$.

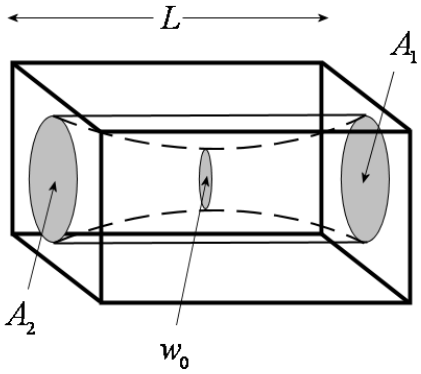

Figure 2.4: The solid angle within which spontaneous emission is amplified (solid line), compared to the evolution in the spot size of a Gaussian pump beam (dashed line).

The cross sectional areas A_1 and A_2 are those at the rear and front surface of the amplification medium respectively and correspond to the pump beam, since the pump is responsible for creating the population inversion leading to spontaneous emission (Figure 2.4) [18, 19]. The solid angle used in equations 2.14 and 2.15 is a rather crude approximation, but is sufficient as a first approach despite the fact that more sophisticated methods of modeling the ASE fractions are available [23, 24]. The final factor in the second term of equations 2.14 and 2.15 is obtained from the Fuchtbauer-Ladenburg equation [25, 22, 26] and simply gives the contribution of spontaneous emission from a given wavelength interval.

The addition of the ASE propagation equations brings about a change to the N_2-rate equation, due to the fact that ASE depletes the excited state atoms. The final form of the N_2-rate equation is given by the following:

$$\begin{aligned} N_2 \;=\; & N\left(\frac{\sigma_{12}^{p}I^{p}}{h\nu_p}+\frac{\sigma_{12}^{s}I^{s}}{h\nu_s}\right)\Big/\left[\frac{\sigma_{12}^{p}I^{p}}{h\nu_p}+\frac{\sigma_{12}^{s}I^{s}}{h\nu_s}+\right. \\ & \frac{\sigma_{21}^{p}I^{p}}{h\nu_p}+\frac{\sigma_{21}^{s}I^{s}}{h\nu_s}+\sum_{\lambda_i}\frac{\sigma_{21}^{ASE}\left(\lambda_i\right)I_{ASE,f}\left(\lambda_i\right)}{h\nu_{ASE}\left(\lambda_i\right)}+ \\ & \left.\sum_{\lambda_i}\frac{\sigma_{21}^{ASE}\left(\lambda_i\right)I_{ASE,b}\left(\lambda_i\right)}{h\nu_{ASE}\left(\lambda_i\right)}+\frac{1}{\tau}\right] \end{aligned} \tag{2.16}$$

2.2 Continuous wave model

The equations describing the propagation of the intensities for the pump, probe, forward ASE and backward ASE (equations 2.11, 2.12, 2.14, 2.15), together with the rate equation for the upper state population density (equation 2.16) forms the heart of the CW numerical model. In Section 2.2, the basic algorithm upon which the simulation is based as well as some of the typical results obtained from the model, will be discussed. The model is also reviewed afterwards resulting in some improvements.

2.2.1 Simulation algorithm

The model is based on a fairly simple iterative procedure and may be described at the hand of the following step-wise algorithm (Figure 2.5):

1. The crystal is divided lengthwise into a fixed number of increments along the optical axis.
2. At an initial time, the upper state population density is assumed to be zero throughout the length of the amplifying medium (in every segment).
3. The differential equations for the intensities of the pump and probe beams (equations 2.11 and 2.12) are solved in every segment, starting from the front surface of the amplifying medium, using a fourth-order Runga-Kutta method.
4. A new value for the upper state population density $N_2 = N_2(I_p, I_s)$ is calculated at every position along the optical axis (equation 2.4).
5. Since $N_2 \neq 0$ anymore, the differential equations for the pump, probe and ASE (forward and backward) are now re-solved for every segment (equations 2.11, 2.12, 2.14 and 2.15). Depending on the spectral resolution for which the ASE is solved, this yields a very large number of differential equations.
6. The upper state population density $N_2 = N_2(I_p, I_s, I_{ASE,f}, I_{ASE,b})$ is now re-calculated along the optical axis (equation 2.16).
7. Steps 5 to 6 are repeated consecutively until a so-called numerical steady-state is reached. The term numerical steady state simply means that the simulation is continued until the output intensity from the amplifier (rear surface) remains constant (within a relative error value) over iterations.

2.2.2 Typical output

In the model discussed until now, the pump beam has been assumed to have an uniform transverse intensity distribution (top hat). The assumption of a top hat intensity distribution is reasonable due to the pump beam's high M^2-value, as will be elaborated upon in Chapter 3. Although not explicitly assumed, the probe beam was also modeled with a top hat transverse intensity distribution due to the absence of any transverse coordinates in our model. Often, the probe beam to be amplified is a single mode TEM_{00} Gaussian beam (as may be associated with a fibre laser source), in which case this inadvertent assumption of a top hat probe beam is unjustified.

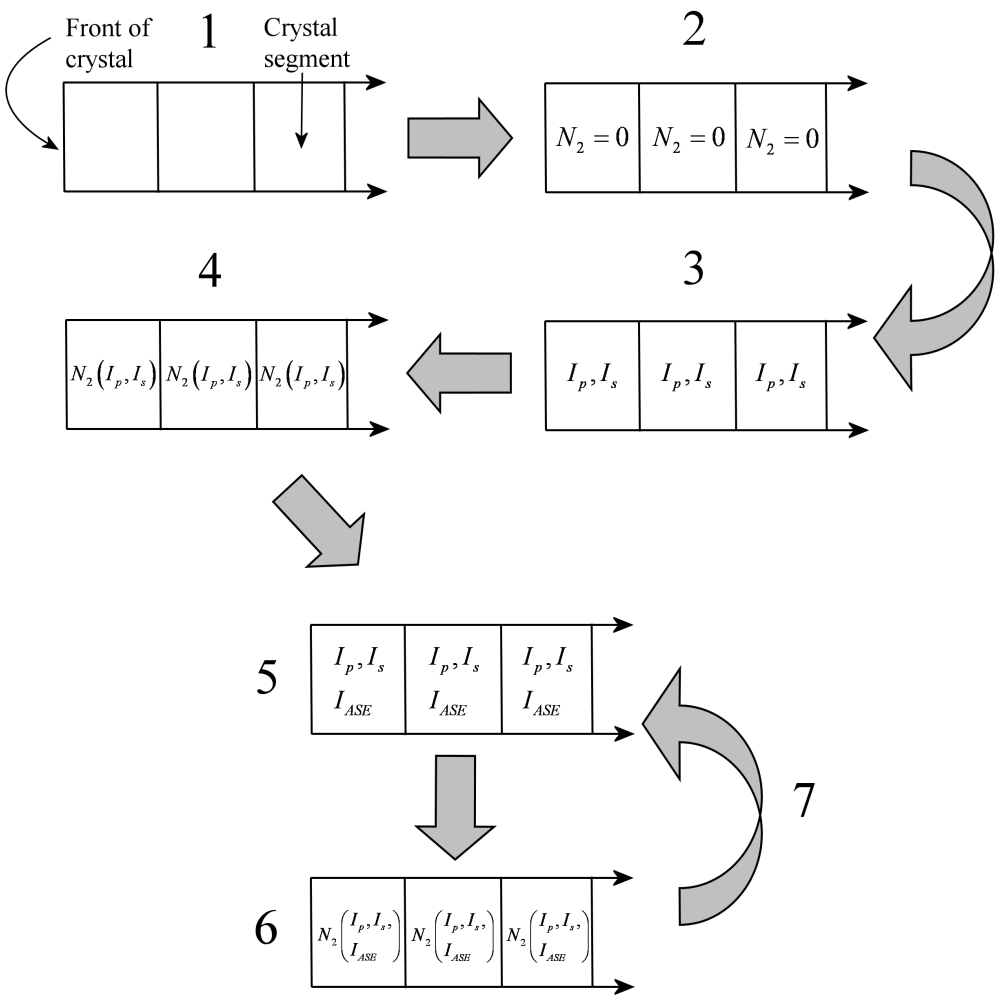

Figure 2.5: A diagrammatic graph showing the simulation algorithm.

As a result of the model's inability to account for non-uniform transverse intensity distributions, the pump and probe beams with their respective waist radii, M^2-values and wavelengths may be illustrated as in the left-hand side of Figure 2.6. The y-axis represents the intensity, while the x-axis indicates the radial coordinates (coordinates transverse to the propagation direction of the beams). The probe beam has a waist radius (w_{0s}^{real}) and M^2 small compared to that of the pump beam. However, as a further consequence of the absence of transverse coordinates, the model does not take account of the partial spatial overlap between the pump and probe beams. Therefore, the pump and probe beams are modeled as though they have identical waist radii, M^2-values and wavelengths. In an attempt to compensate for this discrepancy in the model, the waist and M^2-value of the probe beam are matched to that of the pump beam, $w_{0p}^{real} = w_{0s}^{new}$ (neglecting propagation effects due to wavelength differences). Changing the waist radius of the probe beam translates into a change in the cross-sectional area of the probe beam (A_{0s}).

Since the intensity of the probe beam is calculated according to the relation $I_{0s} = P_{0s}/A_{0s}$, the input probe power (P_{0s}) must be adjusted correspondingly to ensure that the initial probe intensity is maintained. The procedure to compensate for the discrepancy due to a lack of transverse coordinates is illustrated in the right-hand side of Figure 2.6. The appropriate factor to adjust the input probe power by is simply given by the ratio of the real pump waist radius to the real probe waist radius ($w_{0p}^{real}/w_{0s}^{real}$).

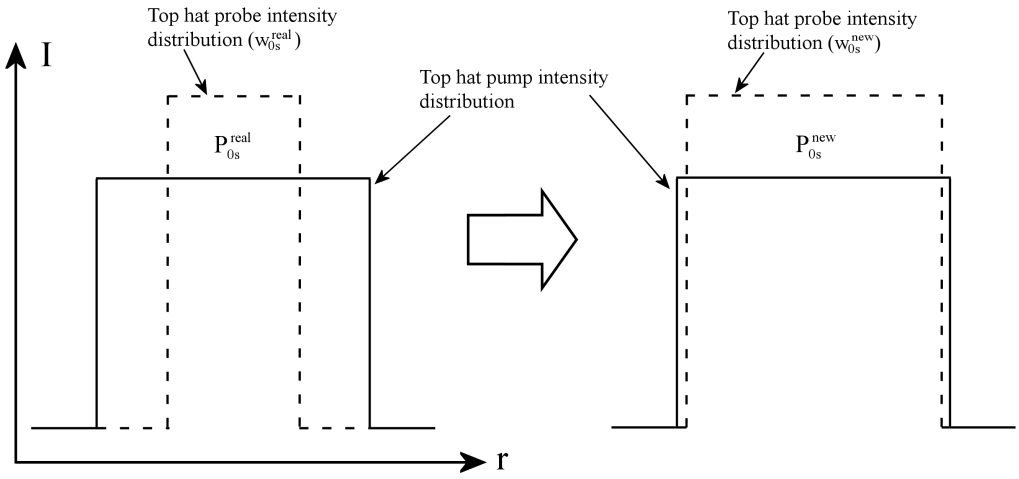

Figure 2.6: Illustration of the consequences of not having transverse coordinates in the CW model. The pump and probe beams are modeled with a top hat transverse intensity distribution (left-hand side). The probe waist radius and the input probe power have to be adjusted to compensate for the model's inability to model partial spatial overlap between the beams (right-hand side).

Figures 2.7 to 2.12 illustrate the results from the CW simulation for typical input parameters (Table 2.1). The Nd:YVO_4 crystal of length 6 mm is pumped by 30 W of pump power and amplifies a probe beam of initial power 1 μW. The pump and probe beams have top hat transverse intensity distributions and are focused in the center of the crystal. The probe beam has a "real" waist radius of 66 μm, which means that the initial power of the probe beam , for simulation purposes, is 2.62 μW. Nd:YVO_4 as amplifying medium will be discussed in Chapter 3 and for the current discussion it is sufficient to say that the pump and probe beams are π-polarized.

Figure 2.7 shows a graph of the probe intensity at the rear surface of the crystal after each iteration. The intensity oscillates about the steady state value for the first few iterations and reaches what was referred to as the numerical steady-state after about 16 iterations. The numerical steady-state indicates that the temporal dynamics has been eliminated from the system and that the quantities of interest may now be analyzed. The figures shown in 2.8 and 2.9 gives the value for the pump power and upper state population density as a function of position along the optical axis, respectively.

Symbol	Parameter	Value	Unit
L	Length of crystal	6	mm
N	Concentration of active atoms	7×10^{19}	cm^{-3}
τ	Spontaneous emission lifetime	98	μs
λ_p	Pump wavelength	801	nm
λ_s	Probe wavelength	1064	nm
$\sigma_{12}^{p,\pi}$	Pump absorption cross section	8×10^{-20}	cm^2
$\sigma_{12}^{s,\pi}$	Probe absorption cross section	0	cm^2
$\sigma_{21}^{p,\pi}$	Pump emission cross section	0	cm^2
$\sigma_{21}^{s,\pi}$	Probe emission cross section	123×10^{-20}	cm^2
M_p^2	Pump beam quality factor	100	-
$\left(M_s^2\right)^{new}$	Probe beam quality factor	100	-
w_{0p}^{real}	Pump waist radius	175	μm
w_{0s}^{new}	Probe waist radius	175	μm
P_{0p}^{π}	Initial pump power	30	W
P_{0s}^{π}	Initial probe power	$1 \times \frac{w_{0p}^{\mathrm{real}}}{w_{0s}^{\mathrm{real}}}$	μW
h	Planck's constant	6.63×10^{-34}	J s
c	Speed of light in vacuum	3×10^{8}	$\mathrm{m\,s}^{-1}$
n	Nd:YVO_4 refractive index	2	-
	ASE wavelength range	$1060 \rightarrow 1070$	nm
	Number of wavelength intervals	100	

Table 2.1: Parameters used in the CW simulation. A Nd:YVO_4 crystal and π-polarized beams are used for the purpose of illustrating typical results.

The pump power decreases drastically with propagation through the crystal due to absorption, as can be expected, and drops to half its initial power in less than a third of the crystal's length. The peculiar shape of the curve in Figure 2.9 is a result of the pump beam being focused in the centre of the crystal. The pump spot radius on the front surface of the crystal is 280 μm and is large compared to the waist radius of 175 μm. The fact that the upper state population density reaches its maximum value after a propagation distance of 2 mm is due to the increase in intensities as a result of the decrease in the pump beam's cross sectional area (spot radius). After the upper state population density has reached its maximum it decreases rapidly due to stimulated emission at the probe's wavelength (Figure 2.11) as well as spontaneous emission and specifically ASE across the emission spectrum of the crystal (Figure 2.10).

The forward propagating ASE power increases gradually towards the rear of the crystal, whilst the backward propagating ASE power is found to increase sharply at the front of the crystal where the population inversion is relatively large. Although the exact reason for the shape of the total ASE power curves is uncertain, the asymmetry of the curves in Figure 2.10 is sensible when considering the way in which the pump power is absorbed.

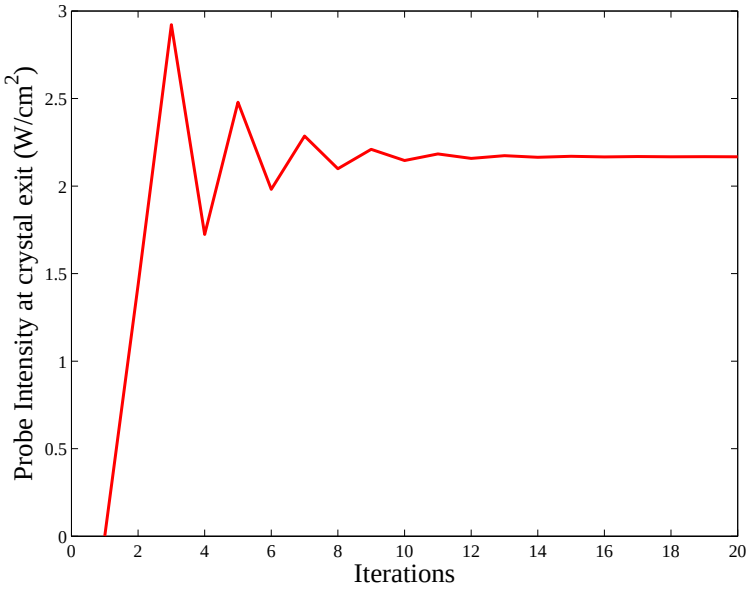

Figure 2.7: Probe intensity at the rear of the crystal converges to a numerical steady state.

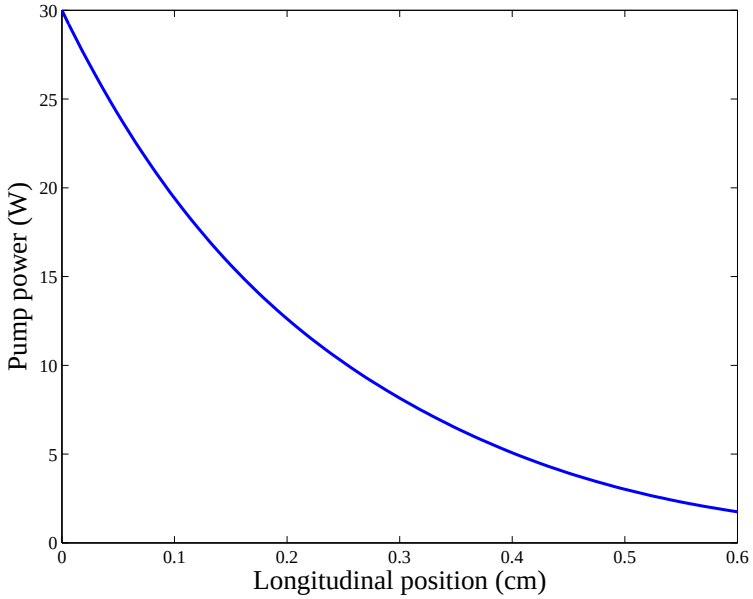

Figure 2.8: Decrease in pump power due to absorption over the length of the crystal. The pump beam is focused in the center of the crystal.

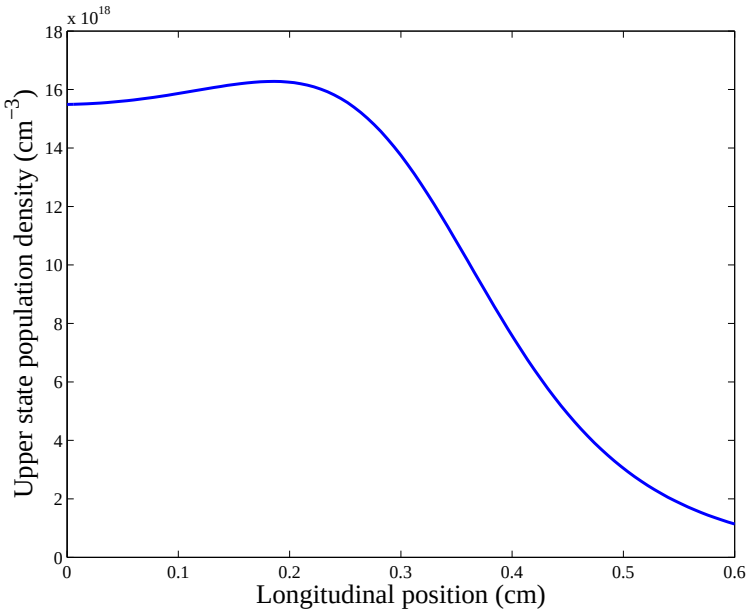

Figure 2.9: Upper state population density as a function of distance along the optical axis. The characteristic shape is determined by the intensities of the pump, probe and ASE at the corresponding coordinate.

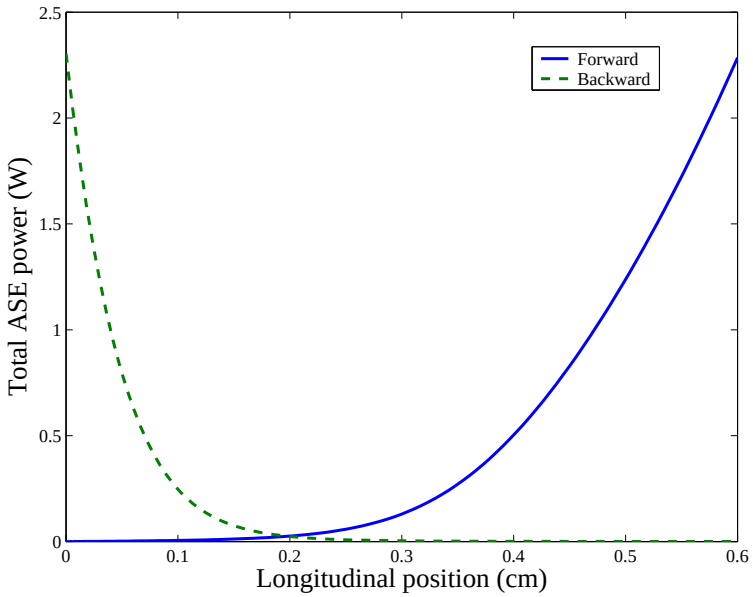

Figure 2.10: The contribution over all wavelengths to the forward propagating ASE (solid line) and backward propagating ASE (dashed line) with respect to position along the optical axis.

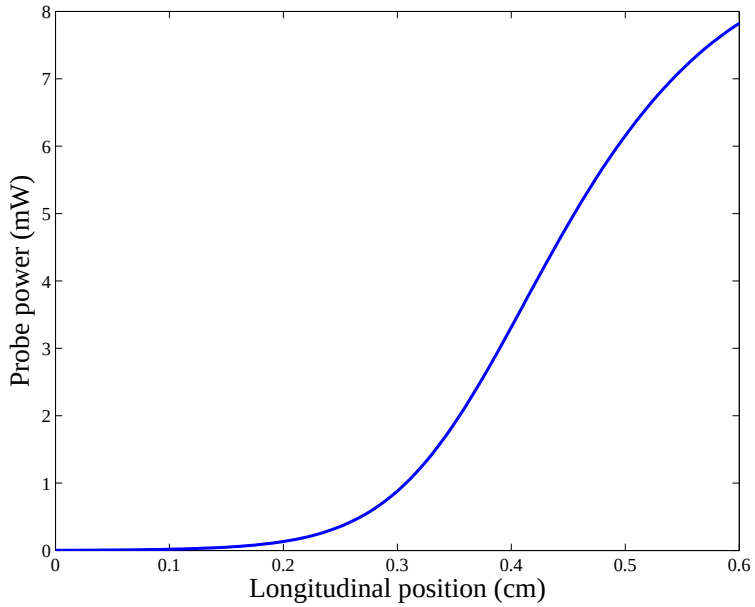

Figure 2.11: Increase in probe power due to amplification over the length of the crystal. The probe beam is focused in the center of the crystal.

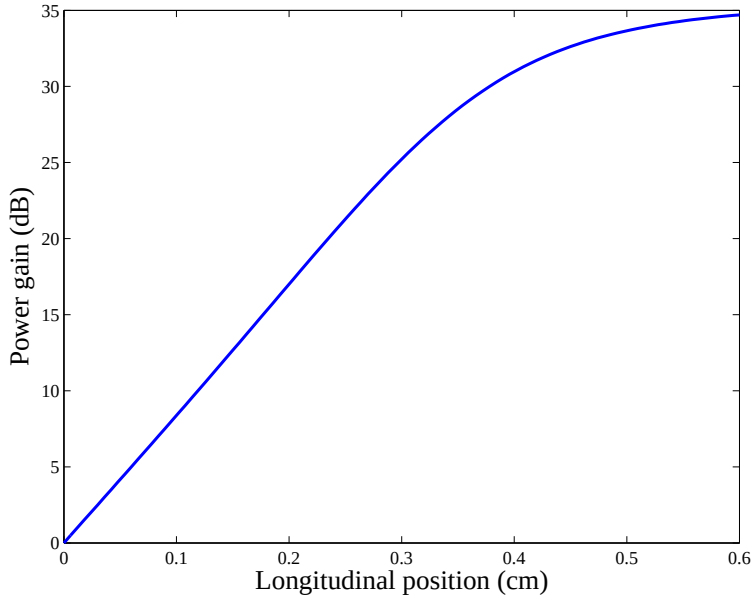

Figure 2.12: Gain experienced by the input probe power as a function of distance along the optical axis. The input probe power of 2.62 μW is amplified to an output power of 7.8 mW over the length of the crystal.

The magnitude of the probe power increases at an exponential rate, but starts to deplete the upper state population density after a propagation distance of 4.5 mm and the gain saturates correspondingly (Figure 2.12).

Here and throughout this thesis, the gain is expressed in units of dB and is calculated according to the simple relation:

$$G\ (\text{dB}) = 10\log_{10}\left(\frac{P_{out}}{P_{in}}\right) \tag{2.17}$$

P_{in} is the input probe power, while P_{out} represents the output probe power from this input power after being amplified over the distance indicated on the x-axis. For the case in Figure 2.12, the input power experiences a power gain of almost 35 dB after amplification over the full length of the crystal.

2.2.3 Addition of transverse coordinates

The results from Section 2.2.2 were obtained by adjusting the probe waist radius and input power by a factor of $w_{0p}^{real}/w_{0s}^{real}$. This waist radius factor does not completely resolve the discrepancies in the CW numerical model and the model is therefore ultimately flawed. In order to simulate the behaviour inside the amplification medium with greater accuracy and to remedy the fact that the current numerical model is unable to illustrate the effect of transverse gain saturation, a new approach is required.

In the case of a Gaussian probe beam, transverse coordinates may be built into the model using an intuitive approach, whereby discrete intensities are distributed along a Gaussian lineshape. When the front surface of the amplifying medium is illuminated by a Gaussian probe beam, the input power (P_{0s}) is represented by a number of "small" top hat beams of varying intensity (Figure 2.13).

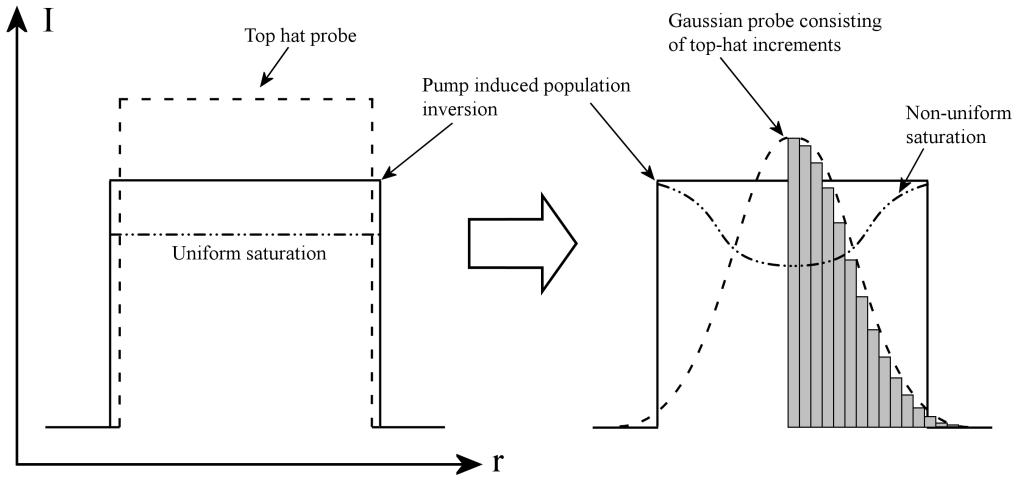

Figure 2.13: Procedure for the inclusion of transverse coordinates. The normal CW model can only simulate uniform transverse intensity distributions and therefore is unable to account for non-uniform transverse gain saturation (left-hand side). The improved CW model includes transverse coordinates by arranging top hat beams according to any non-uniform distribution.

The top hat beams effectively divide the cross-sectional area of the beam into a number of radial zones [27]. Assuming a high degree of symmetry in the probe beam, throughout the medium, the analysis may be restricted to one angular zone [28, 29]. The intensity in each radial zone constituting the Gaussian may be calculated using the expression

$$I(r) = I_0 \left(\frac{w_{0s}}{w_s}\right)^2 e^{-2r^2/w_s^2} \tag{2.18}$$

where, r is the radial coordinate, I_0 the peak intensity (associated with the innermost radial zone) and w_{0s} the beam waist radius. w_s denotes the spot size radius on the front surface of the medium. Since intensity is simply power per unit area ($I = P/A$), the peak intensity, I_0, may be calculated as follows:

$$I_0 = P_{0s} / \int_0^{2\pi} \int_0^{\infty} \left(\frac{w_{0s}}{w_s}\right)^2 e^{-2r^2/w_s^2} r \, dr \, d\theta \tag{2.19}$$

P_{0s} again denotes the input probe power, while θ is the angular coordinate. This means that the peak intensity, used to obtain the intensity within the respective radial zones, is calculated from the input probe power which is specified as one of the input parameters for the CW model.

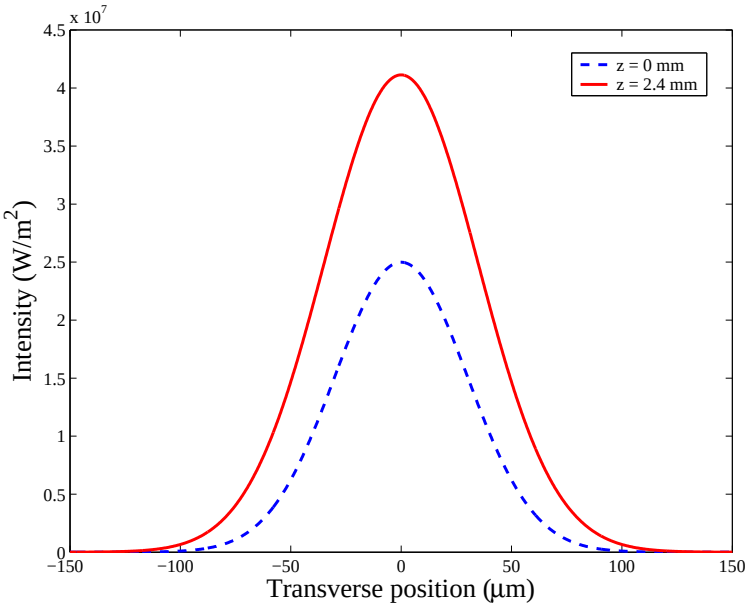

Figure 2.14: Comparison between the Gaussian intensity distribution at two different longitudinal positions within the crystal.

Each of the constituent top hats on the right-hand side of Figure 2.13 are propagated through the pumped amplifying medium making use of the simulation algorithm of Section 2.2.

After a certain propagation length, z, the individually propagated intensities may again be used to reconstruct the Gaussian intensity profile. The Gaussian intensity profile is reconstructed by fitting a Gaussian function to the radially distributed intensities. Once again, the power at z may be retrieved via integration. In contrast to the previous CW model, the probe spot size radius is now not only governed by diffraction (Gaussian beam optics), but is influenced by the amplification of the beam's intensity. As will be elaborated upon in the discussion of the model's output, the amplification of the radially distributed intensities are non-uniform.

Figure 2.14 shows the input intensity distribution (dashed line) and the intensity distribution obtained after amplification over a propagation distance of 2.4 mm. The parts of the input beam at different radial coordinates do not experience an equal amount of amplification. For comparative purposes, the discrete intensity at a certain transverse position on the solid line may be divided by the intensity on the dashed, corresponding to the same transverse position. Calculating the relative amplification at every transverse position results in Figure 2.15. The fact that the intensities on the wings of the Gaussian profile, percentage wise, experiences more gain than the central intensities, leads to a broadening in the profile as reflected in the spot size radius. This is called gain distortion [30]. The broadening effect is shown in Figure 2.16 and is found to be much more severe at the front end of the crystal while it becomes completely negligible at the back end of the crystal. The reason for the so-called gain distortion being so exaggerated in the example of Figures 2.14, 2.15 and 2.16 is the presence of a relatively large input probe power in a low-doped crystal, leading to the restriction of the amplification process to the front end of the medium.

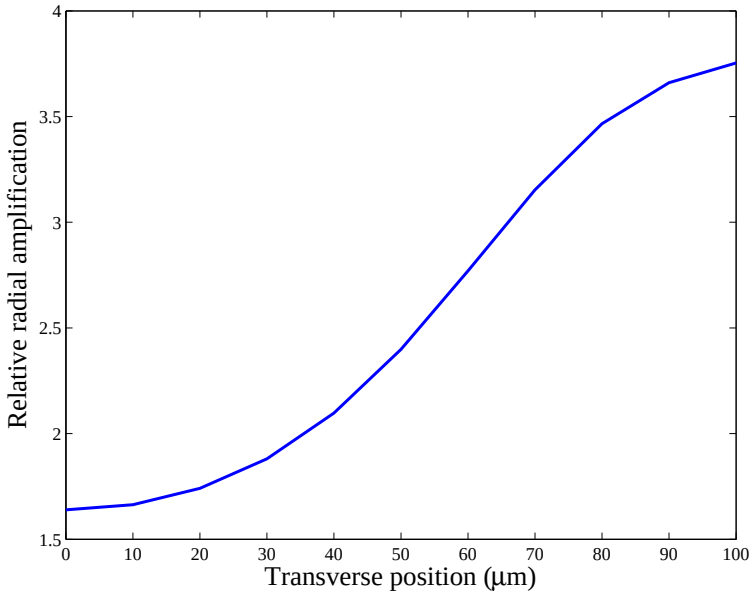

Figure 2.15: Relative radial amplification at two different longitudinal positions within the crystal as a result of non-uniform transverse amplification.

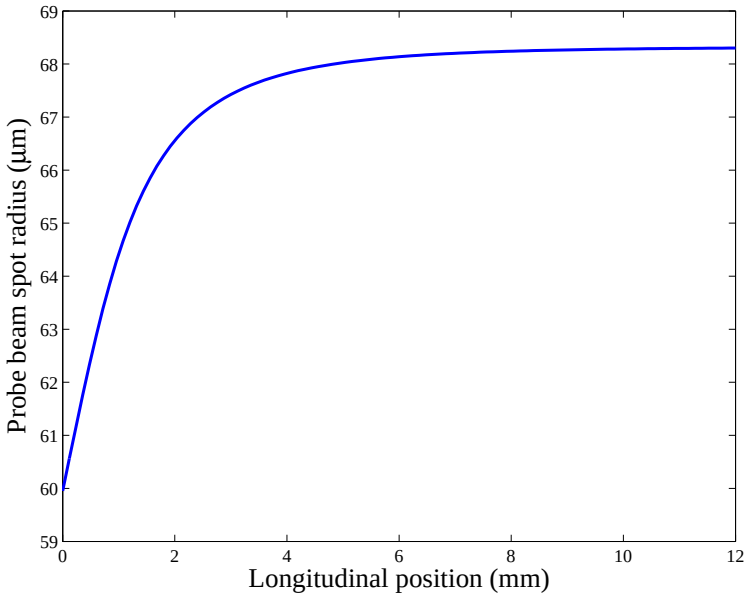

Figure 2.16: The diverging effect of non-uniform transverse amplification on a probe beam (gain distortion).

Since the probe source for an amplifier is usually associated with a high quality beam ($M_s^2 \simeq 1$) and a long Rayleigh range, the effects of diffraction (Gaussian beam optics) have a negligible influence on the spot size of the beam over the short length of a crystal. Therefore, the spot size of the probe beam is modeled to include gain distortion only.

Solving the intensities for the pump, probe and ASE, as well as the upper state population density, in every radial zone at every position along the optical axis, enables the three dimensional visualization of the dynamics inside the amplifying medium. The three-dimensional graphs can be interpreted as a plane, obtained from taking a slice through the area of the crystal overlapping with the probe beam (two-dimensional), with the colour at every position representing the third dimension.

The output from the CW simulation with transverse coordinates is shown below. The results were obtained using a crystal of length 1.2 cm, subject to an initial pump power of 20 W and an initial probe power of 140 mW. Both the pump and probe beams were focused on the front surface of the crystal. The probe beam with $M_s^2 = 1.14$ was modeled according to a Gaussian intensity distribution, while the pump beam with $M_p^2 = 314$ was modeled as a top hat. The crystal parameters and other important information is given in Table 2.2.

Symbol	Parameter	Value	Unit
L	Length of crystal	12	mm
N	Concentration of active atoms	3.3×10^{19}	cm^{-3}
τ	Spontaneous emission lifetime	98	μs
λ_p	Pump wavelength	803.84	nm
λ_s	Probe wavelength	1064	nm
$\sigma_{12}^{p,\pi}$	Pump absorption cross section	6.5×10^{-20}	cm^2
$\sigma_{12}^{s,\pi}$	Probe absorption cross section	0	cm^2
$\sigma_{21}^{p,\pi}$	Pump emission cross section	0	cm^2
$\sigma_{21}^{s,\pi}$	Probe emission cross section	123×10^{-20}	cm^2
M_p^2	Pump beam quality factor	314	-
M_s^2	Probe beam quality factor	1.14	-
w_{0p}	Pump waist radius	200	μm
w_{0s}	Probe waist radius	60	μm
P_{0p}^{π}	Initial pump power	20	W
P_{0s}^{π}	Initial probe power	0.14	W
n	Nd:YVO_4 refractive index	2	-
	ASE wavelength range	$1060 \rightarrow 1070$	nm
	Number of wavelength intervals	100	

Table 2.2: Parameters used in the CW simulation incorporating transverse coordinates. A Nd:YVO_4 crystal and π-polarized beams are used for the purpose of illustrating typical results.

Figure 2.17 shows how the pump beam starts off with an uniform intensity distribution. As in Figure 2.8, the pump intensity (or power) decreases rapidly with propagation distance, with a slight non-uniformity in the transverse intensity profile emerging after only 1 mm of propagation. The source of the non-uniformity in the intensity distribution can be explained at the hand of Figure 2.18, showing the upper state population density as a function of both the longitudinal and transverse position within the crystal. From Figure 2.18 the effect of the Gaussian intensity distribution of the probe is evident. The upper state population density in the center of the crystal is almost immediately depleted due to the probe intensities being a maximum in the center. In contrast to this, the smaller intensities, found at increasingly larger distances from the center of the crystal, takes a larger propagation distance to deplete the population density in their respective vicinities and therefore also experience more gain (refer to Figure 2.15(a)). Because of the population density being the lowest in the center, the pump beam is absorbed at a faster rate in the center, as opposed to the edges of the crystal, leading to the observed non-uniformity.

The effect of the highly non-uniform upper state population density is also very prominent in the figures showing the forward and backward propagating ASE as a function of position (Figures 2.19 and 2.20). Very little amplification of spontaneous emission takes place in the central part of the crystal, while the ASE at the edges of the medium contribute quite substantially to the depletion of the available population density. The backward propagating ASE shows a very sharp increase at the edges of the front surface of the crystal, resulting from the pump beam's waist being positioned at this surface.

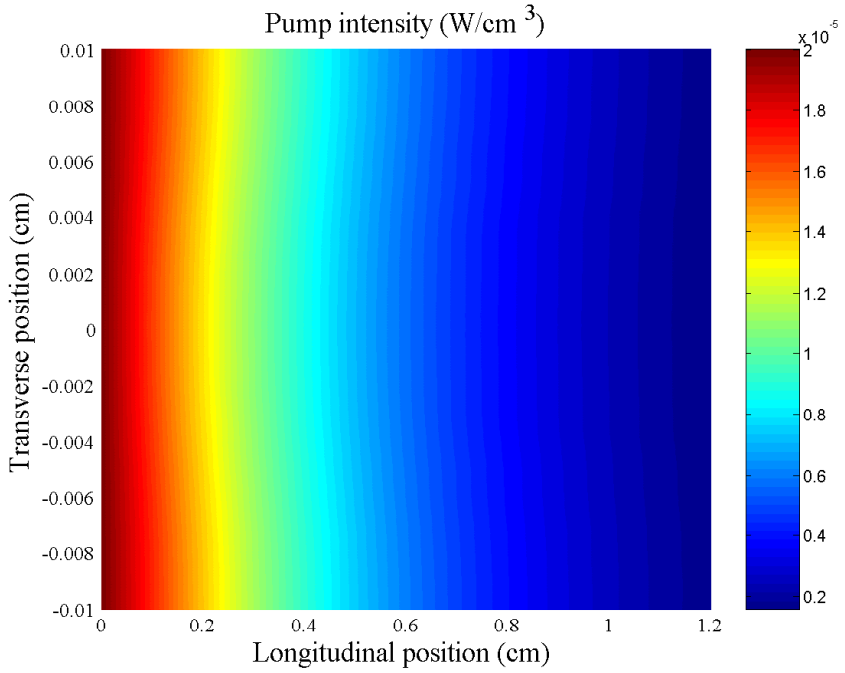

Figure 2.17: Top hat pump intensity as a function of longitudinal and transverse coordinates. The pump beam is focused on the front surface of the crystal.

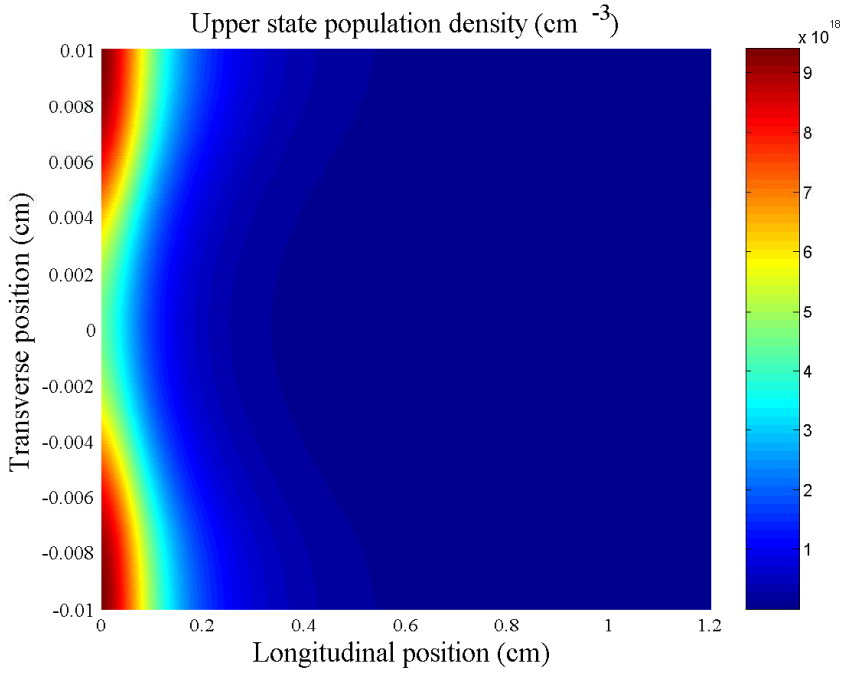

Figure 2.18: Upper state population density at all positions within the crystal overlapping with the Gaussian intensity distributed probe beam.

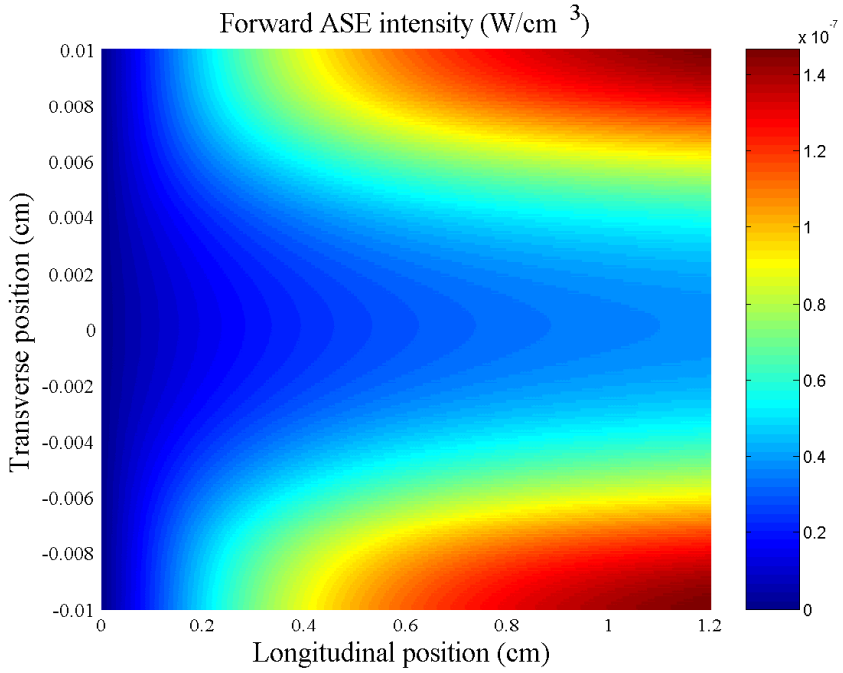

Figure 2.19: Contribution over all wavelengths to the forward propagating ASE as a function of position within the crystal.

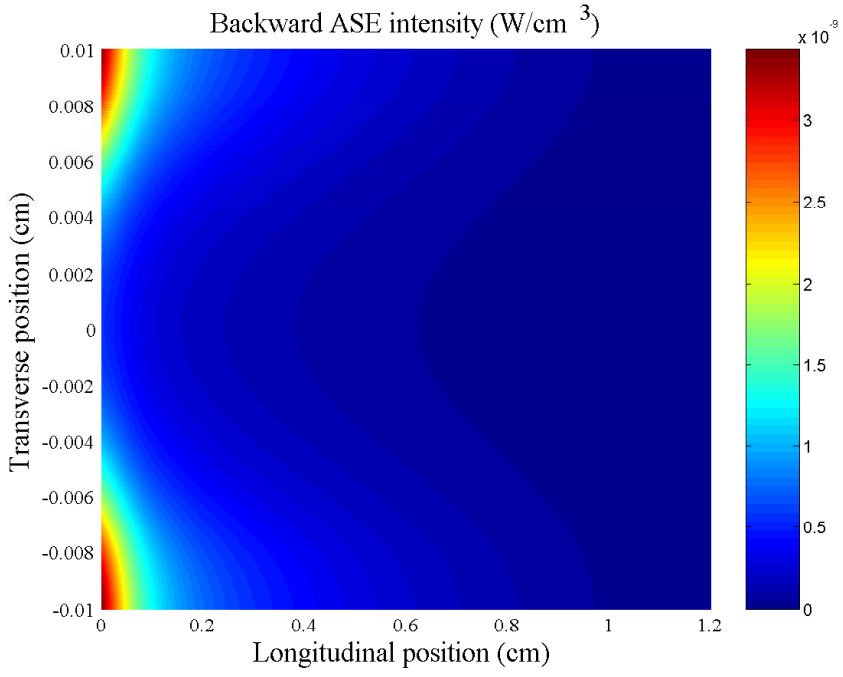

Figure 2.20: Contribution over all wavelengths to the backward propagating ASE as a function of position within the crystal.

2.3 Time-dependent model

The CW model of Section 2.2.3 is capable of characterizing a SS amplifier, taking into consideration the specific material properties and doping concentration of the medium as well as the defining properties of the pump and probe radiation fields. In addition to the CW model, a time-dependent model is presented in the interest of the ultimate development of a SS amplifier for the purpose of probe pulse amplification (initially under CW pumping conditions). One of the biggest advantages of the model developed thus far, is its relative simplicity. This section will describe the procedures followed to adapt the CW model into a model that takes account of temporal dynamics, while preserving its simplicity.

2.3.1 Adjusting the simulation algorithm

In Section 2.1.1, the temporal steady state was obtained from equation 2.3 by setting the time derivative of the upper state population density equal to zero, resulting in equation 2.4. The presence of temporal dynamics implies that the derivative of the upper state population density with respect to time is non-zero and equation 2.3 must therefore be solved (taking into account the influence of ASE). Since $N_2 = N_2\left(I_p, I_s, I_{ASE,f}, I_{ASE,b}\right)$ and $I_p = I_p\left(N_2\right)$, $I_s = I_s\left(N_2\right)$, $I_{ASE,f} = I_{ASE,f}\left(N_2, \lambda\right)$, $I_{ASE,b} = I_{ASE,b}\left(N_2, \lambda\right)$ the time-dependent model requires the simultaneous solution to, depending on the spectral resolution for which the ASE is solved, a very large number of coupled differential equations. The coupled differential equations, as stated previously, do not have an analytical solution and a numerical method is therefore essential. The preferred numerical procedure for the purpose of solving the coupled differential equations is the finite-difference method, whereby the upper state population density rate equation is discretized as follows:

$$\begin{aligned}\frac{dN_2}{dt} &= \frac{N_2\left(t+\Delta t\right) - N_2\left(t\right)}{\Delta t} \\ &= -A_{21}N_2 - \Bigg[\left(\sigma_{21}^p\phi^p + \sigma_{21}^s\phi^s\right) + \sum_{\lambda_i}\sigma_{21}^{ASE}\left(\lambda_i\right)I_{ASE,f}\left(\lambda_i\right) + \\ &\quad \sum_{\lambda_i}\sigma_{21}^{ASE}\left(\lambda_i\right)I_{ASE,b}\left(\lambda_i\right)\Bigg]N_2 + \left(\sigma_{12}^p\phi^p + \sigma_{12}^s\phi^s\right)\left(N - N_2\right) \qquad (2.20)\end{aligned}$$

$$\begin{aligned}N_2\left(t+\Delta t\right) &= N_2\left(t\right) + \{-A_{21}N_2 - [\left(\sigma_{21}^p\phi^p + \sigma_{21}^s\phi^s\right) + \\ &\quad \sum_{\lambda_i}\sigma_{21}^{ASE}\left(\lambda_i\right)I_{ASE,f}\left(\lambda_i\right) + \sum_{\lambda_i}\sigma_{21}^{ASE}\left(\lambda_i\right)I_{ASE,b}\left(\lambda_i\right)\Bigg]N_2 + \\ &\quad \left(\sigma_{12}^p\phi^p + \sigma_{12}^s\phi^s\right)\left(N - N_2\right)\}\Delta t \qquad (2.21)\end{aligned}$$

Given that Δt is sufficiently small, the term in square brackets may be solved, using the values for I_p, I_s, $I_{ASE,f}$ and $I_{ASE,b}$ at time t. The finite-difference method therefore effectively de-couples the relevant differential equations.

The pump beam will initially be assumed as CW (equation 2.11), but the introduction of time-dependence into the differential equation for the intensity of the probe is necessary. In a similar fashion to that used to introduce transverse spatial coordinates, an intuitive approach may be applied for the introduction of the time-dependence. In the CW model the amplifying medium was subject to a probe beam, associated with some power or transverse intensity distribution. Similarly, the time-dependent model assumes the amplifying medium to be subject to a probe pulse, associated with some energy. This energy can be viewed as a power distribution with respect to time. If one therefore has an energy pulse of a certain shape (Gaussian, top hat, etc.), conventionally characterized by a FWHM-value, the effect of the amplifier on the pulse may be obtained by propagating the powers, distributed over time, through the medium consecutively. Each of the powers are broken up into their respective transverse intensity distributions as was done before and equation 2.12 without the geometrical gain term may be used to model the probe intensity.

Figure 2.21 illustrates the logic behind the time-dependent model for the case of square input probe pulse. The square pulse is divided into discrete powers, each associated with a temporal width of Δt, and are propagated through the gain medium. In between the propagation of consecutive powers the upper state population density is updated using equation 2.21. At the rear end of the crystal the individually propagated powers, each amplified to an unique extend depending on the available gain, are re-combined to form the output pulse.

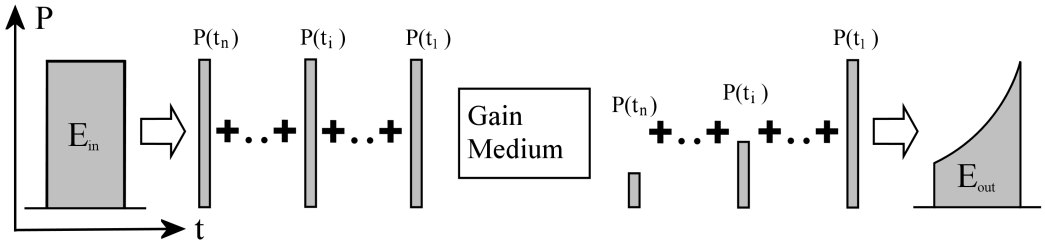

Figure 2.21: Procedure on which time-dependent model relies. The square pulse is divided into discrete powers which are propagated through the gain medium individually, starting from time t_1 and ending at time t_N. The amplified powers are re-combined to form the output pulse.

For a Gaussian input pulse, the power distribution is simply given by:

$$P(t) = P_0 e^{-2t^2/\sigma^2} \tag{2.22}$$

P_0 denotes the peak power, t the time and σ the $\frac{1}{e^2}$-radius of the pulse (time at which P_0 reduces by a factor $\frac{1}{e^2}$). The FWHM of a Gaussian pulse is related to its σ-value by the following expression:

$$\text{FWHM} = \sqrt{2\log_e(2)/\sigma^2} \tag{2.23}$$

The value of P_0 is chosen in such a way as to give the appropriate input pulse energy upon integration over time.

If the input pulse has a square power distribution as in Figure 2.21, it may be described in the usual way as:

$$P(t) = \begin{cases} P_0\,, \text{ if } -\text{FWHM}/2 \leq t \leq \text{FWHM}/2 \\ 0\,, \text{ if } |t| > \text{FWHM}/2 \end{cases} \tag{2.24}$$

The design of any amplifier is subject to a number of requirements, as was mentioned in the Introduction to this thesis. Specifically of interest is the amplification of ps-pulses. Typically, shorter pulses are accompanied by higher intensities which bring about a number of complications, most of which this model is unable to illustrate. The advantage of working with ps-pulses arises from the fact that spontaneous emission, and therefore ASE, are typically associated with lifetimes in the order of ns or even μs. The relatively long times associated with spontaneous emission means that the energy passes through the crystal in a very short time compared to the time it takes ASE to partially deplete the population inversion. In terms of computational difficulty, this bodes well, since ASE-effects may now be neglected and equations 2.14 and 2.15 may simply be removed from the model. The following section provides examples of the output from the time-dependent simulation, illustrating its usefulness in terms of design.

2.3.2 Typical output

The results from the time-dependent model follows in Figures 2.22 and 2.23 and have been obtained using the parameters of Table 2.3. The top hat pump beam with 30 W of initial power is focused in the center of the crystal of length 4 mm. The input probe pulse has a temporal profile with a FWHM of 30 ps and and an energy per pulse of 200 μJ. For Figures 2.22 and 2.23 the spatial intensity distribution of the probe pulse is Gaussian and is focused in the center of the crystal.

Figure 2.22 shows the Gaussian power distribution of the input pulse (dashed line) with respect to time and was recorded before the pulse entered the gain medium. The power distribution of the output pulse (solid line) with respect to time is also indicated and was recorded after amplification (behind the gain medium). The corresponding dynamics in the upper state population density (dash-dotted line) are plotted on the same graph as a function of time (right-hand side y-axis). The results for the upper state population density for the examples discussed here were recorded at an on-axis longitudinal position of 0.4 mm into the gain medium. An interesting observation is the shift in the central maximum of the output pulse with respect to that of the input pulse, indicated by the relative position of the vertical dotted lines. The shift in the central maximum is a result of the fact that the first half of the input pulse is amplified to a greater extent than the second half.

Symbol	Parameter	Value	Unit
L	Length of crystal	4	mm
N	Concentration of active atoms	1.5×10^{21}	cm^{-3}
τ	Spontaneous emission lifetime	951	μs
λ_p	Pump wavelength	941	nm
λ_s	Probe wavelength	1030	nm
σ_{12}^p	Pump absorption cross section	8.5×10^{-21}	cm^2
σ_{12}^s	Probe absorption cross section	1.3×10^{-21}	cm^2
σ_{21}^p	Pump emission cross section	0	cm^2
σ_{21}^s	Probe emission cross section	2.1×10^{-20}	cm^2
M_p^2	Pump beam quality factor	74	-
M_s^2	Probe beam quality factor	1.1	-
w_{0p}	Pump waist radius	100	μm
w_{0s}	Probe waist radius	50	μm
P_{0p}	Initial pump power	30	W
E_{in}	Initial probe pulse energy	200	μJ
FWHM_{in}	Initial probe pulse FWHM	30	ps
n	Yb:YAG refractive index	1.8	-

Table 2.3: Parameters used in the time-dependent simulation. An Yb:YAG crystal is used for the purpose of illustrating typical results.

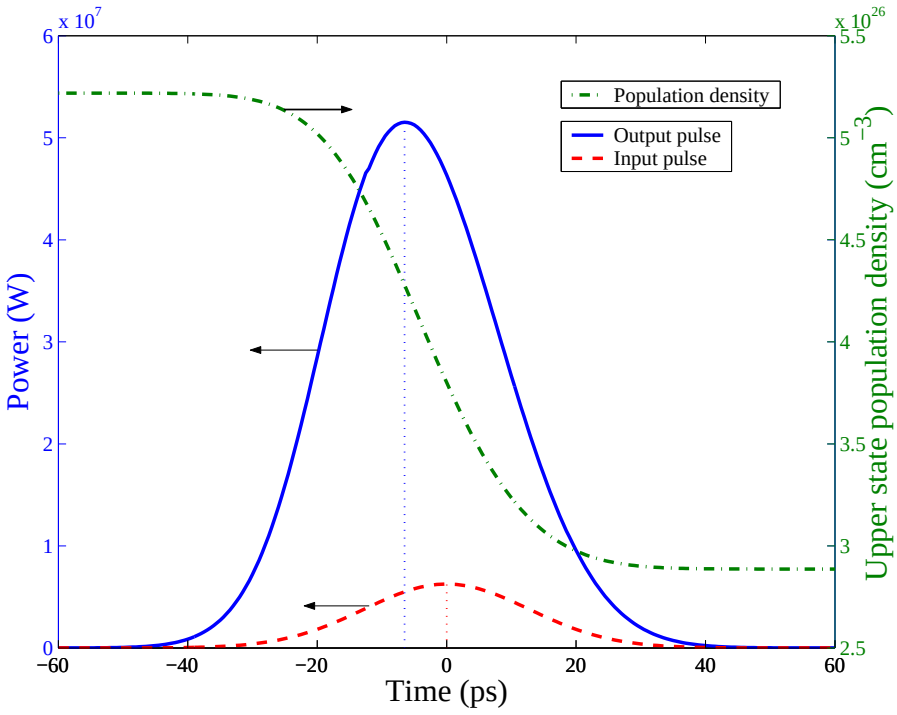

Figure 2.22: Gaussian input pulse (dashed line) giving rise to a non-Gaussian output pulse (solid line), shifted with respect to the temporal centre of the input pulse. The upper state population dynamics with respect to time is also indicated (dashed-dotted line).

In contrast with the input pulse (which is assumed to be a perfect Gaussian), the output pulse is no longer Gaussian or symmetric. The distorted shape of the output pulse is caused by the partial depletion of the upper state population density, illustrated by the dash-dotted line. In addition, the output pulse has a FWHM of 31.45 ps and an energy per pulse of 1.71 mJ, which translates into an energy gain of 9.33 dB.

Figure 2.23 shows a similar graph, but only this time for a top hat input pulse. The output pulse, as a result of the top hat input pulse, is severely distorted. The distortion in the output pulse is again due to the leading edge of the input pulse causing severe gain saturation, resulting in decreasing gain for the trailing parts of the input pulse.

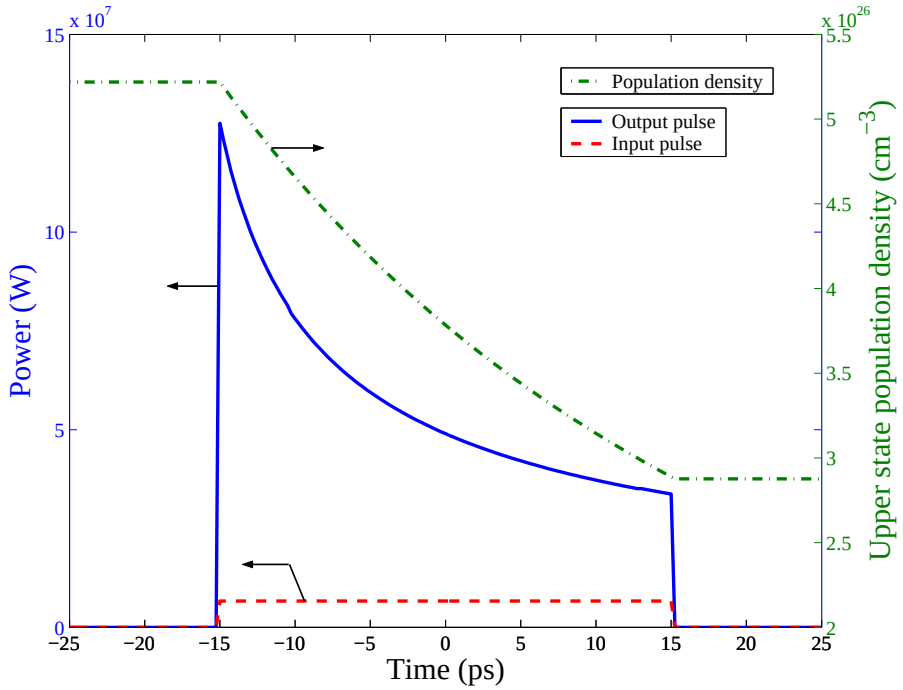

Figure 2.23: Top hat input pulse (dashed line) giving rise to a severely distorted output pulse (solid line). The upper state population dynamics with respect to time is also indicated (dashed-dotted line).

2.3.3 Dual-pass model

Amplifiers are often required to amplify probe pulses with initial energies in the order of μJ's up to the mJ-level. This means that the amplifier must be able to provide a gain of 30 dB. As will become apparent in later chapters, it is nearly impossible to obtain these levels of gain with only a single pass through the amplifying medium (depending of course on the medium that is being used). Often, multiple pulse-passes through an amplifier are also preferred in order to obtain a better energy extraction efficiency or to prevent pulse distortion as a result of gain saturation.

Although a number of complex, tried and tested, techniques exist (multi-pass amplifier, regenerative amplifier), it was decided to explore the case of a simple dual-pass amplifier. The modeling of a dual-pass amplifier involves a straight forward expansion of the preceding time-dependent model and is based on the following assumptions:

- The elapsed time between the first pass and the return pass is so short that the medium's population inversion does not have time to recover. This means that the pump is turned off from the moment the pulse exits the gain medium on its first pass up to the moment at which the pulse re-enters the gain medium for the second pass.
- The output energy per pulse for the first pass is used as input energy per pulse for the second pass.
- There is no pulse overlap inside the crystal. The second pulse is delayed until the first pulse has made its return pass.
- Free-space propagation and the mirror (used to reflect the pulse for the second pass) have no effect on the temporal shape of the pulse.
- The return pass follows the same spatial path as the first pass. This also implies that the propagation characteristics of the probe (waist size and M^2) remain unchanged.

Figure 2.24 illustrates a double-pass amplifier based on the preceding assumptions. Results are shown for a 5 mm crystal pumped with 30 W of power by a beam focused in the center of the crystal with a waist radius of 100 μm and an M_p^2 of 74. The top graph of Figure 2.24 (labeled (a)) shows a Gaussian input pulse (dashed line) with a FWHM of 30 ps and an energy of 20 μJ focused in the center of the crystal with a waist radius of 50 μm and an M_s^2 of 1.1. On the same graph the output pulse (solid line) is shown, and has a FWHM of 30.02 ps. The energy gain is 9 dB. The lower graph of Figure 2.24 shows the output pulse from (a), used as the input pulse for the second pass through the amplifier. The second pass results in an output pulse with a FWHM of 30.45 ps and an energy of 837 μJ. The total energy gain for both passes is therefore 16.22 dB. A closer look reveals that the relative shift between the maxima of the input and output pulses is greater for the second pass (see dotted lines). This makes sense, since a larger input energy would result in more severe gain saturation.

Figure 2.25 gives the upper state population density as a function of iterations for the double-pass simulation. The portion of the solid curve on the left-hand side of the first dotted line in Figure 2.25 depicts the convergence of the numerical processes. The portion between the dotted lines as well as that to the right of the second dotted line, show how the first and the second pass of the pulse decrease the population density, respectively. This decrease in the population density due to each pass corresponds to the stored energy extracted from the upper state population by the pulse and leads to the "steps" in the curve. The advantage of the double-pass geometry lies in the fact that a larger amount of gain is extracted without distorting the temporal shape of the pulse to an unacceptable extent.

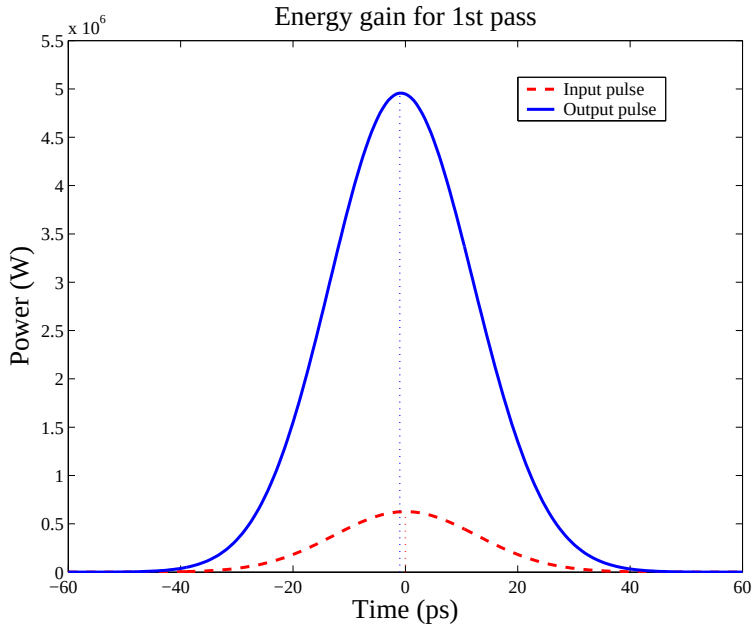

(a)

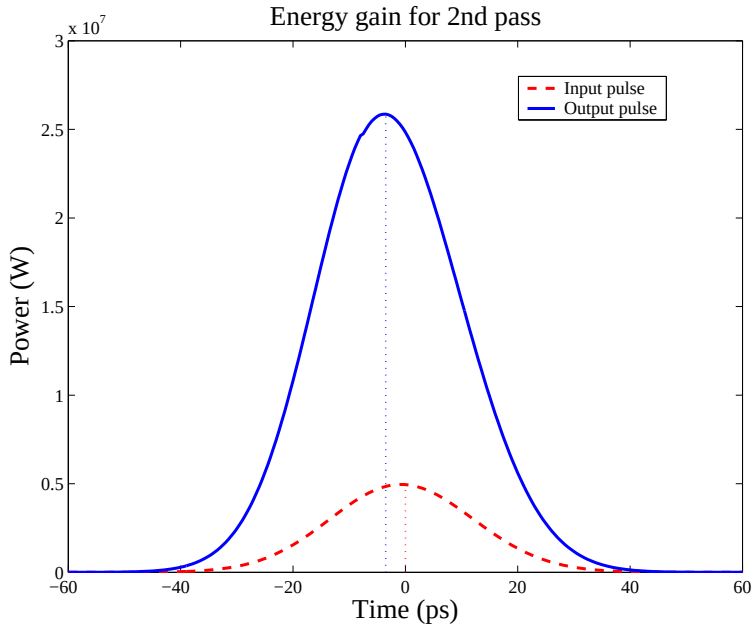

(b)

Figure 2.24: (a) Gaussian input pulse (dashed line) being amplified in the first pass through the amplifier. (b) The output pulse from *(a)* is used as the input pulse for the second pass through the amplifier.

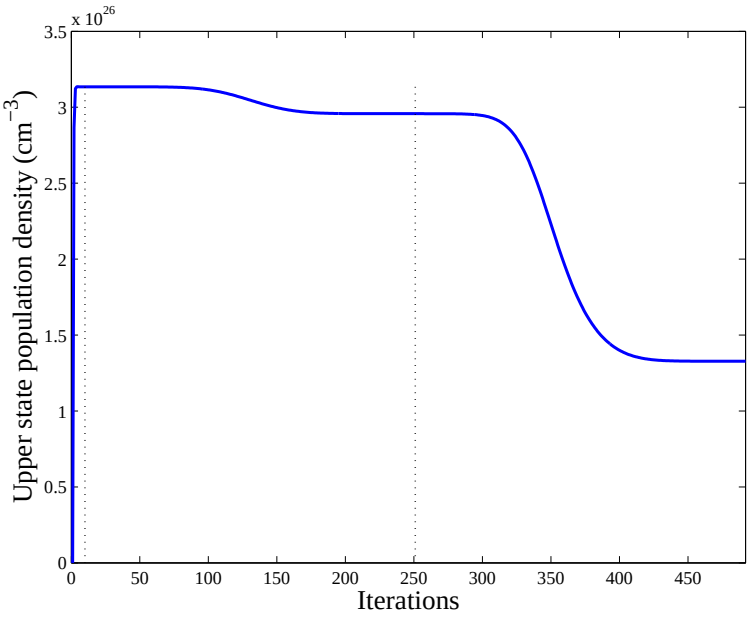

Figure 2.25: Upper state population density as a function of iterations. The first dotted line represents the transition from the phase where the numerical processes converge to the phase where the first pass is calculated. The second dotted line represents the transition between the calculation of the first and second pass.

Chapter 3

Verification of the models

The various numerical models of Chapter 2 give results that certainly look acceptable. However, since the models have to be used to design an Yb:YAG crystal, capable of amplifying pulses of a specific energy and FWHM, it is important to verify their predictions. Chapter 3 describes the procedures followed to verify the results of the CW model as well as the time-dependent model. Due to practical limitations, the verification of these two models had to be done separately and in different ways.

3.1 Experimental validation of continuous wave model

The CW model was experimentally verified making use of a Nd:YVO_4 crystal. Nd:YVO_4 was chosen due to the fact that it had been used in previous experiments at the University of Stellenbosch and was therefore readily available. Section 3.1 deals with a discussion of the basic properties of Nd:YVO_4 as well as the design and characterization of the experimental setup. The section is concluded by comparing the experimental results to that given by the CW simulation and establishing its usefulness.

3.1.1 Material properties of Nd:YVO_4

Nd:YVO_4 is an uni-axial, birefringent crystal and is well documented in the literature [31, 32]. Birefringence is the phenomenon whereby a medium has two different indices of refraction, depending on the polarization of the light. If, as will be the case here, the crystal is a-cut, unpolarized incident light is divided into a component parallel (π-polarization) and a component perpendicular (σ-polarization) to the c-axis (optical axis) [33]. Throughout Section 3.1 reference shall be made to these polarization components, since the properties of the medium greatly differ depending on the polarization.

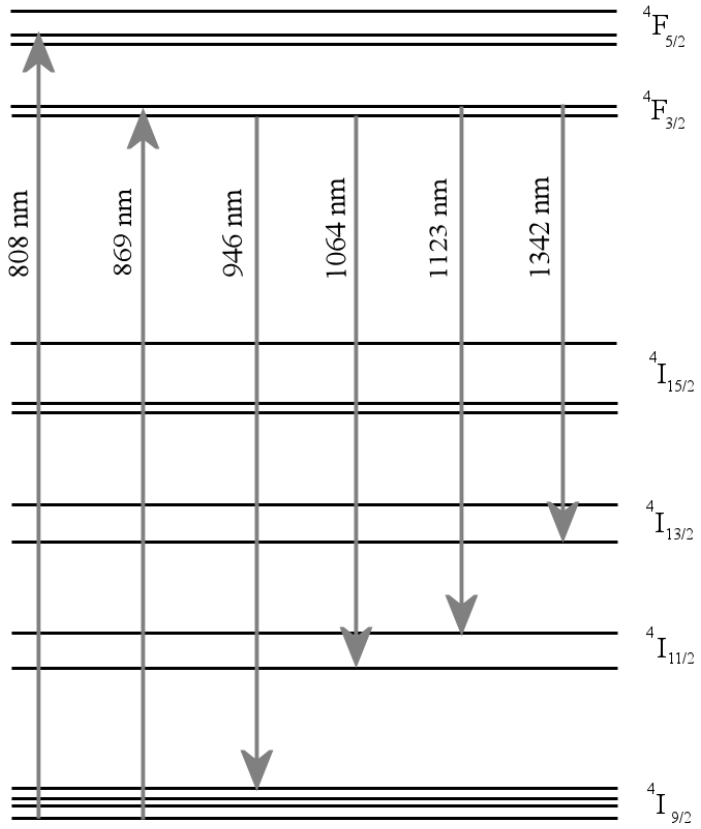

Figure 3.1: Energy level diagram for Nd:YVO_4.

The energy level diagram of Nd^{3+} in YVO_4 is shown in Figure 3.1, indicating the various transitions between the levels and the corresponding wavelengths. This energy level diagram resembles what was previously labeled as a four-state system (refer to Section 2.1.1). The manifold denoted by $^4I_{9/2}$ acts as the ground state and $^4F_{5/2}$ as the uppermost excited state. The transition between these two energy manifolds represents the pump transition at a wavelength of 808 nm. Transitions between the two manifolds labeled by $^4F_{3/2}$ and $^4I_{11/2}$ correspond to the lasing transitions of the medium at a wavelength of 1064 nm. Due to the birefringence, Nd:YVO_4 has separate absorption and emission spectra for the π- and σ-polarizations. The absorption and emission spectrum for the π-polarization are shown in Figures 3.2 and 3.3, respectively [34]. The absorption spectrum confirms the fact that the strongest absorption line is located at 808 nm with a cross section of 63×10^{-20} cm^2, which is much larger than the corresponding peak absorption cross section of 14×10^{-20} cm^2 in the σ-polarization. For the case of the emission spectrum, the largest cross section of 123×10^{-20} cm^2 is found at 1064 nm and dwarfs the cross section of 52×10^{-20} cm^2 (once again not indicated) for the σ-polarization. A property of interest is that the wavelength range for which absorption occurs is almost completely different from the range for which emission occurs (except for a weak mutual feature at 880 nm).

The implications of the relatively displaced absorption and emission spectra on the numerical model will be discussed in Section 3.1.4, but for now it can be said that this property is responsible for, what is referred to as, a low quantum efficiency (ratio of pump wavelength to probe wavelength). A low quantum efficiency is among other things responsible for heat generation within the crystal, which has the potential to influence laser action catastrophically (to be revisited in Section 4.2).

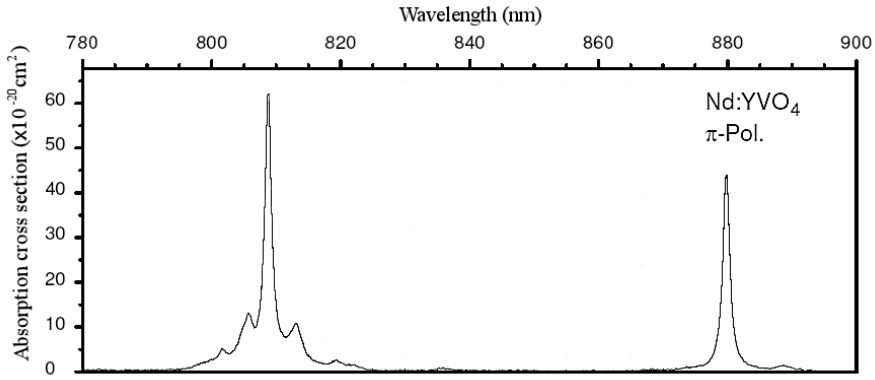

Figure 3.2: Absorption cross section spectrum for the π-polarization of Nd:YVO_4 [34]. The strongest feature is found at 808 nm.

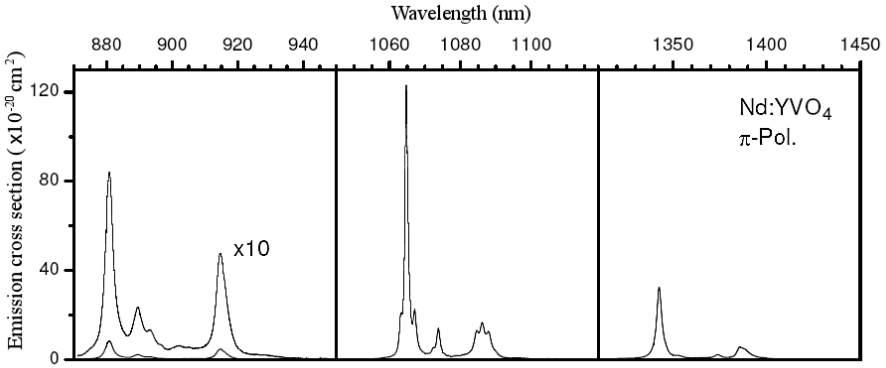

Figure 3.3: Emission cross section spectrum for the π-polarization of Nd:YVO_4 [34]. The strongest feature is found at 1064 nm.

As with the spontaneous emission lifetime of the upper state of 98 μs, the quoted cross sections (specified for 20°C) are dependent on the temperature of the crystal as well as the dopant concentration (Nd^{3+} concentration).

In Sections 3.1.2 and 3.1.3, the consequences of Nd:YVO_4's material properties are taken into consideration and manipulated in such a way as to promote better agreement between the assumptions made for the numerical model and what is seen in experiment.

3.1.2 Design of experimental setup

Nd:YVO_4 is ideally suited for diode pumping, due to the peak absorption wavelength of 808 nm. For the experiment about to be conducted, the pump source was chosen as a multi-mode fibre-coupled diode module (JenOptik) with a fibre core diameter of 400 μm and a numerical aperture (NA) of 0.22. The numerical aperture of a fibre is related to the half angle divergence, θ (refer to the angle between the dashed line and the optical axis in Figure 2.3), by the following:

$$\text{NA} = n \sin\theta \tag{3.1}$$

The half angle divergence is also defined as:

$$\theta = \frac{w}{z} \tag{3.2}$$

Making use of equation 2.9 and the far-field approximation, which requires that $w_{0p} << z$, the M_p^2 of the pump beam may be obtained from the numerical aperture and the core radius:

$$M_p^2 = \frac{(n \arcsin \text{NA})\, \pi w_{0p}}{\lambda} \tag{3.3}$$

Taking the refractive index of air (n) as unity, this leads to a theoretical value of $M_p^2 = 172.5$. An M_p^2 of this magnitude implies a beam that is far from Gaussian. In fact, the pump beam profile may be classified as a top hat with a waist radius of 200 μm at the fibre exit surface. Although the top hat assumption will prove to be accurate at certain positions along the optical axis, it is important to understand that the pump beam profile is position-dependent.

Since a very specific beam waist size is required at the crystal, it is necessary to use an appropriate method to design the pump beam propagation path. Gaussian optics provides the ideal tool, but requires a Gaussian intensity distribution equivalent to the top hat distribution obtained from the fibre. To obtain the equivalent Gaussian intensity distribution the second moment, or variance, may be used [20]:

$$\sigma_x^2 = \frac{\int_{-\infty}^{\infty}\int_{-\infty}^{\infty} (x - x_0)^2\, I(x,y)\, dx\, dy}{\int_{-\infty}^{\infty}\int_{-\infty}^{\infty} I(x,y)\, dx\, dy} \tag{3.4}$$

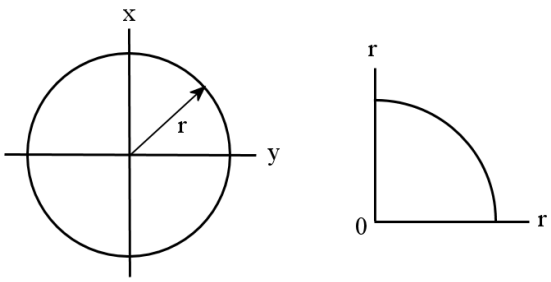

Figure 3.4: Image showing an aerial view of a top hat intensity distribution. The right-hand side represents a quarter of the top hat in polar coordinates and is used to calculate the variance via integration.

In equation 3.4, x and y again represent the transverse beam coordinates (with the optical axis along z) and x_0 denotes the center of gravity of the beam, defined as:

$$x_0 = \frac{\int_{-\infty}^{\infty}\int_{-\infty}^{\infty} xI\left(x,y\right)\,dx\,dy}{\int_{-\infty}^{\infty}\int_{-\infty}^{\infty} I\left(x,y\right)\,dx\,dy} \tag{3.5}$$

A similar equation to that of equation 3.4 can be written for the variance along the y-direction, but since an ideal top hat profile is symmetric, this is not necessary. An aerial view of an arbitrary top hat intensity distribution is given in Figure 3.4.
As can be seen, the center of gravity in both directions (x_0,y_0) is zero. The intensity distribution for the top hat is mathematically described by:

$$I\left(x,y\right) = \begin{cases} I_0\,, \text{ if } x^2+y^2 \leq r^2 \\ 0\,, \text{ if } x^2+y^2 > r^2 \end{cases} \tag{3.6}$$

Making use of polar coordinates,

$$\begin{aligned} x &= r\cos\theta \\ y &= r\sin\theta \\ r^2 &= x^2+y^2 \end{aligned} \tag{3.7}$$

and calculating the Jacobian (equation 3.8), the integral in the numerator of the variance equation (equation 3.4) is solved for one quarter of the top hat profile, making use of its symmetry. The solution to the numerator of equation 3.4 is given in 3.9.

$$J = \left|\frac{\partial\left(x,y\right)}{\partial\left(r,\theta\right)}\right| \tag{3.8}$$

$$\int_0^{\pi/2}\int_0^{r} I_0 r^3 \cos^2\theta \, dr \, d\theta = I_0 \frac{\pi}{16} r^4 \tag{3.9}$$

Multiplying this result by a factor of 4 and solving the integral in the denominator of the variance equation in a similar way, the standard deviation in the x-direction follows:

$$\begin{aligned} \sigma_x &= \sqrt{\frac{I_0 \frac{\pi}{4} r^4}{I_0 \pi r^2}} \\ &= \frac{r}{2} \end{aligned} \tag{3.10}$$

The waist radius of a real top hat beam is related to the standard deviation simply by $w_0 = 2\sigma$ [20], where $\sigma = (\sigma_x + \sigma_y)/2$. The result therefore is:

$$w_0 = r \tag{3.11}$$

Although the result of equation 3.11 may seem intuitive since the beam was assumed to be top hat, it does provide a rigorous mathematical formulation of finding the waist radius of the equivalent Gaussian beam for any non-TEM_{00} beam.

Now that the top hat beam obtained from the pump source has been related to a Gaussian beam with waist radius r, Gaussian optics can be used to design the beam propagation path. However, since this beam has an $M_p^2 = 172.5$, the concept of the embedded Gaussian [20] can be used. The embedded Gaussian ($w_{0,emb}$) does not have any physical meaning, but represents an ideal Gaussian beam of $M_p^2 = 1$, propagating within the real beam. The waist size of the embedded Gaussian is given by:

$$w_{0,emb} = w_0 / M_p \tag{3.12}$$

The embedded Gaussian is useful especially when propagating a beam through a system of optical elements (such as lenses), because the real beam will respond to these elements in the exact same way as the embedded Gaussian. Afterwards, the actual spot size radii can be retrieved from the embedded Gaussian spot size radii by multiplication of a factor M_p.

The spot size radius of the embedded Gaussian is calculated at every z-coordinate, starting from the exit face of the fibre, by transforming the Gaussian beam's complex radius of curvature (equation 2.7). At the exit of the fibre, acting as the first waist in the beam propagation path, the complex radius of curvature is denoted q_0 (refer to Section 2.1.2).

At each of the following z-coordinates, the complex radius of curvature is updated, making use of the following equation:

$$q_{new} = \frac{Aq_0 + B}{Cq_0 + D} \tag{3.13}$$

The letters A to D are elements of the so-called ABCD-matrices. Each ABCD-matrix represents the effect of a particular optical element through which the beam propagates. If, for instance, the Gaussian beam is propagated through a distance, L, of free space, followed by propagation through a thin lens of focal length f (> 0 for convex lens), the final ABCD-matrix used in equation 3.13 is given by:

$$\begin{bmatrix} A & B \\ C & D \end{bmatrix} = \begin{bmatrix} 1 & 0 \\ -\frac{1}{f} & 1 \end{bmatrix} \begin{bmatrix} 1 & L \\ 0 & 1 \end{bmatrix} \tag{3.14}$$

The first matrix on the right-hand side of equation 3.14 denotes the last optical element through which the beam is propagated (thin lens). From equation 2.7 in Section 2.1.2, the spot size radius of the beam is obtained from the imaginary part of the new complex radius of curvature:

$$w_{emb} = \sqrt{\frac{i\lambda q_{new}}{\pi}} \tag{3.15}$$

Finally, the real beam is characterized by the following spot size radii:

$$w = w_{emb} M_p \tag{3.16}$$

It was decided that the pump beam for the Nd:YVO_4 experimental setup should have a spot radius of 200 μm on the front surface of the crystal. The design shown in Figure 3.5 is fairly straight forward and resembles 1:1 imaging. The dashed lines indicate the position of the convex lenses with radius 2.5 cm. The 1:1 imaging is intended to give a top hat pump profile at the waist (front surface of crystal). This result, which is supported by Fourier optics, is consistent with the result obtained from an analysis with the software package GLAD (Appendix). The GLAD simulation indicates that, given a top hat profile of spot radius 200 μm at the exit face of the fibre, the pump profile at the waist will be top hat with a spot radius of approximately 215 μm.

The probe source for the experiment was chosen as a Nd:YAG laser (Lightwave electronics) with a perfect beam quality ($M_s^2 \simeq 1$). Because the pump spot size had already been decided upon, the ideal spot size for the probe, also focused on the front surface of the crystal, may be deduced using the usual guideline, $D \sim 3W$ [20]. This guideline states that 99% of the power in the probe beam will be transmitted through an "aperture" (D) with a diameter three times bigger than the diameter of the probe beam (W).

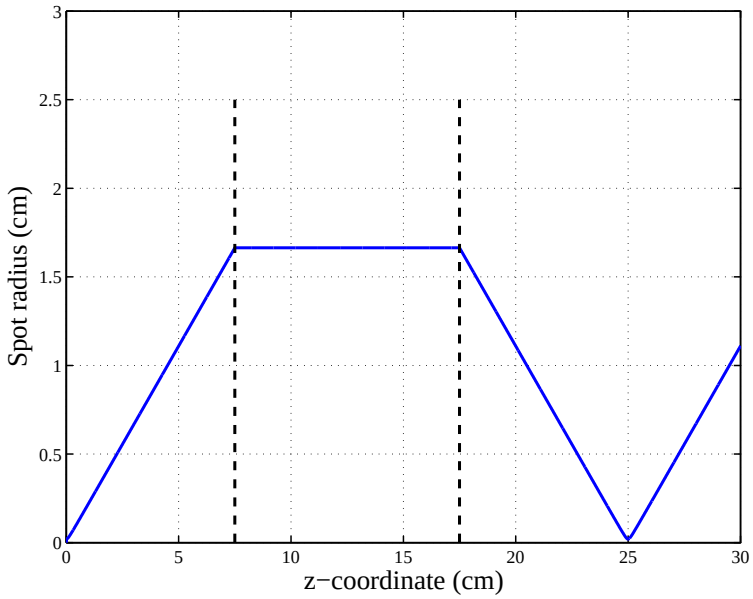

Figure 3.5: Optical design for the pump beam. The dashed lines indicate the position and radius of the convex lenses. The waist radius is obtained as 200 μm.

Taking the diameter of the pump beam as the aperture, the probe beam was chosen to have a waist radius of ± 60 μm. The beam propagation path for the probe source was designed using a similar approach to that used for the pump beam. Section 3.1.3 describes the experimental setup and the validity of the beam propagation path designs.

3.1.3 Experimental setup and characterization

The experimental setup, based on the designs of Section 3.1.2, is shown in Figure 3.6. The unpolarized diode beam passes through a polarizing beam splitter (BS) and a $\frac{1}{2}$-wave plate (1/2-WP), thereby polarizing the beam into the π-orientation. The pump beam then proceeds through two convex lenses (L), coated for high transmission in the wavelength regions of 808 nm and 1064 nm, whereby it is focused through the dichroic mirror (D) and onto the front surface of the Nd:YVO_4 crystal. The dichroic mirror is coated for high transmission at 808 nm as well as high reflection at 1064 nm. Both the second convex lens and the crystal are placed on translation stages (TS) for alignment purposes, but also to determine whether the distance between the first and second lens have any influence on the pump spot size. The Nd:YVO_4 crystal is water cooled by a chiller (Neslab) and is kept constant at 20°C. The probe beam passes through a convex lens (L) on a translation stage and is reflected by the dichroic mirror before it is also focused on the front surface of the crystal.

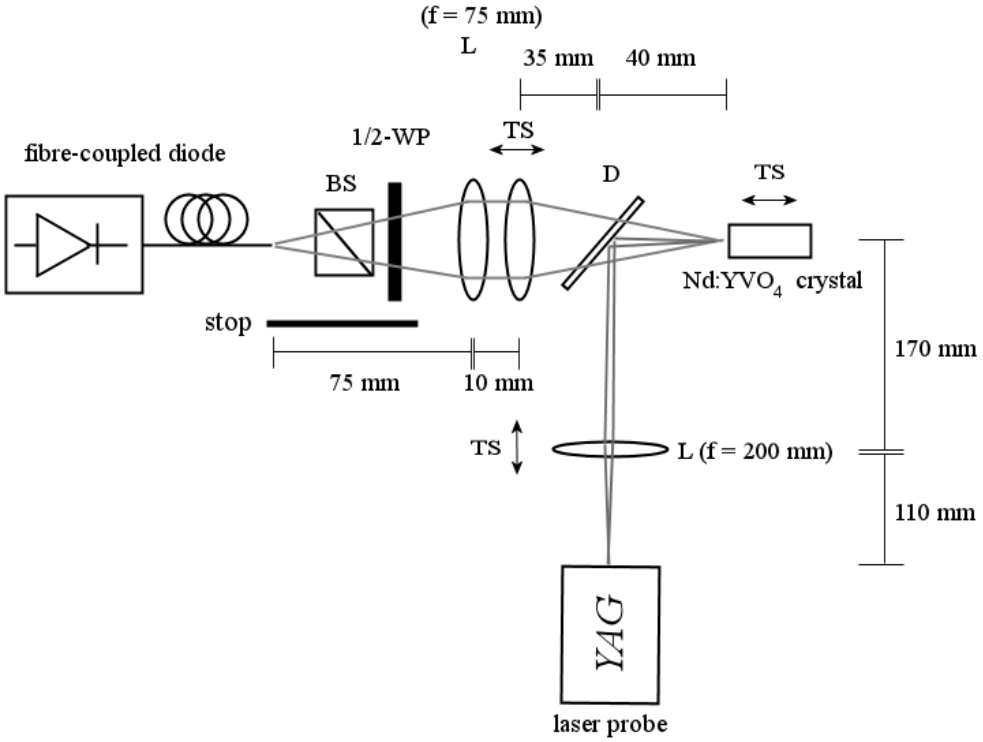

Figure 3.6: Experimental setup for simple amplifier.

As mentioned in Section 3.1.2, the validity of the assumption that the pump beam is top hat is position dependent. It was however chosen that the beam should have a top hat profile at the waist, on the front surface of the crystal. The pump beam is polarized in the π-orientation, albeit at the expense of half of the available pump power. This was done because the π-polarization has an absorption cross section (and also an emission cross section) that is significantly bigger than its σ-polarization counterpart, thereby causing the π-polarized pump light to have a shorter absorption length inside the crystal. A shorter absorption length means that most of the pump power is absorbed while the top hat assumption is approximately valid, increasing the accuracy of the simulation for comparative purposes.

Characterization of the pump beam

As a first step towards characterizing the polarized diode beam, the electro-optical properties are calibrated. A graph of the electro-optical properties of the pump source is shown in Figure 3.7 and gives the actual power incident upon the crystal for the pump beam propagating through all the optical elements in the beam propagation path. The diode module is water-cooled and kept at a temperature of $\pm 23^{o}$C (using a chiller). Due to the difficulty of tuning the temperature with sufficient accuracy, the output power from the diode at different temperatures (at a constant current), was not investigated, although the manufacturers indicate a weak dependence.

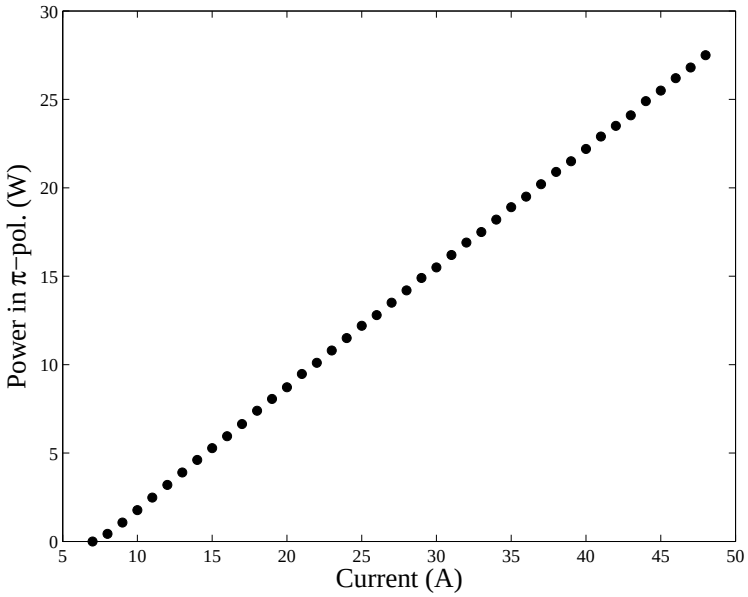

Figure 3.7: Electro-optical properties of pump diodes at ±23°C.

The output power from the diode module influences the central wavelength component of the pump radiation significantly. This effect was investigated using a spectrometer (Ocean Optics) and the results are given in Figure 3.8. It was found that the wavelength of the pump light varies between 802.25 nm and 805.75 nm. The variation in the pump wavelength implies that the absorption cross section of Nd:YVO_4 will be substantially lower than anticipated (refer to Figure 3.2) and will also be dependent on the output power from the diodes.

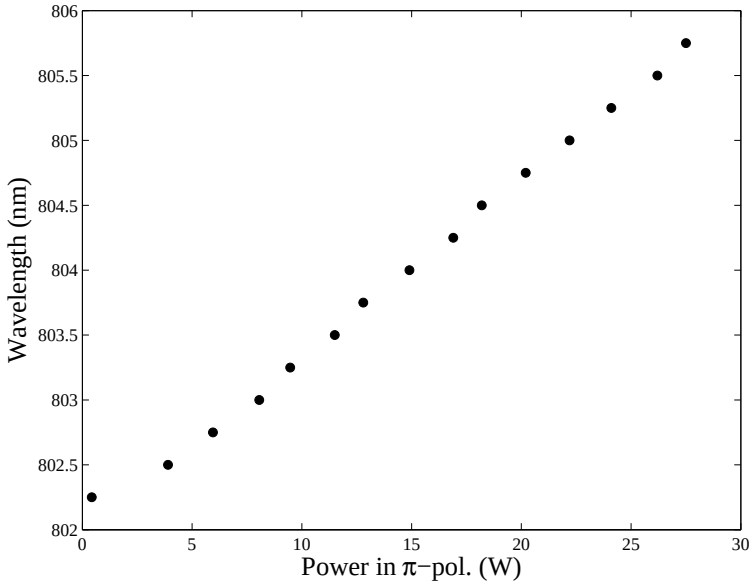

Figure 3.8: Power dependence of wavelength for pump diodes at ±23°C.

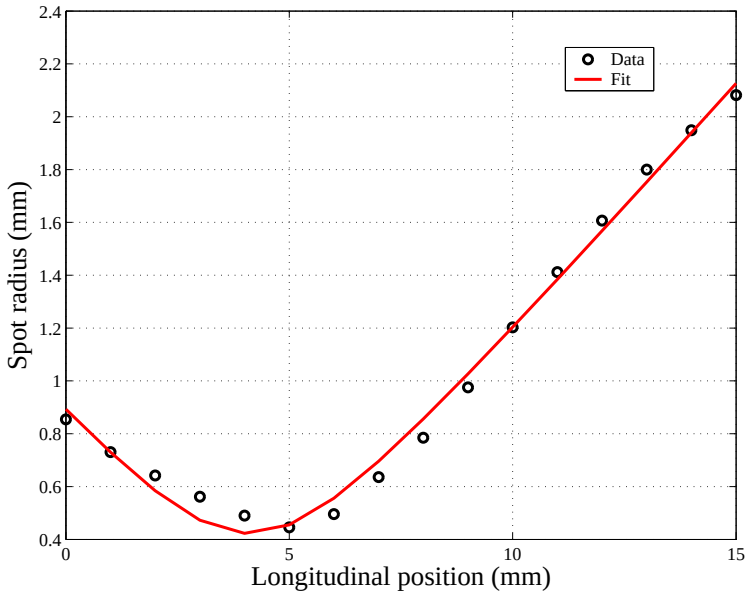

Figure 3.9: Measured pump beam propagation path used for M_p^2-calculation.

To ensure that the pump beam propagation path has been designed with the necessary accuracy, the beam is scanned using a CCD camera (Coherent Laser Cam IIID). Since the spot size of the beam can be measured by the camera's software, the beam-scan method can be used to trace out the beam, locate the waist and determine the beam quality of the pump beam. However, due to the fact that the CCD camera is extremely sensitive to bright light (such as a laser), it is often necessary to include various neutral density filters (HOYA) and beam dividers into the beam propagation path to avoid saturation of the CCD. The disadvantage of using neutral density filters is that they, more often than not, introduce distortion in the beam, being observed on the CCD as background noise. Background noise causes the software of the camera to malfunction when calculating the spot size at a given position along the optical axis and some improvisation is required. Using an image processing technique, the photos stored by the CCD camera were broken down into matrices, with the value of each matrix element representing the relative intensity at the corresponding position within the photo. After removing most of the background noise, by making use of a simple algorithm, the second moment of the remaining intensity is calculated in accordance with equation 3.4. Again use was made of the relation between the spot radius and the standard deviation and a discrete beam propagation path was constructed about the waist position with as little as ten points. The discrete points were then fitted with equation 2.9, using the M^2 as a fitting parameter. Figure 3.9 gives the resulting beam propagation path. The beam has a waist radius of 422 μm, a Rayleigh range of 4 mm and $M_p^2 = 314$. This waist radius and M_p^2-value are both much larger than were indicated by the Gaussian optical design as well as GLAD. The reason for the discrepancy may be a result of severe spherical aberration caused by the use of spherical lenses at low effective f-numbers (as opposed to aspherical or gradient index lenses).

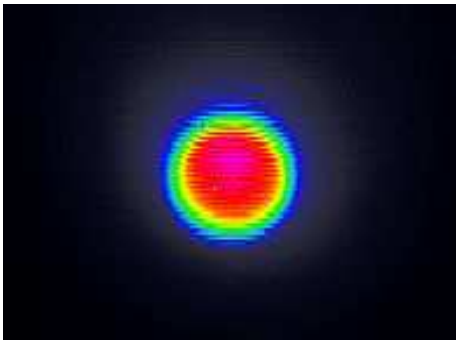

Figure 3.10: Top hat profile of pump beam at waist. 60% of the power is contained in an area with a radius of 200 μm.

After further image processing, it was found that the profile at the waist of the pump beam closely resembles a top hat and contains 60% of the pump power within a top hat region with a radius of 200 μm, despite the measured waist radius of 422 μm (Figure 3.10).

Characterization of the probe beam

The probe laser for the Nd:YVO_4 experiment is also water-cooled to a constant temperature of 20°C by the same chiller used to maintain the temperature of the crystal. The electro-optical properties of the probe source (Figure 3.11) are optimized for operation at a temperature of 20°C and the output power has a central wavelength of 1064 nm, in perfect correspondence to the peak emission line of Nd:YVO_4.

The probe laser has very good beam quality described by an $M_s^2 \simeq 1$. In order to use the same technique used for the pump beam, to determine whether this M_s^2-value is indeed accurate, some changes are required. The probe beam cannot just be measured for the actual beam propagation path due to the small waist size. The waist size of the beam is simply so small and intense that it is firstly, very difficult to attenuate the beam to a sufficient degree to avoid saturation of the CCD without significant distortion. Secondly, it is impossible to accurately determine the second moment of the beam because of the small number of CCD pixels illuminated by the probe beam. For the purpose of confirming the beam quality, the probe beam was allowed to diverge through the intended waist (position of front surface of crystal) onto a lens fixed on a translation stage. This lens was then tuned until an appropriate waist size was found and the data could be processed as before. The results for this are given in Figure 3.12 and yields an $M_s^2 = 1.14$.

Since the actual probe waist size could not be calculated using the camera, a number of conventional methods were employed. The first method is called the scanning slit method, whereby a power meter (Coherent) and a slit with a width in the order of μm's, are both fixed to a translation stage. The position of the slit corresponds to the position of the waist and the translation stage is used to scan across the beam in discrete steps, taking measurements of the power at each step. Secondly, the knife-edge method uses an open slit (or knife edge) to scan across the width of the beam, with the power meter behind it at a fixed position.

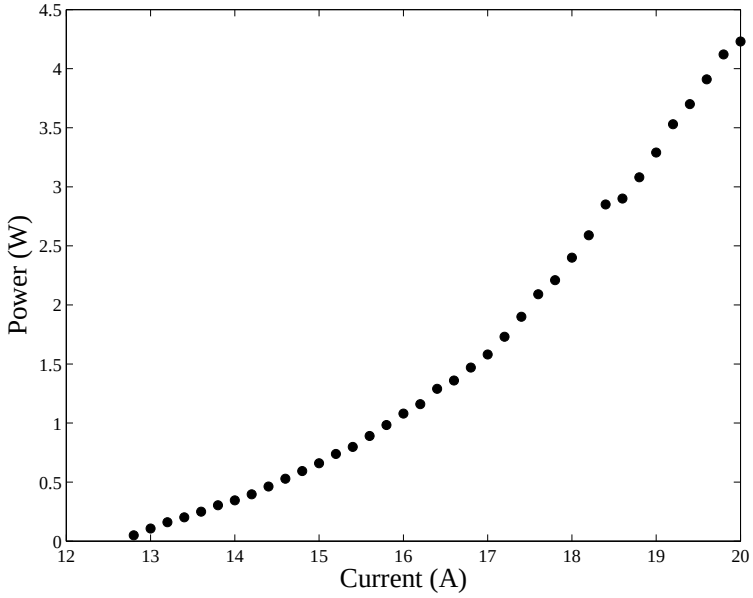

Figure 3.11: Electro-optical properties of the probe laser at 20°C.

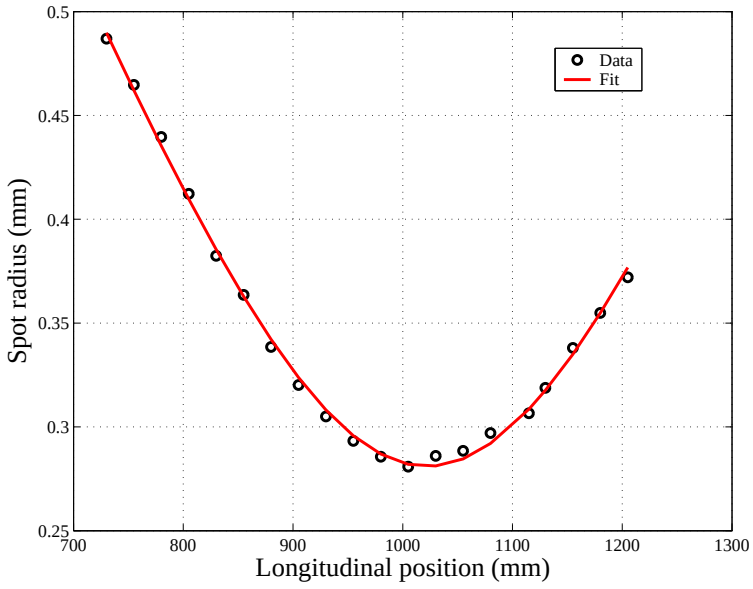

Figure 3.12: Measured probe beam propagation path used for M_s^2-calculation. The experimental setup used was build especially for the purpose of measuring the beam quality and should not be mistaken for the actual beam propagation path.

The profile obtained from the power measurements is a monotonously increasing one, but upon differentiation a Gaussian profile is obtained with a spot radius corresponding to the beam waist radius. A third method, based upon that of the knife edge, describes a procedure whereby the beam's spot size can be obtained by taking the relative position coordinates of the open slit where the power equals 84% of the peak power and 16% of the peak power, respectively. For the third method the power meter also remains stationary and the two position coordinates are used, together with the beam's M^2 and a correlation constant, to obtain a waist radius corresponding to the beam's second moment.

The three methods were used at different positions along the optical axis in an attempt to measure the waist radius, but the results of a waist radius ranging between 95 μm and 150 μm are inconclusive. A possible reason for the inconclusive measurements for the probe waist radius is the relatively large translation stage resolution of 10 μm.

Characterization of the amplifying medium

The Nd:YVO_4 crystal has a length (L) of 12 mm ($4 \times 4 \times 12$ mm) and is specified to have a dopant concentration of 0.425 at.%. This dopant concentration translates into a stoichiometric composition given by:

$$\mathrm{Nd}_f \quad : \quad \mathrm{Y}_{1-f}\mathrm{VO}_4 \tag{3.17}$$

In equation 3.17, $f = 0.425/100$ represents the fraction of Yttrium atoms (Y) replaced by Neodymium atoms (active atoms). The dopant concentration can now be related to the total active atom concentration (N) using the following:

$$N \quad = \quad \frac{\rho f A}{M} \tag{3.18}$$

M denotes the molar mass ($204\,\mathrm{g\,mole^{-1}}$) of Nd:$YVO_4$ for the specified dopant concentration, A is Avogadro's number ($6.022 \times 10^{23}\,\mathrm{mole^{-1}}$) and ρ is the host density ($4.22\,\mathrm{g\,cm^{-3}}$). This yields an active atom concentration of $N = 5.3 \times 10^{19}\,\mathrm{cm^{-3}}$.

The value for N can also be investigated by absorption measurements. Assuming that the pump radiation decreases at an exponential rate (unsaturated absorption), the output power transmitted by the crystal is related to the input power simply by:

$$P_{out} \quad = \quad P_{in} e^{-\sigma N L} \tag{3.19}$$

Equation 3.19 can be solved for N, since both the input (P_{in}) and output power (P_{out}) can be measured and the corresponding wavelength and cross section are known. Using this approach, the value for N was obtained as 2.1×10^{19} $\mathrm{cm^{-3}}$.

Although this value for N is less than half that of the specified value, the comparison between the experimental and simulated results, to follow in Section 3.1.4, verifies the measured value.

3.1.4 Comparison of results

Table 3.1 gives the final parameters the Nd:YVO_4 simulation is based upon. It is important to note that the values indicated for the pump wavelength and pump absorption cross section in Table 3.1 are only applicable to the case where the initial pump power value stays constant. For a changing pump power, the values for the pump wavelength and pump absorption cross section were adjusted in correspondence to Figures 3.8 and 3.2. The values for N, M_p^2 and w_{0s} in the simulation were varied for the purpose of matching the experimental results. The measured value for N and the specified M_p^2-value (172) led to a good comparison between the experimental and numerical results, while the optimum probe waist radius was taken as 72 μm.

Symbol	Parameter	Value	Unit
L	Length of crystal	12	mm
N	Concentration of active atoms	2.1×10^{19}	cm^{-3}
τ	Spontaneous emission lifetime	98	μs
λ_p	Pump wavelength	804.75	nm
λ_s	Probe wavelength	1064	nm
$\sigma_{12}^{p,\pi}$	Pump absorption cross section	11.6×10^{-20}	cm^2
$\sigma_{12}^{s,\pi}$	Probe absorption cross section	0	cm^2
$\sigma_{21}^{p,\pi}$	Pump emission cross section	0	cm^2
$\sigma_{21}^{s,\pi}$	Probe emission cross section	123×10^{-20}	cm^2
M_p^2	Pump beam quality factor	172	-
M_s^2	Probe beam quality factor	1.14	-
w_{0p}	Pump waist radius	200	μm
w_{0s}	Probe waist radius	72	μm
P_{0p}^{π}	Initial pump power	20	W
P_{0s}^{π}	Initial probe power	0.16	W
n	Nd:YVO_4 refractive index	2	-
	ASE wavelength range	$1060 \rightarrow 1070$	nm
	Number of wavelength intervals	100	

Table 3.1: Parameters for the Nd:YVO_4 simulation. The values indicated for the pump wavelength, pump absorption cross section and initial pump power were used to generate Figure 3.14, while the value for the initial probe power is specific to Figure 3.13.

Figures 3.13 and 3.14 show a comparison between the experimental results and the results obtained from the CW simulation with transverse coordinates, for two cases. In Figure 3.13, the input pump power is varied while keeping the input probe power constant, monitoring the gain at every power level. The comparison is very good except for the fact that the simulated results seem to saturate to a lesser degree than the experimental results.

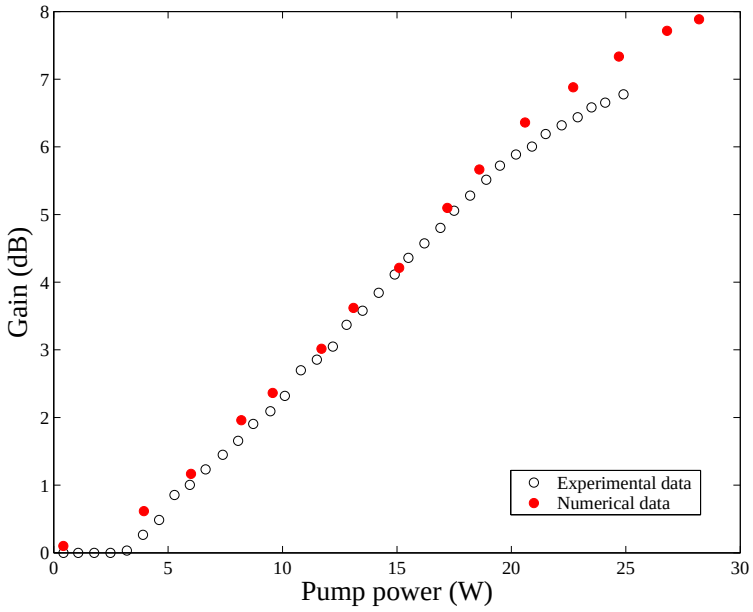

Figure 3.13: Dependence of gain on pump power in a Nd:YVO_4 amplifier. The solid circles represent the numerical results and the blank circles those obtained from the experiment.

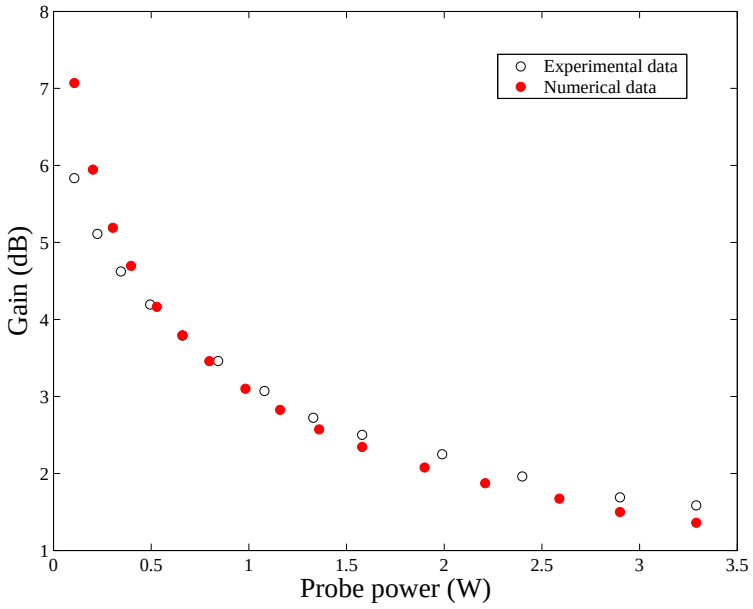

Figure 3.14: Saturation characteristics of the Nd:YVO_4 amplifier. The solid circles represent the numerical results and the blank circles those obtained from the experiment.

Similarly, Figure 3.14 show the case of the input probe power being varied while keeping the input pump power constant, monitoring the gain at every power level.
Once again it is in the high-gain limit where a comparison of the results shows the largest difference.

Error bars for the measured results of Figures 3.13 and 3.14 are smaller than the size of the circles (this also apply to all other experimental results given in this work). The difference between the experimental and simulated results at high pump powers may be explained at the hand of upconversion.

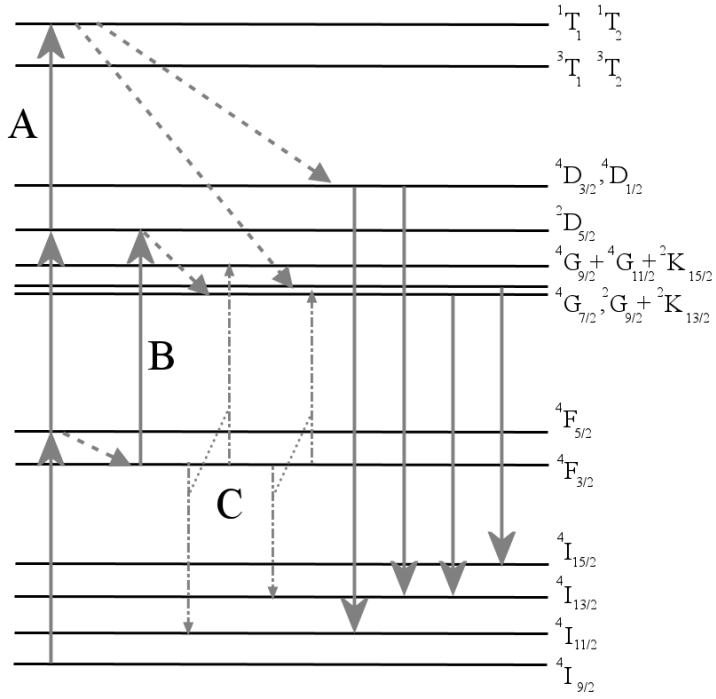

Figure 3.15: Schematic representation of upconversion mechanisms in Nd:YVO_4 [35].

The influence of upconversion on diode end-pumped Nd:YVO_4 crystals is well documented in the literature [36, 37, 35]. Upconversion is the process responsible for the generation of photons with higher energies than the photons leading to excitation (pump light) and work via three mechanisms. The mechanisms will be discussed through the use of Figure 3.15 with specific reference to the transitions labeled by A, B and C [35]. Transition A is a two-step process called three-photon excitation. Firstly, one pump photon is absorbed resulting in the atom being excited from the ground state up to level $^4F_{5/2}$ (also refer to Figure 3.1). The atom then simultaneous absorbs two more pump photons and is excited to level $^1T_2$. The dashed lines in Figure 3.15 refer to the non-radiative relaxation taking place from level $^1T_2$ into levels $^4D_{3/2}$ and $^4G_{7/2}$ or $^2G_{9/2}$ + $^2K_{13/2}$, from which the so-called upconversion emission takes place. Transition B, known as excited-state absorption (ESA), refers to the process whereby the absorption of a pump photon leads to the excitation of Nd^{3+} from $^4F_{3/2}$ (previously identified as the upper laser level) to level $^2D_{5/2}$. Levels $^4G_{7/2}$ and $^2G_{9/2}$ + $^2K_{13/2}$ are again populated through non-radiative relaxation, leading to upconversion emission. The last mechanism is indicated by the transitions in C (dash-dotted lines).

Cooperative energy-transfer is the process whereby an atom donates part of its energy to a neighboring atom, called the acceptor. The donor atom's energy is lowered, while the acceptor atom is excited to a higher energy state. In Nd:YVO_4 this mechanism populates the $^4G_{7/2}$ and $^4G_{9/2} + {}^4G_{11/2} + {}^2K_{15/2}$ energy levels, resulting in upconversion emission from the same levels as in transition B.

ESA has very weak cross sections for the case of diode pumping at $\pm$800 nm and therefore has a negligible influence on Nd:YVO_4 laser performance [36]. The other two mechanisms for upconversion however lead to a reduced upper state population density ($^4F_{3/2}$) and may therefore influence laser action significantly. The extent to which upconversion influences the gain dynamics is proportional to the pump power [36]:

$$I_u \propto I_p^m \tag{3.20}$$

In equation 3.20, I_u refers to the upconversion intensity, while m gives the slope of the pump intensity dependence. Upconversion thus provides a possible explanation for the disagreement between the experimental and numerical results in Figures 3.13 and 3.14, as a result of the upconversion intensity's dependence on the pump intensity.

At this stage it is worth pointing out the value of the comparison between the numerical and experimental results. Due to the crystal that was chosen, the experiment was performed in a low-gain regime (by the standards of Nd:YVO_4). Figure 3.16 shows a simulated comparison between results obtained by considering the effect of ASE (solid line) and by neglecting the effect of ASE (dashed line) for (a) a typical low-gain case (as in the experiment) and (b) a typical high-gain case. This comparison illustrates the severe manner in which ASE saturates the gain in the high-gain limit. As opposed to this, the low-gain limit shows negligible differences between the cases with and without ASE. It may therefore immediately be concluded that the comparison between the experimental and simulated results does not verify the ASE aspect of the numerical model quantitatively.

Despite the observed differences between the experimental and numerical results at high gain and the fact that no substantial conclusions can be made about the way in which the ASE was modeled, the comparison certainly verifies the CW numerical model as a tool that can be used to design an appropriate laser crystal for a given application.

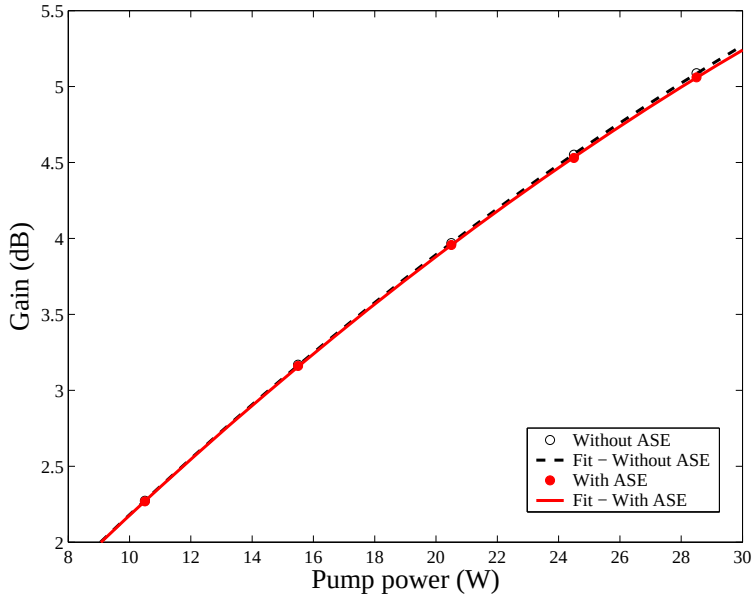

(a)

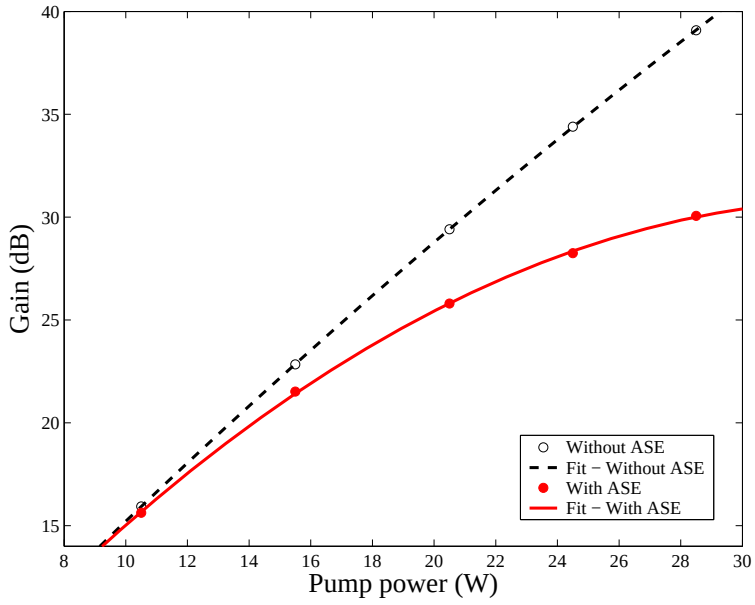

(b)

Figure 3.16: The influence of ASE at (a) low gain and (b) high gain. For both figures a dashed line is used to indicate results simulated without the effect of ASE, whilst a solid line is used for the results that account for ASE.

3.2 Theoretical validation of time-dependent model

The time-dependent model was verified using an analytical approach, commonly known in the literature as the Frantz-Nodvik model for pulse amplification [38]. The Frantz-Nodvik model is often cited in papers dealing with various aspects of pulse amplification [39, 40, 41, 32, 42, 43] and despite the fact that it was published over forty years ago, it still remains a valuable tool for benchmarking. This section deals with the basic properties of the Frantz-Nodvik model and will conclude with a comparison between predictions from their paper and results from the time-dependent numerical model.

3.2.1 The Frantz-Nodvik model

The following pages give the assumptions and mathematical structure on which the Frantz-Nodvik model is based and comes from their paper titled "Theory of pulse propagation in a laser amplifier". For a full mathematical derivation, see [38].

The analytical model considers a probe beam incident on an amplifying medium of length L, consisting of two states (refer to Figure 1.1). $N_1(x,t)$ and $N_2(x,t)$ denote the number densities of active atoms in the ground and excited states respectively. The probe beam's photon density is denoted by $n(x,t)$, where x represents the propagation coordinate along the optical axis. If the pulse is short relative to the radiative lifetime of the excited state, as is the case here, spontaneous emission may be neglected. Referring to the discussion at the start of Chapter 2, pure two state systems have $\sigma_{12} = \sigma_{21} = \sigma$, giving rise to the following coupled, non-linear time-dependent radiation transfer equations:

$$\frac{\partial \Delta}{\partial t} = -2\sigma c n \Delta \tag{3.21}$$

$$\frac{\partial n}{\partial t} + c\frac{\partial n}{\partial x} = \sigma c n \Delta \tag{3.22}$$

In equations 3.21 and 3.22, use was made of the definition of the population difference (inversion), $\Delta = N_2 - N_1$, while c indicates the speed of light in the medium. For a two-state system with no additional losses it also follows that $N_2 + N_1 = \text{constant}$.

For an arbitrary set of boundary conditions (initial conditions) for the population difference and photon density, Frantz and Nodvik derived general solutions to equations 3.21 and 3.22. For the sake of comparing the numerical results from the simulation to the analytical predictions of Frantz and Nodvik, only solutions to the special case of a square (top hat) pulse will be considered. The input photon density of this square pulse of duration τ is subject to the following:

$$n(0,t) = n_0(t) = \begin{cases} n_0\,, & 0 \le t \le \tau \\ 0\,, & \text{otherwise} \end{cases} \tag{3.23}$$

n_0 denotes a constant magnitude for the photon density. The population inversion is initially assumed to be uniform throughout the length of the medium:

$$\begin{aligned} N_2(x,-\infty) - N_1(x,-\infty) &= \Delta_0(x) \\ &= \Delta_0\ ,\ 0 \leq x \leq L \end{aligned} \tag{3.24}$$

Similarly, Δ_0 is a constant magnitude for the initial inverted population. The solution to the position- and time-dependent photon density is simply obtained by using the boundary conditions of equations 3.23 and 3.24 and the general solution is given by:

$$n(x,t) = n_0 / \left[1 - \left(1 - e^{-\sigma\Delta_0 x}\right) e^{-2\sigma\eta(t-x/c)/\tau}\right]\ ,\ 0 \leq t - \frac{x}{c} \leq \tau \tag{3.25}$$

If the transformed coordinate $t - \frac{x}{c}$ does not correspond to the given range of equation 3.25, the photon density has a zero value at that position and time. The constant $\eta = n_0 c\tau$ represents the total number of photons per unit area in the pulse.

The photon density, $n(x,t)$, is also related to the intensity, $I(x,t)$, by:

$$I(x,t) = n(x,t)\, c\hbar\omega \tag{3.26}$$

Equation 3.26 establishes a connection between equations 3.21 and 3.22 and the rate equations and transport equation (equations 1.26 and 1.30, respectively) which were derived at the end of Chapter 1 and form the basis of the simulation equations. Subjecting the equations of Chapter 1 to the same assumptions made for equations 3.21 and 3.22, we find that the pump term and terms corresponding to collisions (including spontaneous emission) are omitted, leaving:

$$\begin{aligned} \frac{\partial N_1}{\partial t} &= \frac{\sigma I}{\hbar\omega}(N_2 - N_1) \\ \frac{\partial N_2}{\partial t} &= -\frac{\sigma I}{\hbar\omega}(N_2 - N_1) \end{aligned} \tag{3.27}$$

$$\frac{1}{c}\frac{\partial I}{\partial t} + \frac{\partial I}{\partial x} = \sigma I (N_2 - N_1) \tag{3.28}$$

Of course, since the numerical model uses a finite-difference method to model temporal dynamics, the time-dependence within equations 3.27 are required to be rewritten as was done in equations 2.20 and 2.21, yielding:

$$N_1(t + \delta t) = N_1(t) + \frac{\sigma I}{\hbar\omega}(N_2 - N_1)\,\delta t \tag{3.29}$$

$$N_2(t+\delta t) = N_2(t) - \frac{\sigma I}{\hbar\omega}(N_2 - N_1)\,\delta t \tag{3.30}$$

The constant δt in equations 3.29 and 3.30 labels the temporal resolution for the finite-difference procedure. Due to the fact that the boundary conditions are specified in terms of the population inversion, these equations may be rewritten for simplicity to resemble a finite-difference inversion equation:

$$\begin{aligned} N_2(t+\delta t) - N_1(t+\delta t) &= N_2(t) - N_1(t) - 2\frac{\sigma I}{\hbar\omega}(N_2 - N_1)\,\delta t \\ \Delta(t+\delta t) &= \Delta(t) - 2\frac{\sigma I}{\hbar\omega}(N_2 - N_1)\,\delta t \end{aligned} \tag{3.31}$$

Equation 3.28 is handled in the same way as in Section 2.3.1. This means that the Frantz-Nodvik model and the numerical model are now based on the same set of equations and assumptions, differing only in the methods of solving. The platform has thus been provided for a sensible comparison.

3.2.2 Comparison of results

In order to reproduce the analytical predictions of Frantz and Nodvik, as intended, the same parameter values (corresponding to the same type of amplifying medium) should be used. A comparison was done for a square input pulse in two distinct cases. For the first of these cases, the probe beam, with $\eta = 4 \times 10^{18}$ photons cm^{-2}, enters the ruby amplifying medium of length 10 cm at time t. The initial population of the amplifying medium is assumed to be completely excited, corresponding to an inversion population given by $\Delta_0 = 8 \times 10^{18}$ cm^{-3}. Using a cross section of $\sigma = 2.5 \times 10^{-20}$ cm^2, typical for ruby at room temperature, the analytical predictions and numerical results for the photon density of the amplified probe beam, exiting the medium at time $t = \frac{L}{c}$, can be calculated. Figure 3.17 shows the results. The output photon density at every time step is normalized to the input photon density and effectively gives the energy gain (dimensionless) from the ruby crystal at that time. The time itself has been normalized to the pulse width, τ. Figure 3.18 shows the same graph for the second case, where all the parameters have the same values, except for $\eta = 4 \times 10^{19}$ photons cm^{-2}, i.e. a larger input photon density. In Figures 3.17 and 3.18 the analytical predictions are indicated by circles, while the solid line represents the simulated results. The shape of the graphs has already been discussed at the end of Chapter 2. All that the graphs actually provide is a comparison between the analytical predictions and numerical simulation that is nearly perfect (irrespective of the value for η). It can therefore safely be said that the time-dependent numerical model gives results that are sensible and in good agreement with known theory.

As explained, the comparison between the analytical predictions and numerical results required that the rate equations and propagation equations upon which the simulation is based be subject to the same assumptions that are used in the analytical model.

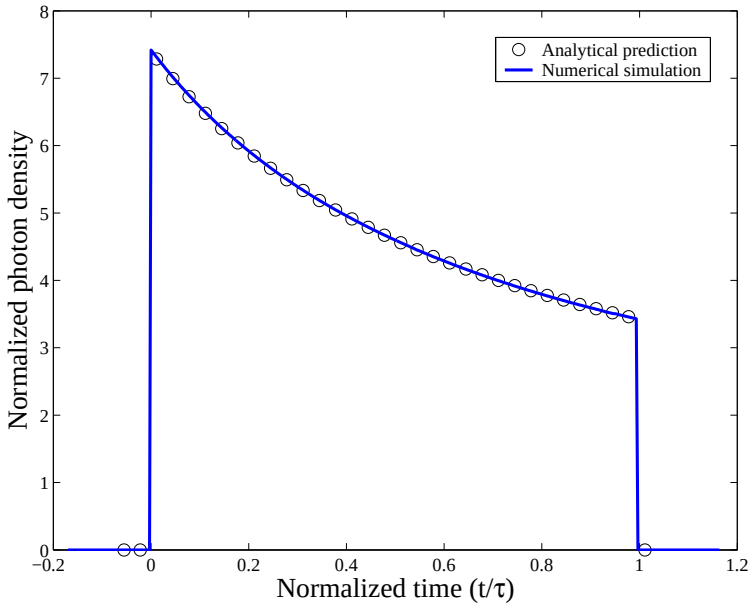

Figure 3.17: Normalized photon density at the exit surface from the ruby crystal at different times, normalized to the pulse width ($\eta = 4 \times 10^{18}$ photons cm^{-2}).

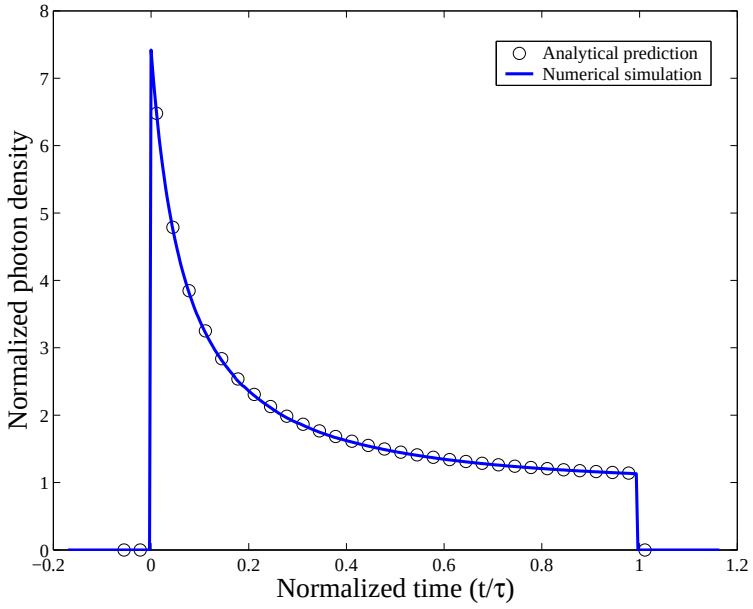

Figure 3.18: Normalized photon density at the exit surface from the ruby crystal at different times, normalized to the pulse width ($\eta = 4 \times 10^{19}$ photons cm^{-2}).

The simulation is however capable of producing results with better accuracy in comparison to what is observed experimentally, due to the fact that these assumptions are not necessary. For instance, the numerical model is capable of simulating the gain experienced by a probe pulse as a result of passing through a crystal with more than two energy states (although it is eventually modeled as a two-state system), which means that it accommodates different cross sections for absorption and emission. Additionally, the numerical model can take full account of, not only spontaneous emission, but also amplified spontaneous emission, should the pulse length be long enough. The simulation further takes account of possible re-absorption of probe photons as well as the effect of possible pump absorption during the amplification process.

With both the CW and time-dependent numerical models verified to a certain extent, these models are now implemented as tools in the design of an amplification medium, subject to a number of design constraints. The experiment following the design stage will also serve as an excellent final test for the models and is the topic of discussion in Chapter 4.

Chapter 4

The Yb:YAG experiment

The numerical models developed in Chapter 2 and verified in Chapter 3 are now used to investigate the amplifying properties of Yb:YAG. The investigation is performed by first exploring a number of different crystals, subject to different pumping conditions, with the CW simulation. The optimum design according to the CW simulation is then explored with the time-dependent simulation to get an idea of the energy gain that can be achieved with this crystal. In addition to the optical properties, the thermal properties of Yb:YAG are also investigated using a pseudo-engineering approach. Chapter 4 is concluded with a discussion of the experimental setup and experimental results.

4.1 Design of Yb:YAG crystals

In contrast to Nd:YVO_4, Yb:YAG can be labeled as a quasi-three-state system. The implications of a quasi-three-state energy level scheme for the rate equations are discussed in Section 4.1.2. The remainder of Section 4.1 is dedicated to results from the models, illustrating the manner in which certain variables influence the performance of such an amplifier.

4.1.1 Material properties

Ytterbium-doped YAG is a material that has been studied extensively in terms of its performance as a laser medium. Yb:YAG has been compared to YAG doped with various other dopant ions [25], but remains an excellent choice for laser action due to a number of reasons [44, 45, 46]:

- The absorption band of Yb:YAG is ideally suited for InGaAs diode pumping.
- Processes such as excited-state absorption (ESA) and cross-relaxation are absent, leading to increased laser efficiency.
- A broad emission band allows for the generation of ultra-short pulses.
- Due to the small difference between the pump wavelength and the lasing wavelength, Yb:YAG has a very small quantum defect (refer to Section 3.1.1).

- The host medium, YAG, is optically isotropic with a high thermal conductivity and excellent mechanical stability.

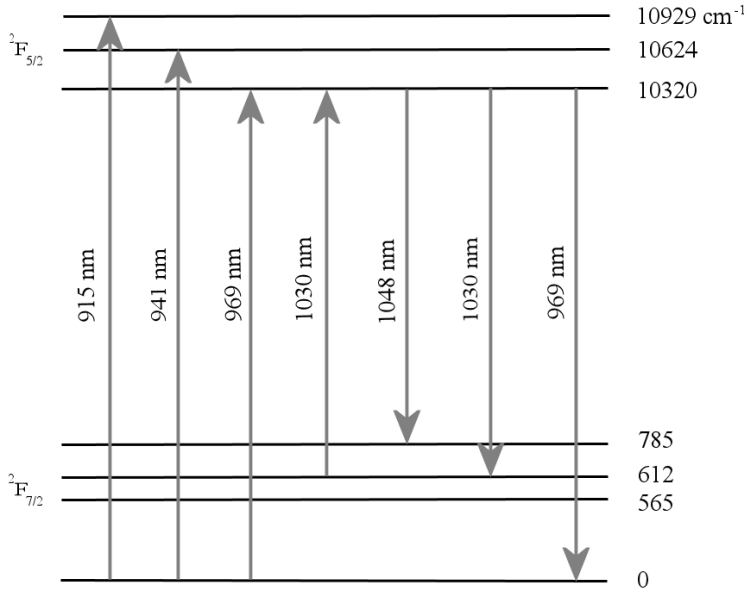

Figure 4.1: Energy level diagram for Yb:YAG [46].

The energy level scheme of Yb:YAG is given in Figure 4.1 and clearly shows the large energy difference between the lowest level in the $^2F_{7/2}$ manifold and the three excited levels in the same manifold which is responsible for the so-called quasi-three-state nature of the material [46].

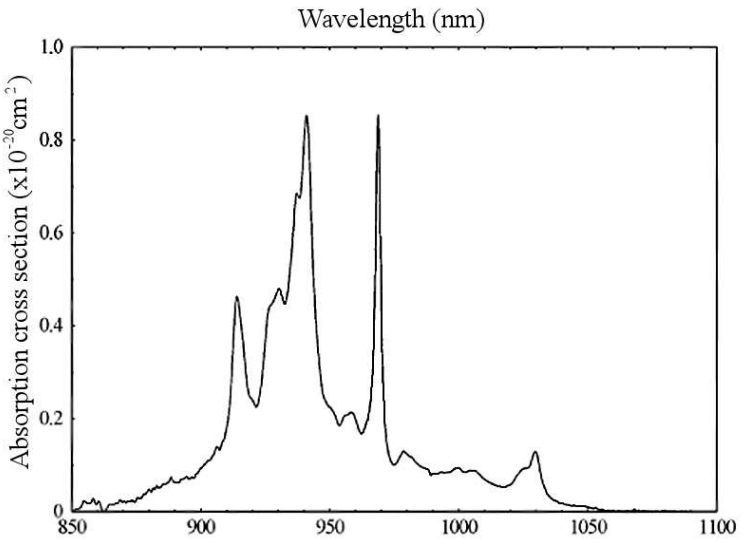

Figure 4.2: Absorption cross section spectrum of Yb:YAG. The strongest feature is found at 941 nm [47].

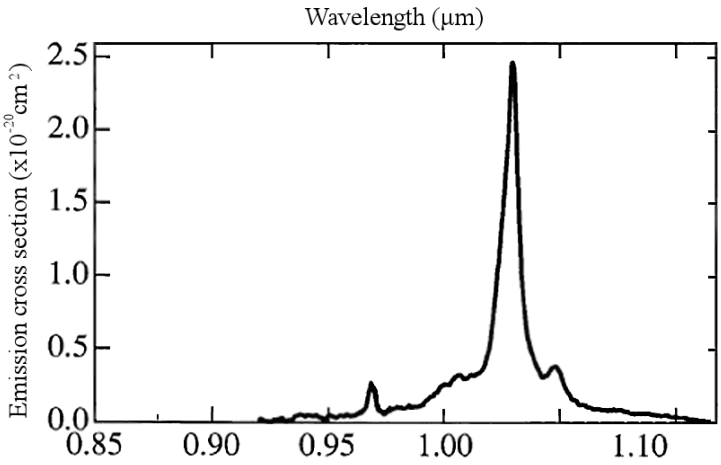

Figure 4.3: Emission cross section spectrum of Yb:YAG. The strongest feature is found at 1030 nm [48].

As is evident from Figures 4.2 and 4.3 which shows the absorption and emission spectra of Yb:YAG at 27°C ([47] and [49, 48]) respectively, the strongest absorption line is at 941 nm, whilst the 1030 nm transition dominates lasing action. The peak absorption cross section (8.5×10^{-21} cm^2) and emission cross section (2.1×10^{-20} cm^2) are small compared to the cross sections previously quoted for Nd:YVO_4. Due to the large spontaneous emission lifetime of 951 μs [44] associated with the upper state, Yb:YAG has an excellent energy storage capacity [50] and is therefore of great use as a pulse amplifier.

4.1.2 Implications on the population rate equations

One of the disadvantages of working with Yb:YAG is that the absorption cross section spectrum overlaps the emission cross section spectrum (compare Figures 4.2 and 4.3). In the case of overlapping cross section spectra, emission corresponding to the 1030 nm, and also the 969 nm, transitions may act in reverse and re-populate the upper state. The re-populating effect can also be seen by looking at the energy level diagram of Figure 4.1. The process by which atoms from the lower state are excited, decreases the amount of pump as well as probe photons available for pumping and amplification, respectively. Although this so-called re-absorption may indeed be subject to stimulated emission with time, a portion of the excited atoms will lead to spontaneous emission and therefore decreases the gain achievable.

Despite the fact that the quasi-three-state system of Yb:YAG is modeled as a two-state system, the numerical simulation accommodates possible re-absorption (absorption at the lasing wavelength) as well as emission at the pump wavelength. These processes are represented by σ_{12}^s and σ_{21}^p respectively in the model equations of Chapter 2. Although emission at the pump wavelength is neglected for the purpose of simulating the Yb:YAG amplifiers, re-absorption is included.

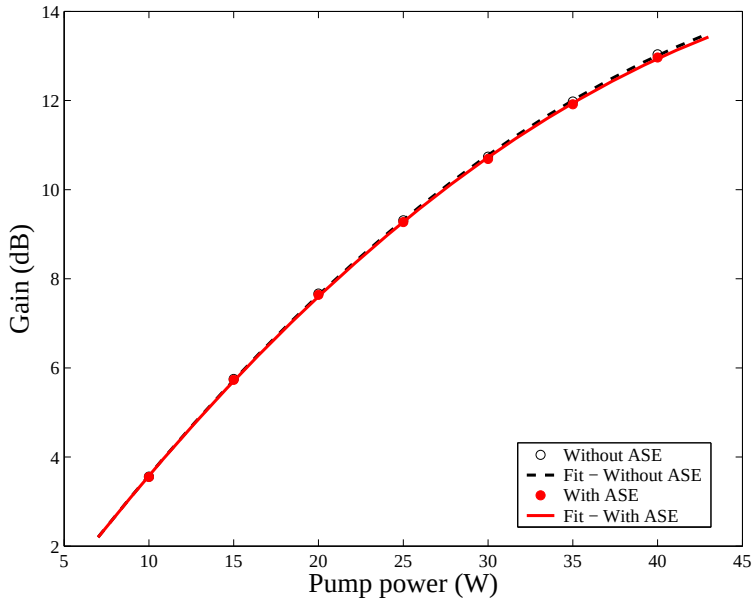

Figure 4.4: The influence of ASE at high gain. A dashed line is used to indicate results simulated without the effect of ASE included, whilst a solid line is used for the results that account for ASE as well.

In investigating the characteristics of Yb:YAG using the CW numerical model, it is found that the influence of ASE is basically negligible, even in the high gain limit. Increasing the FWHM of the Lorentzian function, used to model the cross sections for the ASE, to 20 nm, the difference between the results including the effect of ASE (solid line) and the results neglecting ASE (dashed line) remains very small (Figure 4.4). The only plausible explanation for the small amount of ASE, lies in the large spontaneous emission lifetime of the upper state of Yb:YAG, resulting in very little spontaneous emission being available for amplification. Due to the large spontaneous emission lifetime, the model equations of Chapter 2 may be adapted to neglect the effect of ASE, resulting in a considerable decrease in computational time.

4.1.3 Results from the continuous wave model

The design criteria for the development of the Yb:YAG amplifier, using the CW numerical model as tool, may be summarized as follows:

1. Choose a specific length of crystal that will enable ease of handling. A longer crystal will ensure better thermal contact between the amplification medium and the water-cooled mount, leading to reduced temperature build-up.

2. Calculate the active atom concentration (N). A larger active atom concentration may be used with a shorter crystal to obtain the same amount of amplification as can be obtained from a smaller active atom concentration and a longer crystal.

3. Due to re-absorption, the gain experienced by the probe is not necessarily a maximum at the end of the crystal for all crystal lengths. It is therefore required to choose a length of crystal, with its corresponding active atom concentration, that ensures a maximum gain at the rear surface of the crystal.

4. Since the degree to which thermal effects influences the performance of the amplifier is a concern, an attempt is made to keep the thermal gradients along the optical axis to a relative minimum. This is approached by designing the amplifier in such a manner that 15% of the pump power remains unabsorbed at the rear surface of the crystal (Transmission ≥ 0.15).

The dopant concentration (at.%) is related to the active atom concentration by equation 3.18. In the case of Yb:YAG $f = 3F$, where $F = (\text{dopant concentration})/100$. The expression for f comes from the stoichiometric composition of Yb:YAG, given by:

$$\mathrm{Yb}_F \quad : \quad \mathrm{Y}_{3-F}\mathrm{Al}_5\mathrm{O}_{12} \tag{4.1}$$

In addition to the design criteria, the available pump power is limited to 30 W, thereby effectively limiting the gain that can be extracted from the crystal. Since this crystal should be able to amplify output pulses from a fibre laser (energy per pulse in the nJ regime) up to the mJ regime, a double pass amplifier may very well be necessary in order to obtain enough gain (refer to Section 2.3.3).

For the purpose of numerically evaluating different crystals , the pump and probe sources for the experiment have to be identified first. As a pump, a multi-mode fibre-coupled diode module (JenOptik) was chosen. The fibre delivering the pump light has a diameter of 200 μm and a numerical aperture of 0.22 which translates into a theoretical M_p^2 of 74 (using equation 3.3). An in-house built fibre laser is used as a probe and has a measured M_s^2 of 1.1.

Making use of the design criteria, a large number of crystals were evaluated using the CW model with the pump beam focused at different positions within the crystal. It was found that the position of the pump beam's focus influences the gain substantially for a constant crystal length and active atom concentration. For active atom concentrations ranging from 4×10^{26} m^{-3} to 7×10^{26} m^{-3}, the optimum pump beam focus lies 2 mm beyond the front surface of the crystal, but shifts towards 1 mm beyond the front surface of the crystal for concentrations ranging from 9×10^{26} m^{-3} to 15×10^{26} m^{-3}. The simulation parameters kept constant in all of the designs and the variables of the two optimum designs are shown in Tables 4.1 and 4.2 respectively.

Symbol	Parameter	Value	Unit
τ	Spontaneous emission lifetime	951	μs
λ_p	Pump wavelength	941	nm
λ_s	Probe wavelength	1030	nm
σ_{12}^p	Pump absorption cross section	8.5×10^{-21}	cm^2
σ_{12}^s	Probe absorption cross section	1.3×10^{-21}	cm^2
σ_{21}^p	Pump emission cross section	0	cm^2
σ_{21}^s	Probe emission cross section	2.1×10^{-20}	cm^2
M_p^2	Pump beam quality factor	74	-
M_s^2	Probe beam quality factor	1.1	-
w_{0s}	Probe waist radius	50	μm
P_{0p}	Initial pump power	30	W
P_{0s}	Initial probe power	1×10^{-7}	W
n	Yb:YAG refractive index	1.8	-

Table 4.1: Constant parameters for all the Yb:YAG designs.

Initially the pump beam's waist radius, w_{0p}, was kept constant at 100 μm, but once the two optimum designs had been identified, the power gain's dependence on the pump waist radius was investigated. The power gain as a function of pump waist radius for the two optimum designs are given in Figure 4.5 and the optimum values are indicated in Table 4.2.

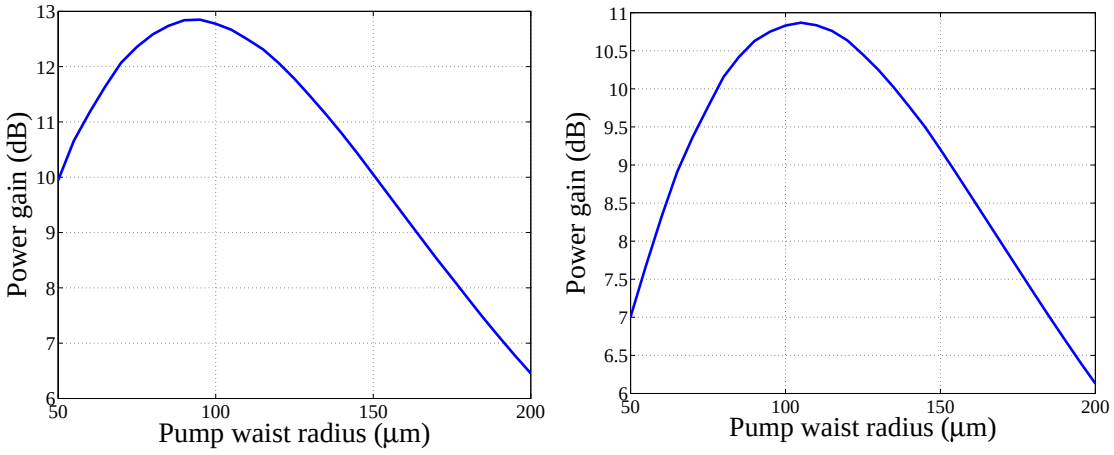

(a) (b)

Figure 4.5: Gain dependence on pump waist radius for (a) $N = 9 \times 10^{26}$ m^{-3} and (b) $N = 7 \times 10^{26}$ m^{-3}. A higher dopant concentration corresponds to a smaller optimum pump waist radius.

N (m^{-3})	L (mm)	Pump focus position (mm)	w_{0p} (μm)	Gain (dB)
9×10^{26}	4	1	90	12.84
7×10^{26}	5	2	105	10.87

Table 4.2: Important parameters for the two optimum Yb:YAG designs.

The fact that the pump waist radius is smaller for a larger dopant concentration makes sense. A higher dopant concentration means more active atoms per unit volume and more active atoms mean that a smaller volume, or at least cross-sectional area (waist), is required to absorb the available pump power.

The relevant results for the two optimum CW simulation designs are given in Figures 4.6 and 4.7. Both sets of results satisfy the design criteria in terms of transmission and gain. The slope of the curves, indicating the pump power absorption, furthermore indicates satisfactory thermal gradients. The slope of the curves in Figures 4.6 and 4.7 should be compared to that of Figure 2.8, where 50% of the pump power is absorbed in less than a third of the crystal's length. Since possible crystal fracture is a concern and the emphasis is on following a cautious experimental approach to investigate the Yb:YAG medium, the crystal with length 5 mm and $N = 7 \times 10^{26}$ m^{-3} was chosen as the final design.

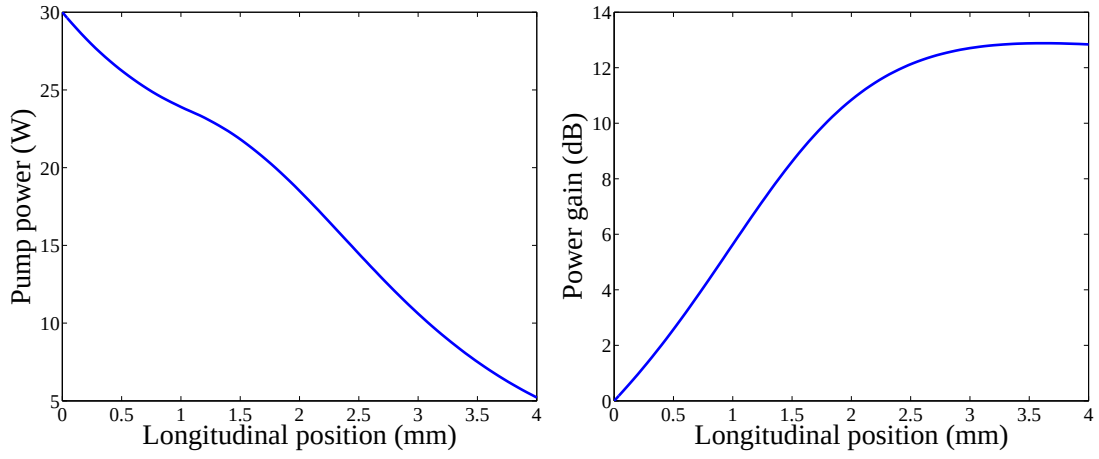

(a) (b)

Figure 4.6: Results from the CW simulation for an Yb:YAG crystal with $N = 9 \times 10^{26}$ m^{-3}. (a) Gradient of pump power absorption. (b) Evolution of power gain along optical axis.

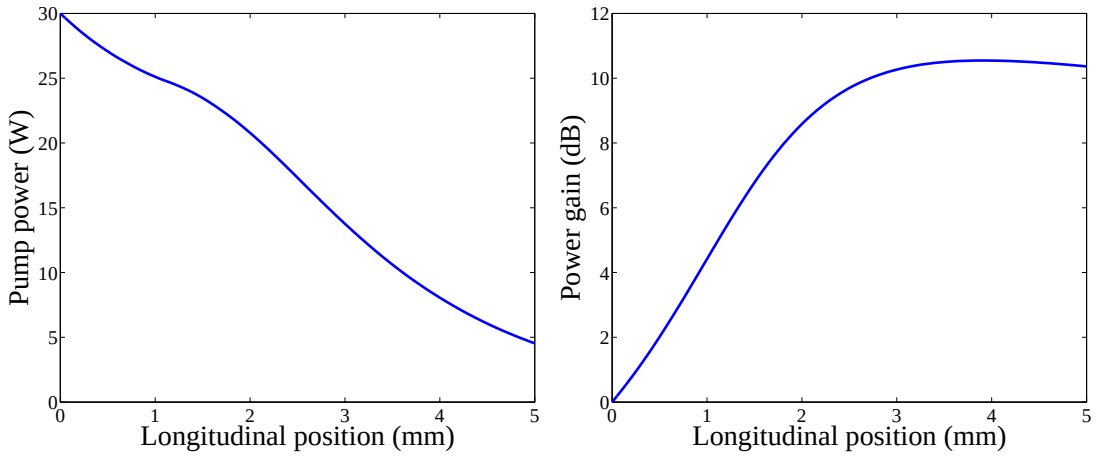

(a) (b)

Figure 4.7: Results from the CW simulation for an Yb:YAG crystal with $N = 7 \times 10^{26}$ m^{-3}. (a) Gradient of pump power absorption. (b) Evolution of power gain along optical axis.

4.1.4 Results from the time-dependent model

Using the dual-pass numerical model, the chosen crystal may now be evaluated in terms of pulse amplification. An input pulse with energy 200 nJ and FWHM of 30 ps is incident upon the Yb:YAG crystal. The pulse passes through the crystal and is reflected for a second pass. This process is again modeled on the assumptions described in Section 2.3.3.

The results are shown in Figures 4.8 and 4.9. The total energy gain of 21.61 dB gives an output power of 29 μJ. Although very little saturation of the upper state population occurs and the extraction efficiency of the amplifier is poor, the energy gain is maximized and any further amplification will require multiple (more than two) passes through the crystal.

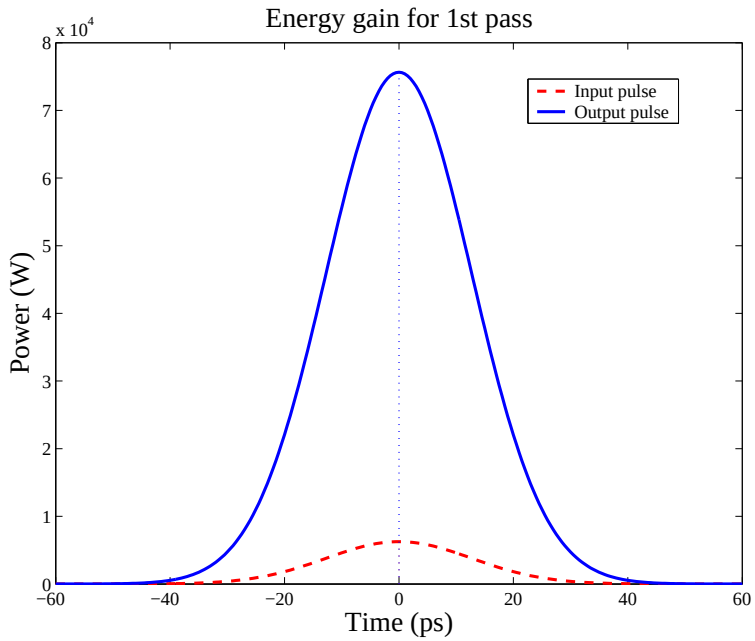

(a)

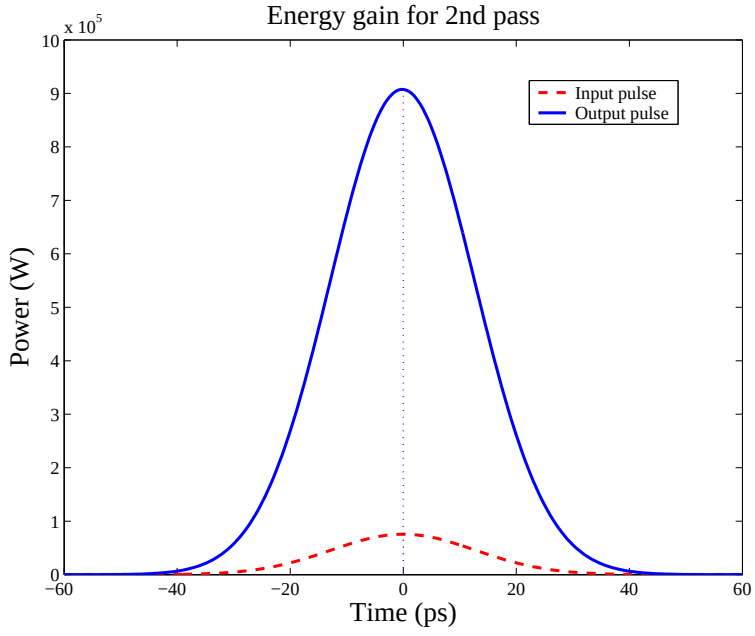

(b)

Figure 4.8: Results from the dual-pass numerical model for an Yb:YAG crystal with $N = 7 \times 10^{26}$ m^{-3}. (a) Energy gain for the first pass: 10.83 dB. (b) Energy gain for the second pass: 10.79 dB.

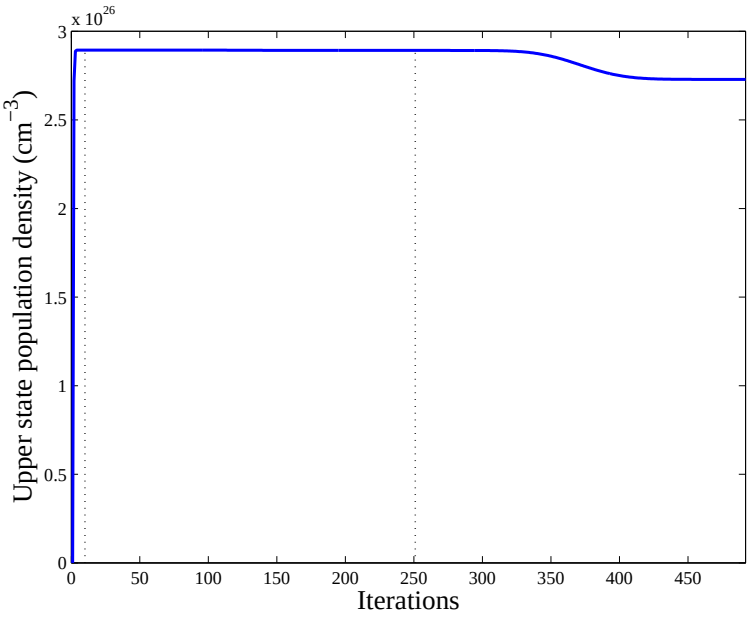

Figure 4.9: Result from the dual-pass numerical model for an Yb:YAG crystal with $N = 7 \times 10^{26}$ m^{-3}. The upper state population density as a function of iterations indicates almost no saturation during the first pass and only a slight amount of saturation as a result of the second pass.

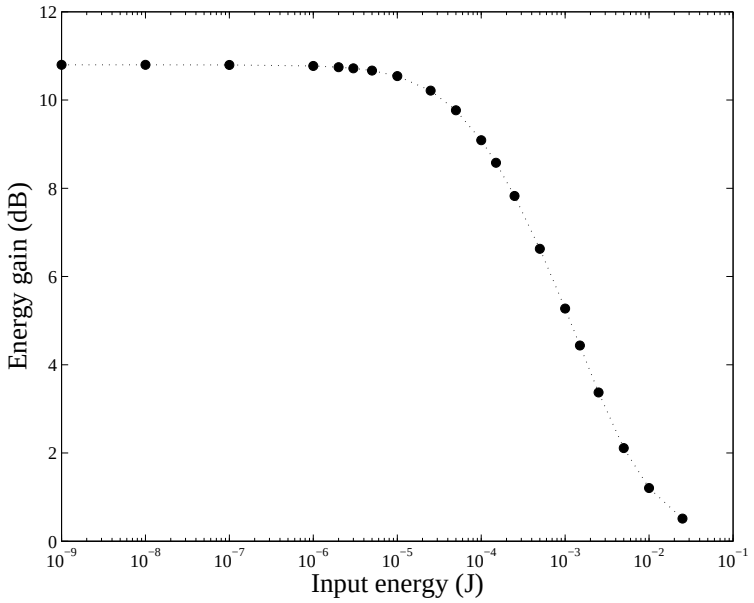

Figure 4.10: Saturation characteristic of the Yb:YAG crystal with $N = 7 \times 10^{26}$ m^{-3}, calculated with the time-dependent model. The theoretical saturation input energy is approximately 0.25 mJ.

Figure 4.10 shows the numerically calculated saturation characteristics of the Yb:YAG amplifier.

From this graph the saturation input energy of the amplifier can be estimated by making use of the 3 dB point [51]. According to the 3 dB definition the amplifier reaches its saturation input energy when the gain is 3 dB less than the maximum gain. The saturation input energy then follows as approximately 0.25 mJ for the crystal under consideration.

4.2 Thermal considerations

Yb:YAG has very good thermal properties relative to other popular laser materials such as Nd:YAG [50, 52, 53]. For the preceding simulations the pump beam was assumed to have a waist radius of roughly 100 μm within the crystal. Since such a small waist radius is usually associated with high intensities, thermal effects should be considered [54]. Although thermal effects are responsible for a variety of phenomena in laser media (thermo-optic aberrations, thermal lensing, stress-induced birefringence, etc.), only two specific consequences of thermal loading will be considered. Firstly, the temperature dependence of the gain that can be expected from the amplifier has to be investigated. The temperature dependence of not only the transition coefficients, but also the thermal properties of laser media is a topic that has been researched to great extent in recent years [55, 56] and is worth exploring, if only qualitatively. Secondly, despite the fact that the design criteria for the Yb:YAG amplifier requires acceptable thermal gradients along the optical axis, the possibility of thermally induced crystal fracture should be explored. Section 4.2 deals with the investigation of the above mentioned thermal effects and their consequences.

4.2.1 Solving the heat equation

In order to explore thermal effects due to diode end-pumping, it is first necessary to obtain the temperature distribution within the crystal. The crystal, with dimensions $4 \times 8 \times 5$ mm (height $\times$ width $\times$ length), is bound by a water-cooled mount (20°C) at the top and the bottom, whilst the sides are bound by air (25°C). The calculation for the temperature distribution may be simplified greatly by assuming that the heat generation along the length of the crystal is uniform (z independent). Since the heat extraction by the water-cooled mount may also be assumed to be uniform, the heat conduction in the z direction (along the optical axis) may be neglected. The heat flow is therefore restricted to a plane perpendicular to the z-axis (xy-plane) and a cross section of the crystal at any z position may be considered as if the surrounding cross sections did not exist [50, 51].

Although the assumption for uniform heat generation applies strictly to "long" rods subject to side-pumping [51], it can be justified for end-pumping geometries close to the front surface of the crystal. The front surface of the crystal is thermally isolated by air on the one side and in thermal contact with crystal medium on the other side. Assuming the pump light to be absorbed in a saturated manner, the crystal medium in contact with the front surface has a temperature that is approximately equal to that of the front surface, making it possible to neglect heat conduction between them.

As a result of absorption, the pump power incident on the crystal is a maximum at the front surface and is therefore of specific interest in the investigation to follow.

With respect to the possibility of thermal fracture, an investigation into the thermal effects on the front surface of the crystal is sufficient since the thermal fracture limit on the surface of the material is substantially lower than the thermal fracture limit within the bulk material [57]. Figure 4.11 gives a diagrammatic representation of the 30 W pump beam, with an axisymmetric top hat profile, incident on the crystal surface.

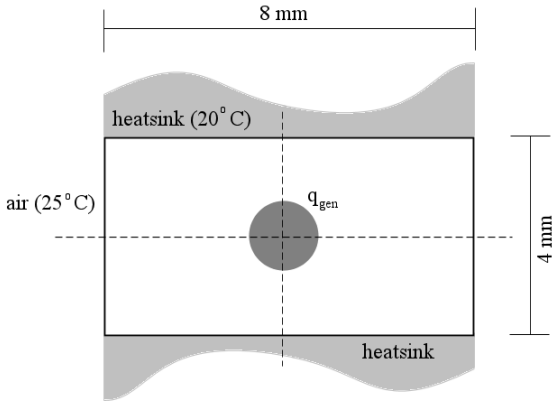

Figure 4.11: Graphical presentation of heat generation within an Yb:YAG crystal.

The temperature distribution may be obtained from the material properties and the properties of the thermal source (pump), by solving the two-dimensional heat equation for the front surface of the crystal [54, 58, 59, 53]. The heat equation for two dimensions may be written as follows:

$$\frac{\partial T}{\partial t} = \alpha \left[\frac{\partial^2 T}{\partial x^2} + \frac{\partial^2 T}{\partial y^2} \right] + \frac{\alpha}{k} q_{gen} \tag{4.2}$$

$T = T(t, x, y)$ denotes the temperature, t the time, x and y the spatial coordinates, α the coefficient of thermal expansion and k the thermal conductivity of the material. The parameter q_{gen} will be discussed at the end of this section. In the form of equation 4.2, the heat equation may be solved by making use of the so-called Forward-Time Centered-Space (FTCS) method [60]. According to the FTCS method, the heat equation may be rewritten as:

$$\begin{aligned} \frac{T(t+\Delta t, x, y) - T(t, x, y)}{\Delta t} = & \frac{\alpha}{\Delta^2} \{ [T(t, x+\Delta, y) - 2T(t, x, y) + \\ & T(t, x-\Delta, y)] + [T(t, x, y+\Delta) - \\ & 2T(t, x, y) + T(t, x, y-\Delta)] \} + \frac{\alpha}{k} q_{gen} \end{aligned} \tag{4.3}$$

For equation 4.3 the following transformations are made: $\partial t \rightarrow \Delta t$ and $\partial x, \partial y \rightarrow \Delta$.

The right-hand side of equation 4.3 simply states that the temperature at a certain position, specified by coordinates x and y, at time $t + \Delta t$ can be calculated from the temperatures of its nearest neighbors at time t. The logic of the FTCS method is illustrated in Figure 4.12. The FTCS method is stable in two dimensions when the Von Neumann stability condition is satisfied:

$$\frac{\alpha \Delta t}{\Delta^2} \leq \frac{1}{4} \tag{4.4}$$

Substituting the Von Neumann condition as an equality, the FTCS solution to the heat equation may be written in a simplified form, given by:

$$\begin{aligned} T(t+\Delta t, x, y) &= \frac{1}{4}\left[T(t, x+\Delta, y) + T(t, x-\Delta, y) + T(t, x, y+\Delta) + \right. \\ &\quad \left. T(t, x, y-\Delta)\right] + \frac{\Delta^2}{4k} q_{gen} \end{aligned} \tag{4.5}$$

The bracketed part on the right-hand side of equation 4.5 represents diffusion of heat, while the remaining term represents a heat generating process. Solving the heat equation therefore provides a steady-state temperature distribution on the front surface of the crystal by taking into account, the amount of heat that is generated, the way the heat is transported on the surface of the medium and the boundary conditions. For simplicity, the boundary conditions are assumed to be fixed. Fixed boundary conditions translate into the assumption of perfect thermal conduction between the crystal and the water-cooled mount (heatsink) and perfect thermal isolation between the crystal and the neighboring air (refer to Figure 4.11). Although both of the boundary condition assumptions may break down in realworld situations, the resulting conduction between the crystal and its surroundings should approximate the assumption well.

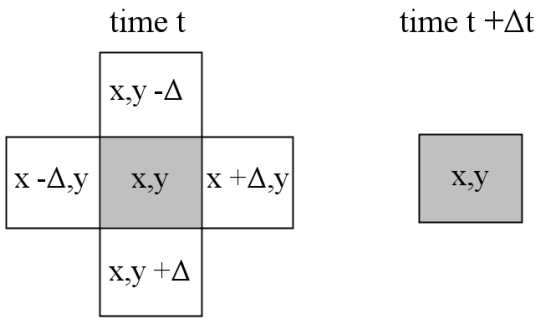

Figure 4.12: Graphical presentation of FTCS-method, used to solve the 2D heat equation.

The parameter labeled q_{gen} denotes the source of heat within the heat equation formalism. The pump source is responsible for the generated heat but only a fraction of the pump power is converted into thermal energy.

The main mechanism leading to the conversion of optical power (pump light) into thermal energy is the quantum defect [52]. The quantum defect quantifies the amount of energy that is transported through the medium by way of fast non-radiative transitions (see Section 2.1.1). In preceding discussions, mention was made of the fact that Yb:YAG has a small quantum defect in comparison to some other popular laser crystals (for example Nd:YAG) and it is exactly this characteristic that contributes greatly to Yb:YAG's outstanding thermal properties.

In general, q_{gen} may be defined as:

$$q_{gen} = -(1-\eta)\frac{\partial I_p}{\partial z} \tag{4.6}$$

$(1-\eta)$ denotes the quantum defect with $\eta = \lambda_p/\lambda_s$, while $\frac{\partial I_p}{\partial z}$ is a measure of the amount of pump power absorbed over a distance z and also contains information about the change in the cross sectional area (A) of the beam over z. As in equation 2.10, the derivative of the intensity with respect to z can be decomposed as follows:

$$\begin{aligned}\frac{dI}{dz} &= \frac{d}{dz}\left(\frac{P}{A}\right) \\ &= \frac{1}{A}\frac{dP}{dz} + P\frac{d}{dz}\left(\frac{1}{A}\right)\end{aligned} \tag{4.7}$$

The first term in equation 4.7 describes the heat generation process sufficiently and the second term (non-absorptive) may therefore be neglected. $\frac{\partial P_p}{\partial z}$ can now be calculated in two ways. The first method, labeled here as the unsaturated absorption method, is self explanatory. The pump power is assumed to be absorbed by the first infinitesimally small increment of the crystal (front surface) in an unsaturated environment. Under the assumption of unsaturated absorption of pump power, the output power after a given distance of propagation, as a result of a specific input power, is mathematically described by (refer to equation 3.19):

$$P^p(z) = P_0^p e^{-\sigma_{12}^p N z} \tag{4.8}$$

All the parameters in equation 4.8 have their usual meaning and P_0^p denotes the input pump power. For the case where $z \ll 1$, the exponential term approaches unity and the q_{gen} parameter is defined as:

$$q_{gen} = (1-\eta)\frac{\sigma_{12}^p N P_0^p}{A} \tag{4.9}$$

The second method by which $\frac{\partial P_p}{\partial z}$ can be calculated is labeled the saturated absorption method, since it is able to take account of possible saturation of the upper energy state with respect to absorption.

For the second method, the derivative is simply obtained from the CW numerical simulation and should be a fairly accurate representation of the actual absorbed power.

As an example of the obtained temperature distribution, Figure 4.13 is shown. The temperature distribution was obtained for the Yb:YAG crystal identified as the optimum design making use of the unsaturated absorption method for reasons that will be explained in Section 4.2.2. The pump beam (with $M_p^2 = 74$ and initial power of 30 W) is focused 2 mm beyond the front surface of the crystal, resulting in a spot radius of 266 μm on the front surface. The heat equation was solved using $\Delta = 20$ μm and $k = 14$ W m^{-1} K^{-1} (K denotes Kelvin) [44]. For Figure 4.13 the maximum temperature of 70.4°C is obtained at the position of the optical axis on the front surface.

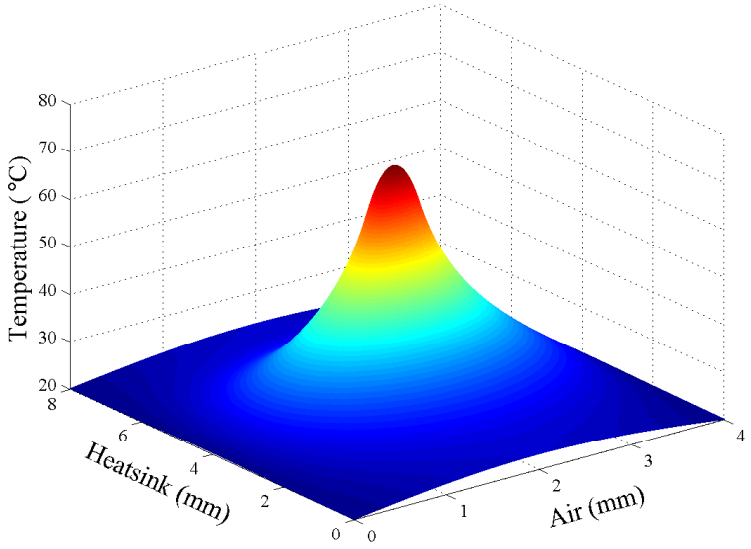

Figure 4.13: Temperature distribution on the front surface of the crystal. The pump beam is focused 2 mm into the crystal, resulting in a pump spot radius of 266 μm on the front surface. The maximum temperature of 70.4°C is located at the centre of the crystal.

4.2.2 Effect on gain

The temperature distribution for the optimum Yb:YAG crystal was also obtained using the saturated absorption method, yielding a similar profile and a maximum temperature of 52.4°C. It was however decided to use the temperature distribution of Section 4.2.1 (or at least the maximum temperature) to establish a worst-case scenario regarding the degree to which thermal effects influence the gain expected from the Yb:YAG amplifier. For the purpose of evaluating the influence of thermal effects on the gain, Boltzmann statistics is used [44].

It is assumed that the thermal properties of Yb:YAG remain constant over the temperature range of interest. The main area of concern is the possible changes in the absorption coefficients of the lower energy manifold of Yb:YAG that may arise due to changes in the temperature.

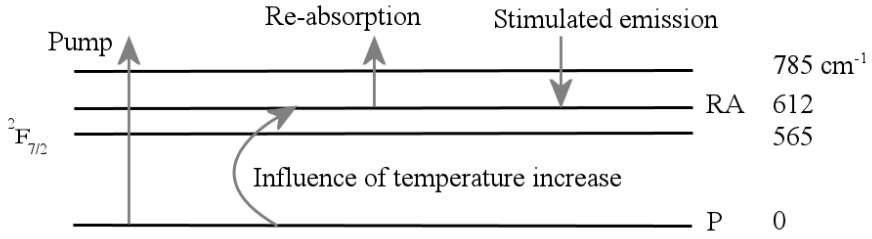

Figure 4.14: Magnified $^2F_{7/2}$ manifold of Yb:YAG. The process whereby an increase in temperature influences the level population densities are indicated. The energy level associated with re-absorption is labeled RA, while P denotes the lower pump level.

A magnified illustration of the $^2F_{7/2}$ manifold of Yb:YAG (refer to Figure 4.1) is shown in Figure 4.14. The energy level labeled P indicates the lower pump level, while the energy level from where re-absorption takes place is indicated by RA. The extent to which a temperature increase leads to a decrease in the population density of the lower pump level (N_P) and a corresponding increase in the population density of the re-absorption level (N_{RA}), may be described by the following Boltzmann equation:

$$N_{RA}\left(T_{new}\right) = N_{RA}\left(T_{old}\right)\exp\left[-\frac{\Delta E}{k_B}\left(\frac{1}{T_{new}}-\frac{1}{T_{old}}\right)\right] \tag{4.10}$$

T_{old} represents the temperature at a time prior to the heat generating process and T_{new} denotes the maximum temperature in the temperature distribution due to heating (optical pumping). The energy difference between levels RA and P are indicated by ΔE and must be converted from cm^{-1} to Joule. The constant k_B in equation 4.13 has a value of $1.38\times10^{-23}\ \mathrm{J\,K}^{-1}$ and is the well known Boltzmann constant.

Since the level population density is related to the absorption coefficient by the absorption cross section ($\alpha_{RA}=\sigma_{RA}N_{RA}$), equation 4.13 may be used to write:

$$\frac{\alpha_{RA}\left(T_{new}\right)}{\alpha_{RA}\left(T_{old}\right)} = \frac{\sigma_{RA}\left(T_{new}\right)}{\sigma_{RA}\left(T_{old}\right)}\exp\left[-\frac{\Delta E}{k_B}\left(\frac{1}{T_{new}}-\frac{1}{T_{old}}\right)\right] \tag{4.11}$$

Due to the temperature independence of the absorption cross section, the factor $\frac{\sigma_{RA}(T_{new})}{\sigma_{RA}(T_{old})}$ is simply unity. It is therefore possible to obtain the change in the absorption coefficient of level RA as a result of a known temperature increase. This increase in the absorption coefficient of level RA corresponds to a decrease in the absorption coefficient of the lower pump level (α_P). The increase and decrease of the absorption coefficients may be explained as follows. The temperature of an ensemble of atoms determines its energy distribution. As the temperature increases, more of the atoms have a higher energy and consequently, less atoms occupy in the ground state (P). Since the pumping process relies on atoms occupying the ground state, the absorption coefficient at the pump wavelength decreases.

It can be seen that the decrease of the pump wavelength absorption coefficient, together with the fact that more atoms occupy the lower lasing transition (RA), will lead to a decrease in the gain achievable with the amplifier.

The CW model may be used for a comparison between the gain achievable from an Yb:YAG crystal with absorption coefficients corresponding to T_{old} and the gain achievable from an Yb:YAG crystal with absorption coefficients corresponding to T_{new}. For this purpose it is necessary to revisit the procedure used to solve the model equations. The equations used to solve the CW model with transverse coordinates, as well as the time-dependent model, makes use of the cross sections (absorption and emission) to characterize the complete energy level structure of the gain medium. In the case of Yb:YAG, the quasi-three-level structure was reduced to a two-level structure by assuming that none of the ions accumulate in energy levels other than the lower pump level and the upper laser level. The numerical calculations, used to solve the model equations, used the cross section values to determine the way in which the population densities of the simplified two-level system responds to the pump and probe radiation fields. The population densities are therefore dependent on the values of the cross sections, which are specified as input parameters to the model. Since the model does not contain the absorption or emission coefficients and the values of the population densities are simply calculated from the cross sections, the gain's dependence on the absorption coefficients cannot be evaluated. The effect of changing absorption coefficients can however be modeled by approximating the absorption cross sections as temperature dependent and the population densities as temperature independent parameters:

$$\alpha\left(T\right)=\sigma N\left(T\right) \quad \Rightarrow \quad \alpha\left(T\right)=\sigma\left(T\right)N \tag{4.12}$$

The change in these effective absorption cross sections may then be calculated as follows for simulation purposes:

$$\sigma_{RA}\left(T_{new}\right) \quad = \quad \sigma_{RA}\left(T_{old}\right)\exp\left[-\frac{\Delta E}{k_B}\left(\frac{1}{T_{new}}-\frac{1}{T_{old}}\right)\right] \tag{4.13}$$

Using values of 300 K (27°C) and 343 K (70°C) for T_{old} and T_{new}, respectively, the effective reabsorption cross section (previously labeled σ_{12}^{s}) increases from 1.3×10^{-21} cm^2 to 1.88×10^{-21} cm^2. Similarly, the effective absorption cross section at the pump wavelength (previously labeled σ_{12}^{p}) decreases from 8.5×10^{-21} cm^2 to 7.92×10^{-21} cm^2. Comparing the value for the gain predicted by the CW simulation, using the "old" and newly acquired effective cross sections, it is found that the influence of the temperature increase only leads to a 0.7 dB decrease. It can therefore be concluded that thermal effects have a relatively small influence on the gain for the temperatures under consideration.

4.2.3 Theory of elasticity

Thermal effects are responsible for the build-up of stress in laser materials. Stress is associated with displacements within the material which may lead to fracture.

Typically in end-pumped geometries, the cooler outer part of the crystal prevents the expansion of the hotter central part [59]. The unsaturated absorption temperature distribution is used to evaluate whether the thermal stresses are indeed capable of causing fracture of the crystal. This time however, the case where the pump beam (with the same waist radius and M_p^2) is focused on the front surface of the crystal, is explored. Again the temperature distribution looks similar to that of Figure 4.13 with a maximum of 88.2°C. For a certain temperature distribution, the corresponding stress tensor components on the front surface of the crystal can be calculated. For the calculation of the stress tensor components, the approach of Timoshenko and Goodier [61] shall be followed (also see [62]).

Since the approach of Timoshenko and Goodier is applicable to a long circular cylinder with a symmetrical temperature profile about the optical axis, the rectangular Yb:YAG crystal is approximated as cylindrical. Treatment of the crystal as a long cylinder provides the platform for the Plane Strain approximation, which assumes the front surface of the crystal to be subject to strains parallel to the surface only (also see [57]). Additionally, the forces acting on the long cylinder is assumed to be uniform along the cylinder's length, as was the case for the heat conduction in the temperature calculations of Section 4.2.1. The Plane Strain approximation therefore effectively assumes the crystal to have no displacement in the axial direction (polar coordinates).

The stresses (σ), strains (ϵ) and temperature (T) inside the crystal are related by Hooke's law as follows:

$$\epsilon_r - \alpha T = \frac{1}{E}\left[\sigma_r - \nu\left(\sigma_\theta + \sigma_z\right)\right] \tag{4.14}$$

$$\epsilon_\theta - \alpha T = \frac{1}{E}\left[\sigma_\theta - \nu\left(\sigma_r + \sigma_z\right)\right] \tag{4.15}$$

$$\epsilon_z - \alpha T = \frac{1}{E}\left[\sigma_z - \nu\left(\sigma_r + \sigma_\theta\right)\right] \tag{4.16}$$

α is again the thermal expansion coefficient, but the meaning of the other symbols are unique to this specific context. E denotes Young's modulus (Modulus of elasticity), ν the Poisson ratio, and the subscripts r, θ and z for the stress and strain symbols refer to the radial, tangential and axial components respectively. The assumption of no axial displacement ($w = 0$) however requires the axial strain to be zero, according to the relation:

$$\epsilon_z = \frac{\partial w}{\partial z} \tag{4.17}$$

As a result of equation 4.17, equations 4.14 to 4.16 may be rewritten as equations for the stress components in terms of the temperature and the radial and tangential strains.

Substitution of the stress equations into the equation of equilibrium,

$$\frac{d\sigma_r}{dr} + \frac{\sigma_r + \sigma_\theta}{r} = 0 \tag{4.18}$$

together with with the equations relating the strains and displacements,

$$\epsilon_r = \frac{du}{dr} \tag{4.19}$$

$$\epsilon_\theta = \frac{u}{r} \tag{4.20}$$

provides a differential equation for the radial displacement (u). The solution to the differential equation for the radial displacement is given by:

$$u = \frac{1+\nu}{1-\nu}\alpha\frac{1}{r}\int_a^r T(r)\, r\, dr + C_1 r + \frac{C_2}{r} \tag{4.21}$$

The constants of integration, C_1 and C_2, may be solved from the boundary conditions, while the integration boundary, a, has a value of zero for a solid cylinder.

Equation 4.21 may be substituted into the stress equations derived from equations 4.14 to 4.16, using the relations of equations 4.19 and 4.20. The boundary conditions require $(\sigma_r)_{r=b} = 0$, where b denotes the outermost radial coordinate, thereby giving solutions to the constants of integration. The stress tensor components along the radial and tangential directions follows as:

$$\sigma_r = \frac{\alpha E}{1-\nu}\left(\frac{1}{b^2}\int_0^b T(r)\, r\, dr - \frac{1}{r^2}\int_0^r T(r)\, r\, dr\right) \tag{4.22}$$

$$\sigma_\theta = \frac{\alpha E}{1-\nu}\left(\frac{1}{b^2}\int_0^b T(r)\, r\, dr + \frac{1}{r^2}\int_0^r T(r)\, r\, dr - T(r)\right) \tag{4.23}$$

Assuming zero axial force, the axial stress tensor component is similarly given by:

$$\sigma_z = \frac{\alpha E}{1-\nu}\left(\frac{2}{b^2}\int_0^b T(r)\, r\, dr - T(r)\right) \tag{4.24}$$

The zero axial force assumption is justified since the crystal is only mounted on the top and the bottom and no force is applied in the direction parallel to the optical axis.

For the rectangular Yb:YAG crystal, b in equations 4.22, 4.23 and 4.24 was chosen to have a value of 2 mm, thereby corresponding to the shortest dimension of the crystal face.

Another important addition to the theory, used to investigate the thermal stresses on the surface of the crystal, is that of the surface fracture strength. The fracture strength can be calculated from the following relation [57],

$$\sigma_f = \frac{K_c}{(\pi\beta)^{1/2}} \tag{4.25}$$

where β is the surface crack depth and K_c is the material fracture toughness [63]. The constant β in equation 4.25 is comparable to the dig number specified by laser material manufacturers and the value that is used for β in Section 4.2.4 is deduced from it.

4.2.4 Possibility of thermal fracture

The calculated individual stress components are shown in Figure 4.15 [51]. It is found that the crystal experiences a high degree of negative stress in the centre, whilst the edges are subject to a lesser degree of positive stress. Positive stress corresponds to tension and negative stress is associated with compression [57, 64]. The values used for the various parameters are given in Table 4.3 [65].

Symbol	Value	Unit
α	8.2×10^{-6}	K^{-1}
E	310×10^{9}	$\mathrm{kg\,m^{-1}\,s^{-2}}$
ν	0.3	-
K_c	2.2×10^{6}	$\mathrm{kg\,m^{-1/2}\,s^{-2}}$
β	50×10^{-6}	m

Table 4.3: Parameters used for the calculation of the thermal stress tensor components on the surface of an Yb:YAG crystal.

Figure 4.16 gives the resultant stress, normalized to the surface fracture strength of the crystal, as a function of radial coordinates. The resultant stress was calculated according to:

$$\sigma_{res} = \sqrt{\sigma_r^2 + \sigma_\theta^2 + \sigma_z^2} \tag{4.26}$$

Equation 4.26 is a generalization of the total edge stress, defined by Koechner [51]. Referring to the dashed line in Figure 4.16, indicating the fracture limit, it is evident that the calculations predict crystal fracture due to compression. The pump beam focused on the front surface of the crystal with a waist radius of 100 μm corresponds to an intensity of 95 $\mathrm{kW\,cm^{-2}}$. Upon consulting the supplier of the Yb:YAG crystal, used for the experiment to follow in Section 4.3, the result of likely crystal fracture was verified. It can therefore be concluded that the waist size of the pump beam should be enlarged to avoid crystal fracture. An enlarged pump waist will however lead to a slight decrease in the gain that can be expected from the amplifier.

The temperature distribution and the relative magnitude of the stress components were also investigated with the commercial software LASCAD (Appendix). LASCAD yielded results in good agreement with the calculations performed in Sections 4.2.1 and 4.2.4.

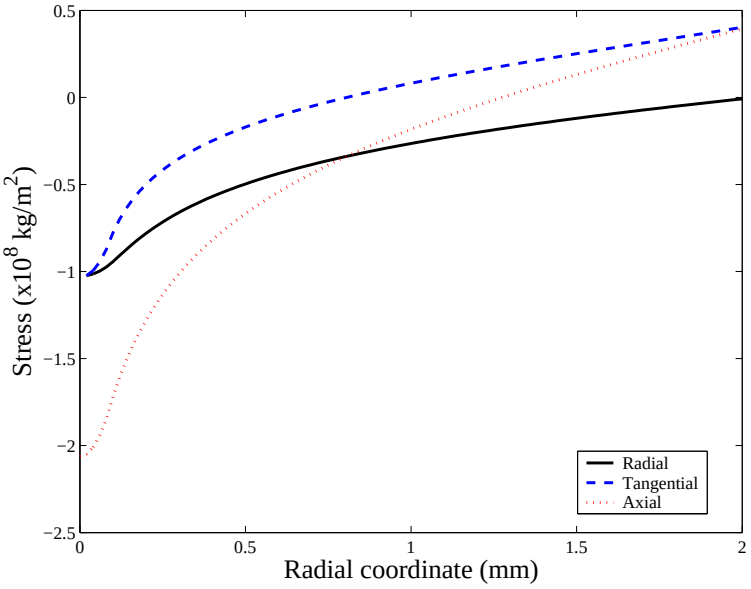

(a)

Figure 4.15: Stress components at radial positions across the shortest dimension of the crystal. The crystal is subject to extreme compressive stresses.

4.3 Experimental setup

The original plan for the Yb:YAG experiment was to perform an analysis similar to that of the Nd:YVO_4 experiment. The approach used in Chapter 3 was to characterize the system for the purpose of optimizing the gain, after which the dependence of the gain on the input pump and input probe power was investigated. The approach of Chapter 3 however requires the experiment to be equipped with an appropriate pump and probe source. Although a pump source for Yb:YAG is conveniently provided in the form of InGaAs diodes, the probe source requires some initiative. In the introduction to this thesis it was stated that an Yb:glass fibre laser will serve as a probe source. Unfortunately this laser has an output spectrum centered about 1080 nm and therefore needs to be tuned to obtain the required spectral properties corresponding to Yb:YAG. Due to a lack of human resources and time the fibre laser was not available for this experiment and another approach was necessary for the investigation of the Yb:YAG medium.

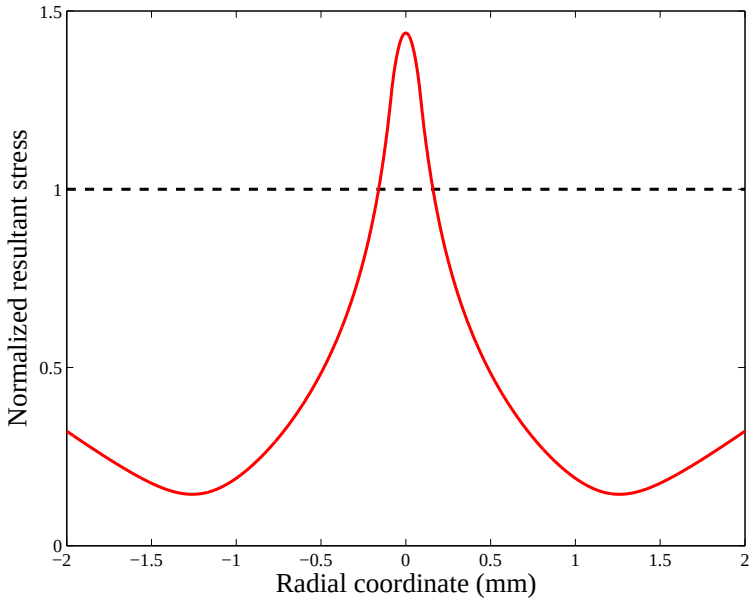

(a)

Figure 4.16: Resultant stress value, normalized to the surface fracture strength of the crystal, as a function of radial position.

The details of the new approach will be discussed in Section 4.4, while Section 4.3 is concerned with the design and characterization of the experimental setup.

4.3.1 Optical design for pump beam

The details of the pump source to be used in the Yb:YAG experiment have already been discussed. Although the diode module has an M_p^2 roughly half that of the diode module used in the Nd:YVO_4 experiment, the nature of the beam quality is such that a detailed optical design is required. Since the preceding discussion regarding thermal effects led to the conclusion that a pump waist radius of 100 μm will quite possibly result in fracture, it was decided to use a waist radius of 150 μm for the pump beam. A number of high quality optical elements, such as aspherical lenses and achromatic doublets, with the appropriate anti-reflective coatings were available for the construction of the pump beam propagation path. Apart from using Gaussian beam optics, the design process was also approached from a geometrical optics viewpoint. The use of geometrical optics was motivated by the fact that optical aberrations, specifically spherical aberrations, influenced the spot size and beam quality of the pump beam in the Nd:YVO_4 experiment.

With regards to geometrical optics, two tools were used to evaluate a large number of different optical systems. A student edition of the commercial software OSLO LT (Appendix) was used to evaluate the spot diagrams and wavefront aberrations in the image plane of the various systems. A spot diagram reveals information about the type of aberrations that influence an optical system and also gives an idea of the intensity spread in the image plane due to an on-axis object point.

In a similar way the wavefront peak-to-valley value is used to evaluate the quality of an optical system. Making use of the aberration polynomial coefficients, calculated by OSLO, the relative magnitude of the respective aberrations can be quantified. The second tool used in the design process is a ray tracing program written in MATLAB (Appendix). The ray tracing tool, also capable of calculating the wavefront and its departure from a perfect spherical wavefront, was used to assess whether the predictions given by OSLO are sensible.

Figure 4.17 shows the optimum design for the purpose of imaging the fibre end face with a lateral magnification of -1.5. The design consist of a large numerical aperture aspherical element with a focal length of 11 mm, used to decrease the divergence of the pump light, as well as two doublets with focal lengths of 200 mm and 150 mm respectively. The aspherical element was found to reduce the primary spherical aberrations within the system by a factor of 2.5 (in comparison to similar designs), whilst the combination of the doublets minimized the angles of incidence of the rays with respect to the refracting surfaces, thereby leading to better image quality. The system of Figure 4.17 gave a spot diagram with a Root-Mean-Square (RMS) radius of 7 μm, compared to the diffraction limit of 3.8 μm. The wavefront had a peak-to-valley value of less than one wavelength (at 940 nm), which is very good considering the amount of elements used as well as the large aperture of the system [66].

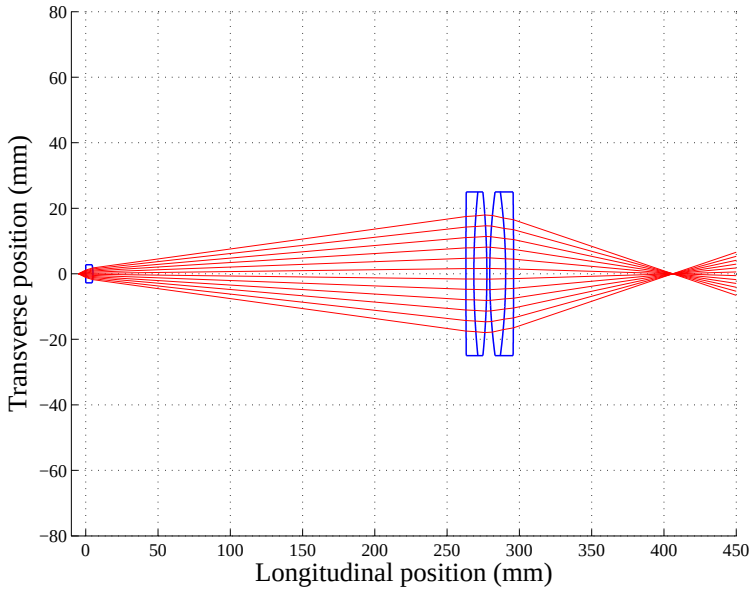

Figure 4.17: Design of pump beam propagation path obtained from geometrical ray tracing.

4.3.2 Characterization

A preliminary experimental setup containing the relevant dimensions and optical elements is shown in Figure 4.18. Except for a change in the distances between the elements, this setup is based on the ray tracing design. The pump diodes are cooled by a thermo-electric cooling device (TE technology, Inc.).

The thermo-electric cooling device is optimized for rapid convergence to the set temperature within the range of 20°C to 30°C and enables excellent tunability of the diode temperature. The pump beam is transmitted through an aspherical lens (L) and two achromatic doublets (AR 940 nm) before being focused in the centre of the water-cooled Yb:YAG crystal (maintained at 20°C). The crystal used for all the experimental data to follow was provided by Castech and has a dopant concentration of 5 at.% and dimensions previously specified. Again, translation stages (TS) were used for efficient alignment of the optical elements.

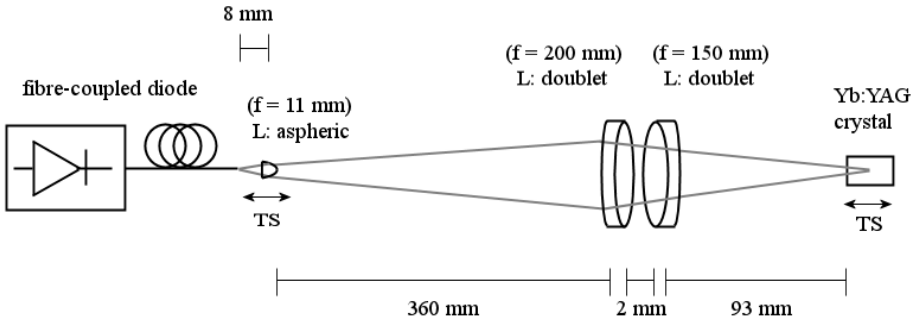

Figure 4.18: Preliminary experimental setup with Yb:YAG as amplifying medium.

The electro-optical properties of the pump source are given in Figure 4.19. The maximum output power is 26.8 W. The central wavelength of the pump radiation is highly dependent on the output power as well as the temperature of the diode module as shown in Figure 4.20.

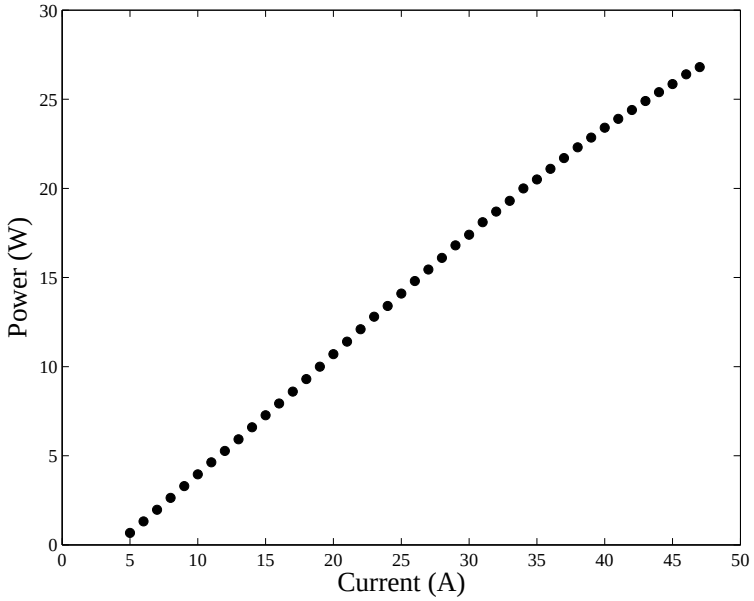

Figure 4.19: Electro-optical properties of pump diodes at 24°C.

The wavelength ranges from 934 nm to 943 nm. Since the largest absorption cross section corresponds to a wavelength of 941 nm, it makes sense to operate the module at a temperature of either 22°C and 25.9 W or 24°C and 23.4 W.

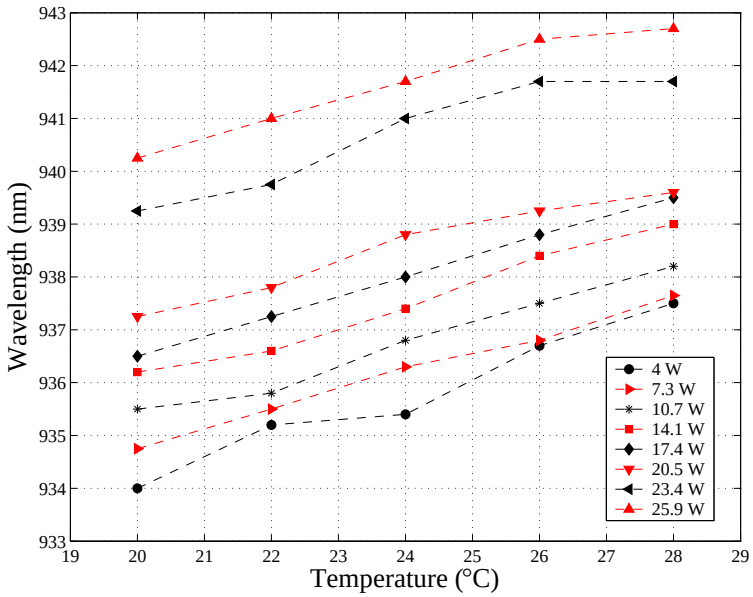

Figure 4.20: Diode wavelength dependence on pump power and temperature.

As in the Nd:YVO_4 experiment, the pump beam was evaluated using a CCD camera. The optical setup was changed slightly for the purpose of obtaining a measured result for the M_p^2 value without saturating the CCD. Although a graph of the processed data is not shown here, the value of $M_p^2 = 70$ is in excellent agreement with the theoretical value. An attempt to reproduce the measured result for the M_p^2, using the actual optical setup (Figure 4.18) including neutral density filters, resulted in an $M_p^2 = 84$ which is 14% larger than the specified value. This measurement yielded a waist radius for the pump beam of 151 μm which is close to the expected value.

4.4 Results and discussion

Due to the absence of a probe source, the focus of the experiment shifted. Since the gain could no longer be measured and compared to results obtained from the numerical models, a new method of evaluation was required. In order to extract information from the experiment, it was decided to attempt an investigation into the crystal's spontaneous emission. For this purpose a CCD camera and a spectrometer were used. Additionally, information about the relative absorption can be extracted and compared to the numerical results by analyzing the transmission of pump light through the crystal. Section 4.4 is concerned with the procedures followed to obtain the results from the Yb:YAG experiment and concludes by showing a comparison between these results and those predicted by the simulations.

4.4.1 Final experimental setup

The experimental setup for the investigation of spontaneous emission is given in Figure 4.21. For simplicity, the part of the setup to the left of the achromatic doublet has been omitted (refer to Figure 4.18). The pump power, focused in the centre of the crystal, is absorbed and results in fluorescence. This fluorescence takes place in all directions about the centre of the crystal with equal probability and may therefore be imaged onto a CCD camera equipped with a macro-lens and placed at a 90° angle with respect to the side of the crystal (a similar approach was followed by Chénais et al. in their investigation of absorption saturation [50]). To avoid any potential obstructions, a new water-cooled crystal mount was designed for the purpose of imaging the spontaneous emission.

Behind the rear surface of the crystal a convex lens (L) with a focal length of 75 mm is used to focus the diverging pump light as well as the contributions from spontaneous emission and ASE. The focused light then propagates onto a system of dichroic mirrors (M), of which the first two are coated to reflect light in the spectral region of 1040 nm and transmit light in the region of 940 nm, thereby removing traces of pump light that leads to saturation of the spectrometer. The third dichroic mirror is coated to transmit light of 1040 nm and ensures that only spontaneous emission and ASE reaches the spectrometer.

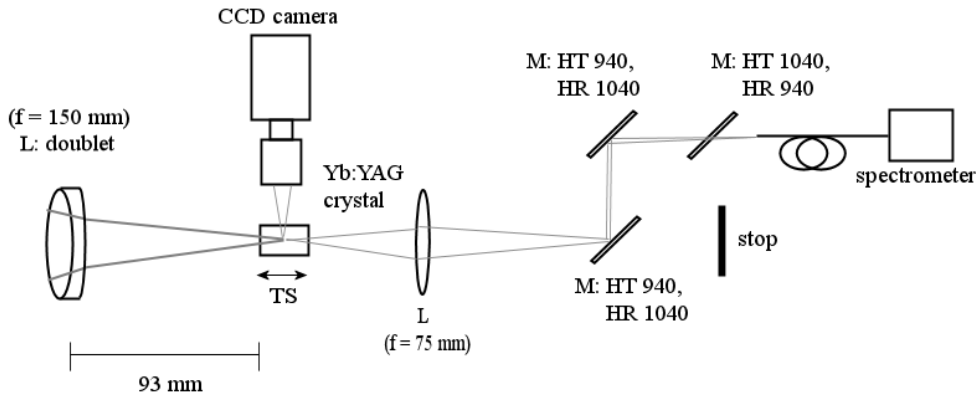

Figure 4.21: Final experimental setup used to investigate the properties of the spontaneous emission from a 5 at.% Yb:YAG amplifying medium.

Although the spontaneous emission from the side of the crystal, captured by the camera, is expected to have a wavelength of approximately 1030 nm, it was surprising to find elements of blue and green fluorescence intense enough to see with the naked eye. Using the spectrometer, it was however found that the intensity of these spectral components are in fact negligible in comparison to the infrared components. The reason for the blue and green fluorescence is the presence of rare earth impurities (such as Tm^{3+} and Er^{3+}) inside the Yb:YAG crystal, leading to anti-Stokes luminescence (upconversion) [67].

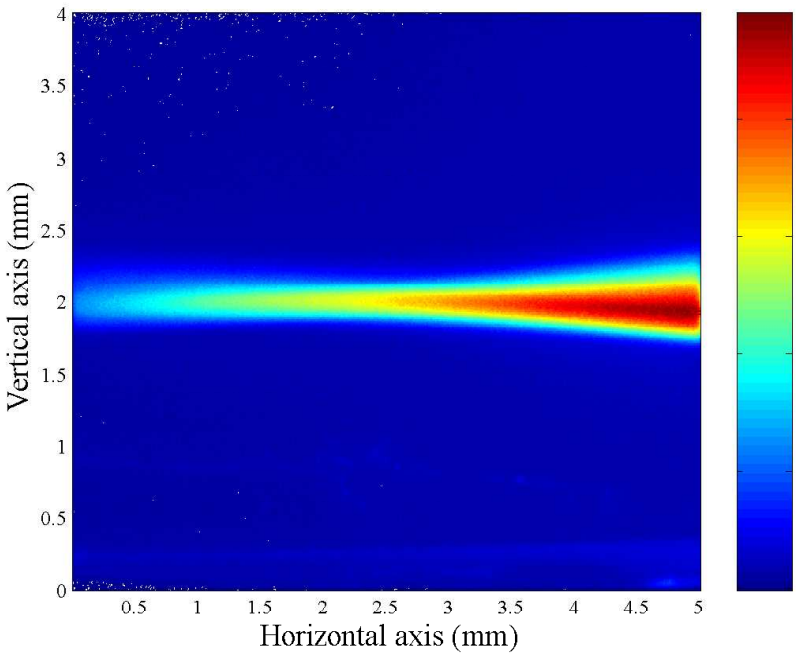

Figure 4.22: Spontaneous emission image obtained from a CCD camera at a 90° angle with respect to the side of the Yb:YAG crystal. The pump beam is focused in the centre of the crystal at full power.

As an example of the spontaneous emission profile that can be obtained with the camera from the side of the crystal, consider Figure 4.22. For this figure and for the rest of Chapter 4, it shall be assumed that light enters the crystal from the right-hand side. The camera had to be calibrated for a specific zoom level and distance from the object for the purpose of converting pixels into measurable units. The calibration process was simplified substantially due to the refraction of background light caused by the crystal and the fact that the crystal's dimensions are known. Once the camera had been calibrated, background noise was removed from the image in a similar manner to that used in Chapter 3 for the measurement of the pump beam's M_p^2. The specific example of Figure 4.22 shows the pump beam focused in the centre of the crystal, with the resulting profile due to beam propagation effects as well as absorption, decreasing the intensity that reaches the camera. As with the three-dimensional graphs of Chapter 2, the colour corresponding to some position resembles the third dimension (intensity), with red being the maximum and blue the minimum.

Despite the high M_p^2 of the pump beam and the fact that it is modeled as a top hat distribution in the simulation, the space-dependent intensity profile inside the crystal resembles a Gaussian intensity profile. The Gaussian intensity profile should be visualized as a three-dimensional distribution on a plane perpendicular to the optical axis, where the transverse x and y directions form a two-dimensional plane and the intensity at any given pair of coordinates forms the third dimension.

Assume the horizontal axis and the vertical axis of Figure 4.22 represent the z- and y-coordinates of the crystal respectively, with the x-coordinate perpendicular to the plane of the figure. The spontaneous emission profile of Figure 4.22 then consists of contributions from all the x-coordinates and for a given z-coordinate the intensity at each y-coordinates is simply an integral over a three-dimensional Gaussian intensity profile with respect to the x-coordinate. By performing the integral for a certain z-coordinate, the resulting two-dimensional profile, consisting of one spatial dimension (y) and one dimension representing the intensity, is in fact also Gaussian. More specifically, irrespective of the difference in magnitude, it is found that this two-dimensional intensity distribution has a spot radius equal to that of the original three-dimensional intensity distribution. Although the conclusion of identical spot sizes might seem straight forward, it is not a property common to all distributions and is of great practical value for the problem at hand. It is now possible to fit the intensity distribution of Figure 4.22 at every position along the optical axis with a Gaussian profile, thereby extracting the actual spot radii.

A comparison between the Gaussian beam, with an M_p^2 equal to that of the pump beam, and the spot radii extracted from the processed photograph is shown in Figure 4.23. Due to the low intensities at the end of the crystal (left-hand side of photograph) it is very difficult to extract sensible spot radii and those data points are therefore omitted. The waist of approximately 180 μm is larger than the waist that was designed and the waist measured during the M_p^2 beam scan. The larger size of the experimentally measured waist may be a result of the fact that the photograph was obtained with the pump at full power, whilst the beam scan was done at a very low pump power.

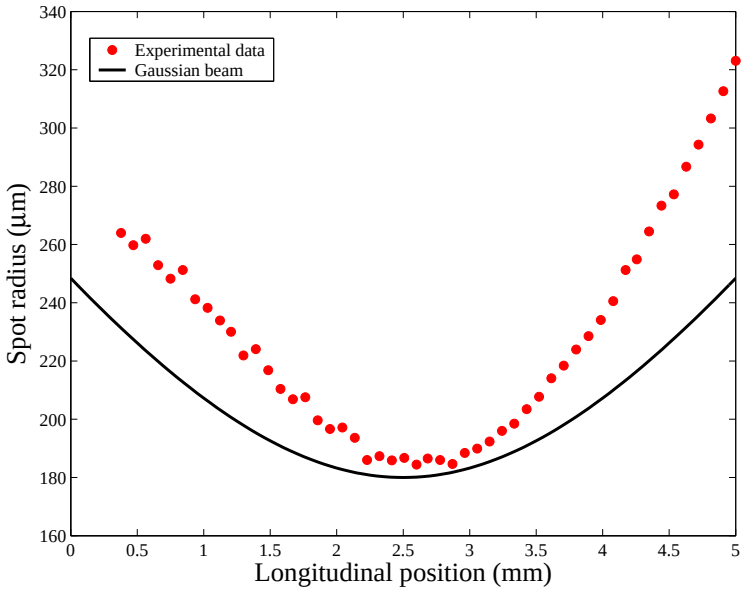

Figure 4.23: Spot radii along the optical axis according to the experimental data as well as Gaussian beam optics. The pump beam is focused in the centre of the crystal at full power.

4.4.2 Discussion

The argument used to derive the spot sizes of the pump beam from Figure 4.22 can also be used to evaluate the absorptive properties of the crystal. The absorption of pump radiation is responsible for the population inversion that leads to spontaneous emission. Therefore, if the three-dimensional pump intensity distribution inside the crystal is known, it may be related to the two-dimensional spontaneous emission intensity (I_{SE}), captured by the camera.

The Gaussian pump intensity distribution inside the crystal may be described as

$$I_p(x,y,z) = I_p(z)\, e^{-2\left(x^2+y^2\right)/w^2(z)} \tag{4.27}$$

where $I_p(z)$ denotes the pump intensity at all positions on the optical axis ($x = y = 0$). Assuming that this pump distribution leads to a similar population inversion distribution, which in turn is responsible for the intensity distribution of the spontaneous emission, it follows:

$$\begin{aligned} I_{SE}(y,z) &\propto \int_{-\infty}^{\infty} I_p(x,y,z)\, dx \\ &\propto I_p(z) \sqrt{\frac{\pi}{2}} w(z)\, e^{-2y^2/w^2(z)} \end{aligned} \tag{4.28}$$

The integration variable of equation 4.28 corresponds to the coordinate system that was defined in section 4.4.1. Especially of interest is the case for which $y = 0$ in equation 4.28 and only the intensities on the optical axis of Figure 4.22 are considered. Equation 4.28 may then be rewritten as:

$$I_{SE}(z) \propto I_p(z)\, w(z) \tag{4.29}$$

Section 4.4.1 describes a procedure whereby the spot radii is extracted from the photograph by fitting a Gaussian to the transverse intensity distributions. By also taking the maximum of this Gaussian fit at all positions along the optical axis, values for $w(z)$ and $I_{SE}(z)$ are provided. Since the pump intensity at all longitudinal positions can also be calculated by the CW model, equation 4.29 provides the platform for a qualitative comparison between the model and the experiment.

For comparative purposes, the spontaneous emission intensities obtained from the CCD camera are divided by the spot radii and the resulting intensities are normalized to the maximum intensity. Figures 4.24 and 4.25 give the experimental intensities and numerically calculated pump intensities (also normalized to the maximum pump intensity) for three different input pump powers respectively.

The pump beam is focused 3.7 mm beyond the front surface of the crystal (light enters the crystal from the right-hand side). Despite the fact that the experimental results at the start of the crystal are quite different from the numerical results with respect to the magnitude and order of the three curves, the residual pump power at the end of the crystal as well as the actual position of maximum pump intensity (2 mm from the end of the crystal) compares well. Figures 4.26 and 4.27 show the same graphs for the case of the pump beam focused in the centre of the crystal. The comparison between the experimental and numerical results are much better with the possible exception of the experimental result for an input pump power of 3.96 W.

In addition to the two sets of comparative results, shown in Figures 4.24 to 4.27, Figure 4.28 shows the experimental and numerical results (plotted on the same axis) for a full power pump beam focused in the centre of the crystal.

The result seems to indicate that our treatment of the spontaneous emission intensity is correct. It is however, important to comprehend the value of the comparisons made in Figures 4.24 to 4.28. Since the CW numerical model developed in Chapter 2 does not incorporate transverse coordinates for the pump beam, the simulation is unable to predict the absolute magnitude of the spontaneous emission at the various longitudinal positions. Furthermore, the method of evaluation for the experimentally measured spontaneous emission is also restricted to relative values and cannot be used to obtain absolute magnitudes. The normalized results are therefore acceptable and the importance of the comparison lies in the shape of the various curves (including the residual pump power).

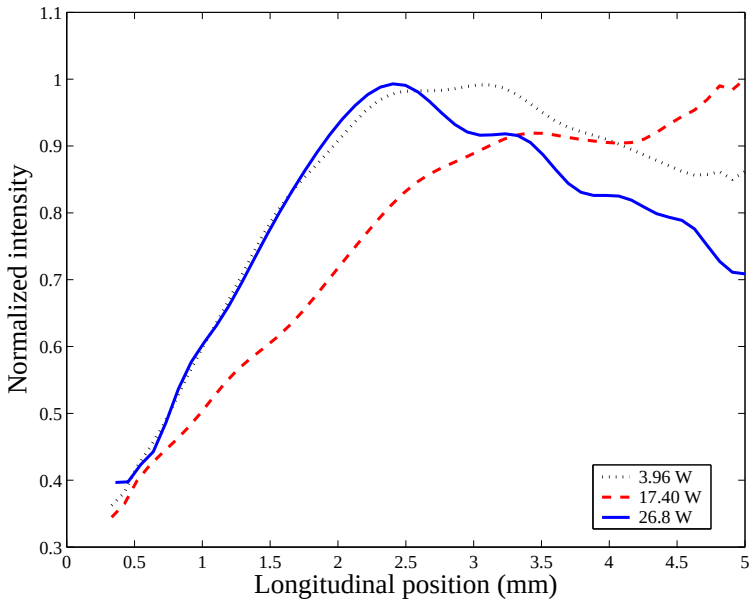

Figure 4.24: Normalized experimental result for intensity along the optical axis. The intensity is proportional to the pump intensity within the crystal at the corresponding z position. The pump beam is focused at a longitudinal position of 1.3 mm.

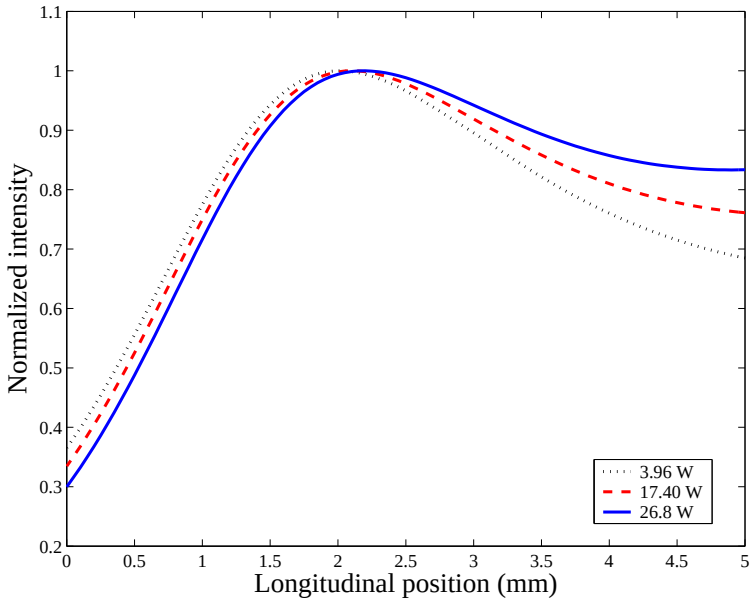

Figure 4.25: Numerical result for normalized pump intensity along the optical axis. The pump beam is focused at a longitudinal position of 1.3 mm.

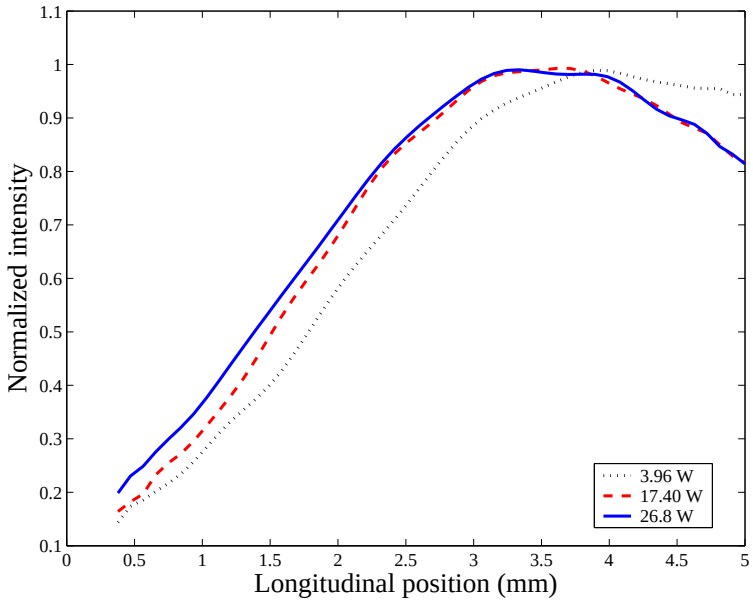

Figure 4.26: Normalized experimental result for intensity along the optical axis. The intensity is proportional to the pump intensity within the crystal at the corresponding z position.The pump beam is focused in the centre of the crystal.

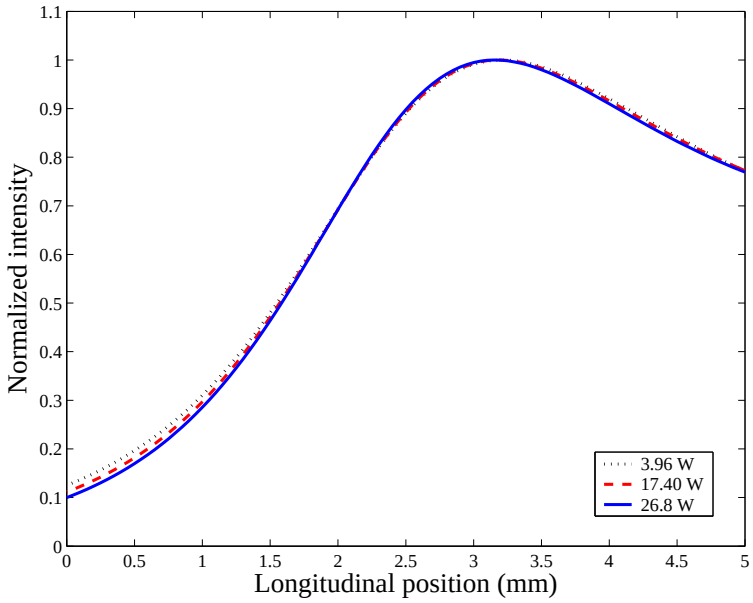

Figure 4.27: Numerical result for normalized pump intensity along the optical axis. The pump beam is focused in the centre of the crystal.

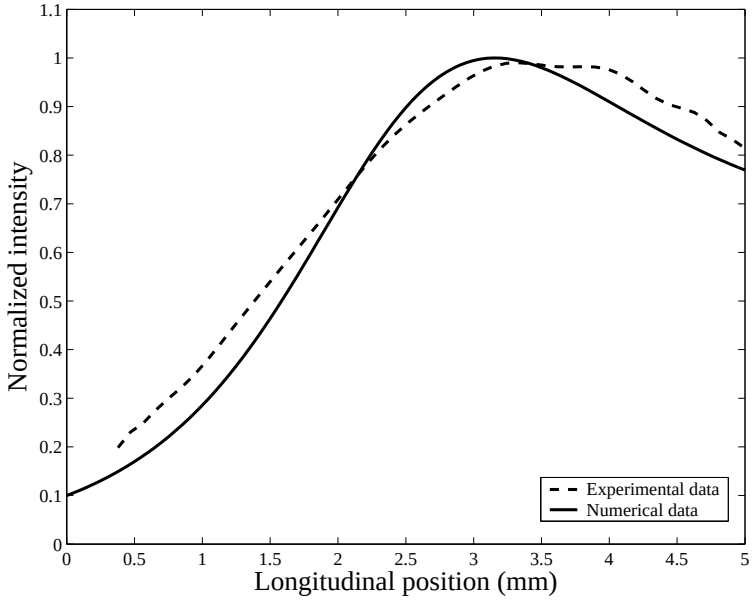

Figure 4.28: Comparison between the normalized pump intensity obtained from the simulation and the normalized experimentally measured intensity. The full power pump beam is focused in the centre of the crystal.

The spectrometer and sequence of mirrors, shown in the final experimental setup (Figure 4.21), are used to remove all traces of residual pump power and to measure the relative intensities of the spontaneous emission or possible ASE as the pump power is increased.

For the purpose of measuring the relative ASE or spontaneous emission intensities, it is important to first evaluate the spontaneous emission intensity at full pump power to ensure that the spectrometer does not saturate. A non-saturating spectrometer then indicates that the device can be kept stationary for all the measurements and establishes an absolute frame of reference. Apart from taking these measurements behind the crystal, the experiment is also performed at the side of the crystal, making use of a similar technique to remove possible pump light reflections.

The results for the measurements performed behind the crystal and those performed at the side of the crystal are given in Figures 4.29 and 4.30. Although it was stated at the start of this chapter that ASE has a negligible effect on the gain achievable with this specific Yb:YAG amplifier, the experimental results in Figure 4.29 are compared to those predicted by the simulation with ASE incorporated.

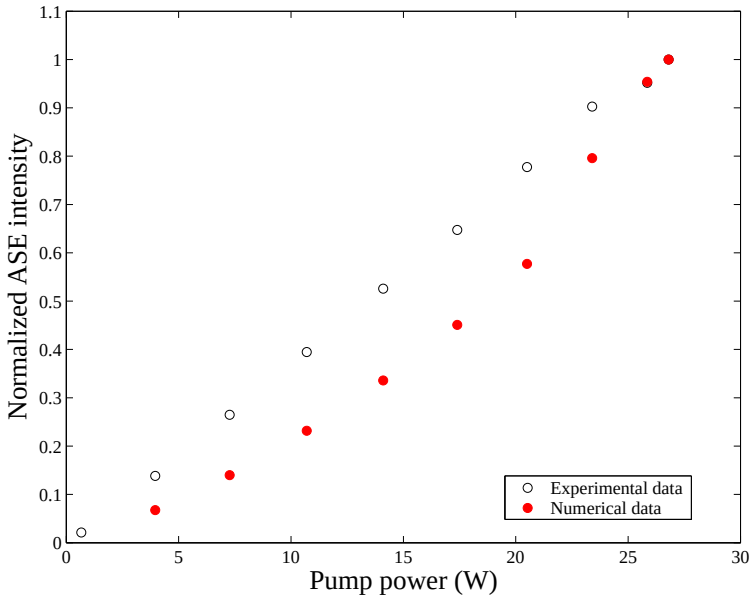

Figure 4.29: Comparison between the Experimental and Numerical results for the normalized ASE intensities. The measurement is performed behind the crystal.

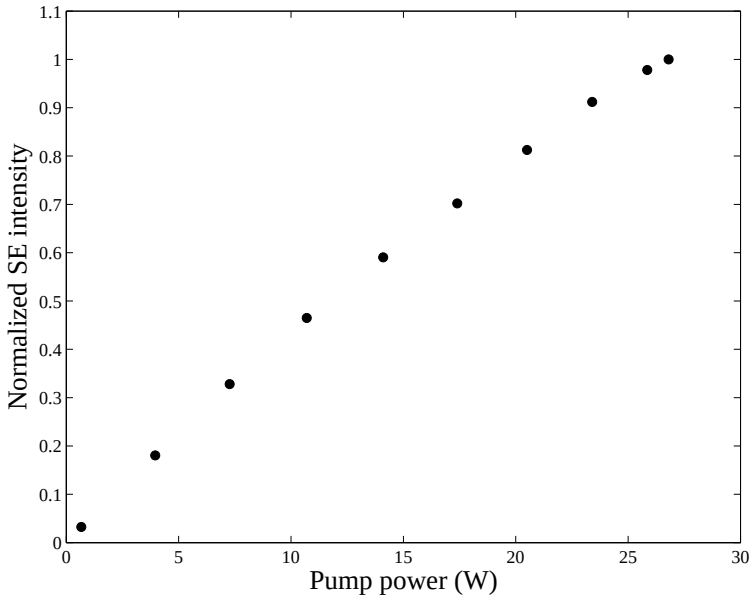

Figure 4.30: Measured result for normalized spontaneous emission (SE) intensity. The measurement is performed at the side of the crystal.

The comparison is relatively good, but again the only real significance lies in the mutual trend of an increasing ASE magnitude with larger input pump powers. The experimental results in Figure 4.30 are not compared to results from the simulation for reasons already discussed. In contrast to the measurements behind the crystal, the measured intensities at the side of the crystal are spontaneous emission and not ASE. The absence of ASE is expected since amplification of spontaneous emission occurs mainly in directions parallel to the optical axis. Early signs of saturation in the measured intensities at high input pump powers further strengthens the argument that ASE is absent.

In conclusion, the measured pump light transmission is compared to that obtained from the simulation in Figure 4.31. The pump light transmission provides for an useful comparison since it evaluates the quality in which the numerical simulation models absorption. The results compare very well, but differ noticeably in the high input pump power limit. For the last three numerical data points in particular, the difference between the experimental results and simulation is large. The numerically calculated transmission is found to drop below the 10% mark at an input pump power of 23.4 W, which is substantially lower than the calculated transmission obtained at a pump power of 20.5 W. The sudden drop in transmission is simply due to the change in wavelength and a corresponding rapid change in absorption cross section, as a result of the increasing pump power. The reason for the experimental results not showing this sharp change in transmission is a direct consequence of the fact that the pump wavelength, modeled as monochromatic in the simulation, has a finite bandwidth. The pump wavelength spectrum at full power and 24°C, obtained using a spectrometer, is given in Figure 4.32 and has a FWHM of approximately 4 nm. The finite bandwidth of the pump radiation causes the effect of a rapidly increasing absorption cross section to be less severe.

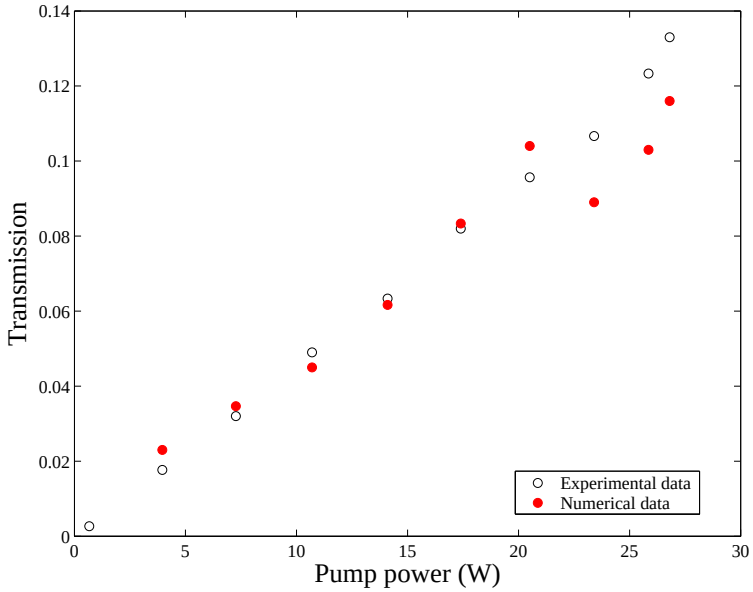

Figure 4.31: Comparison between pump light transmission predicted by simulation and experiment.

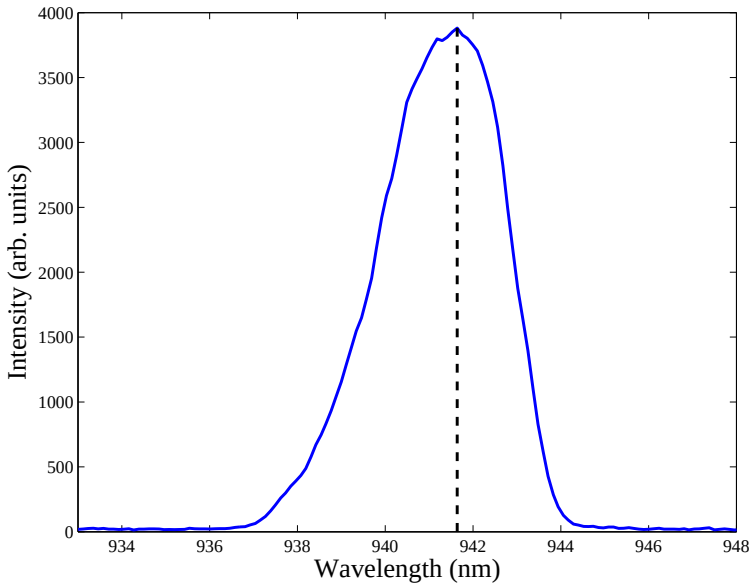

Figure 4.32: Diode wavelength spectrum at 24°C and full power (26.8 W).

Chapter 5

Conclusions

The aim of this research was to take the first steps in the design process of a solid-state amplifier. A numerical model was identified as an inexpensive method whereby different laser media could be compared in terms of their potential as amplifiers. To this end the equations forming the basis of the numerical model were chosen. The population rate equations were derived, clearly stating the relevant assumptions used in the process.

Adjustments made to the population rate equations enabled the CW numerical model to account for the effects of ASE and pump beam divergence. Predictions made by the simulation indicated premature gain saturation as a result of ASE. The numerical model was improved to incorporate transverse coordinates for the purpose of accurately modeling the probe beam. The addition of transverse coordinates provided the platform for modeling transverse gain saturation. Making use of an intuitive approach, the CW model was adapted into a time-dependent model, capable of simulating the gain experienced by an incident probe pulse.

The accuracy of the CW numerical model was evaluated experimentally. The simple amplifier, using Nd:YVO_4 as a gain medium, was designed, constructed and characterized in order to ensure compatibility with the assumptions made for the simulation. The comparison between the measured and simulated gain curves was good. Slight discrepancies between the measured and simulated results in the high input pump power limit were attributed to the presence of upconversion. An analytical model was used for the purpose of verifying the time-dependent model. The time-dependent model was subject to the same assumptions used in the analytical model for comparative purposes. Once again the agreement between the analytical and simulated results for the energy gain, experienced by a top hat input pulse, was good.

After it was established that the results from the numerical models may be trusted, the models were used as tools in the design of an Yb:YAG laser crystal. The design, subject to numerous requirements, was evaluated in terms of its amplifying and thermal properties. The effect of thermal loading on the front surface of the crystal was found to have a significant effect on the absorption coefficients (effective absorption cross sections), whilst the influence of these absorption coefficient changes had a relatively small effect on the power gain. The calculations furthermore illustrated the possibility of thermal fracture.

The designed crystals were also investigated using the time-dependent model, where it was assumed that the input pulse traverses the laser medium twice. For the case of the optimum crystal design, the pulse energy gain after two passes through the crystal was too little to reach the desired output pulse energy.

Due to the unfortunate absence of a probe source, the experimental evaluation of the Yb:YAG crystal was limited to a study of the spontaneous emission. The experimental results, obtained from the CCD camera, were in good agreement with those predicted by the CW simulation. These experimental results did not however, serve as a verification of the simulation due to the qualitative nature of the comparison. The agreement between the experimental and simulated results for the pump light transmission at high input powers was poor. This poor comparison was attributed to the infinitely narrow bandwidth that was used to simulate the pump wavelength.

For the purpose of verifying whether the CW numerical model correctly describes the amplification process in an Yb:YAG crystal, a probe source is required. The fact that the CW simulation predicted the appropriate gain dynamics for the Nd:YVO_4 medium, together with the qualitative agreement between the experimental and simulated results for the Yb:YAG medium, justifies the application of the CW numerical model as a design tool. The validity of the time-dependent model remains to be proven.

Future work may include the development of a mode-locked fibre source with an output in the spectral region corresponding to the peak emission cross section of Yb:YAG. Such a pulsed probe source will enable the verification of the time-dependent model, but will also identify ways in which the model may be improved.

In order to increase the output pulse energy from an Yb:YAG crystal to the mJ-range, a number of possible improvements can be made. The best way to ensure the maximum energy gain is by constructing a multi-pass amplifier. If more pump power is available, the energy gain can furthermore be increased by using a larger pump waist radius and ensuring better spatial overlap between the pump and probe beams. In the case of a higher input pump power it may well be necessary to explore longer gain media with lower dopant concentrations.

The CW numerical model can be improved in a number of ways:

- Include the effects of upconversion. Upconversion was identified with both the laser media investigated in this work and has the potential to decrease the gain considerably.
- Model the pump wavelength according to a finite bandwidth. An infinitely narrow bandwidth was found to give an incorrect representation of the absorbed pump power. Since the gain is proportional to the absorbed pump power, it is important to model the process of absorption as accurately as possible.
- Incorporate transverse coordinates for the pump beam. The transverse coordinates for both the pump and probe beams may then be modeled on a two-dimensional grid, simplifying the simulation algorithm and speeding up the numerical calculations.

With a minimum amount of effort, these improvements to the CW model should increase the accuracy of the predictions and will provide a more valuable design tool.

Appendix: Specifications of equipment used in experiments

A1) General equipment

Spectrometer

Ocean Optics HR4000CG-UV-NIR
The spectrometer was used to investigate the spectral properties of laser light and fluorescence.

- Detector: 3648-element linear CCD array
- Wavelength range: 200-1100 nm
- Optical resolution: 0.75 nm FWHM
- Software: *OOIBase32* Spectrometer operating software

Chiller

Neslab Endocal RTE-110
Two Chillers were used to regulate the temperature of the Nd:YVO_4 crystal and pump diodes in the experiment of Chapter 3. In Chapter 4, a chiller was again used to regulate the temperature of the Yb:YAG crystal.

- Work area: $5 \times 5 \times 5.75$ In. (length $\times$ width $\times$ depth)
- Temperature range: -30°C to 130°C
- Temperature stability: ± 0.1°C

CCD Camera

Coherent Auburn Division: LaserCam IIID
The CCD camera was used for beam diagnostics.

- Sensor active area: 6.4 mm (H) × 4.8 mm (V)
- Number of pixels: 736 (H) × 484 (V)
- Pixel pitch: 8.53 μm (H) × 9.84 μm (V)
- Signal to noise ratio: >55 dB
- Lens mount: C-mount
- Software: *LaserCam IIID* software support

Power meter

Coherent LM200 used with *Field Master GS*
The power meter was used to obtain the electro-optical properties of the diode modules and the Nd:YAG laser. It was also used to measure the probe gain in Figures 3.13 and 3.14.

Neutral density filters

HOYA NDX400
The neutral density filters were used to attenuate the laser beams for the protection of the CCD camera (or to prevent saturation).

A2) The Nd:YVO_4 experiment

Fibre-coupled diode module

JenOptik Laserdiode GmbH (JOLD 75-CPXF-2P)
The Fibre-coupled diode module was used to pump the Nd:YVO_4 gain medium.

- Central wavelength: 804.75 nm at 18°C
- Spectral bandwidth: 2.5 nm at 18°C (FWHM)
- Full power: 75 W

- Current at full power: 50.9 A
- Core diameter: 400 μm
- Fibre NA: 0.22
- Operation mode: CW

Nd:YAG laser

Lightwave Electronics: Model 221
The Nd:YAG laser was used as a probe source in the Nd:YVO_4 experiment.

- Central wavelength: 1064 nm
- Full power: 7.5 W
- Confocal parameter: <1.2 times diffraction limited
- Operation mode: CW

Power supply

Agilent Technologies 6573A
Two power supplies were used to drive the diode module and the Nd:YAG laser.

- Power: 2100 W
- Output voltage: 0-35 V
- Output current: 0-60 A

Lenses

R&G Co.
The lenses were used to obtain the required pump and probe beam waist sizes.

- *BK7 ϕ50 PCXf+75; AR1060, 808; i0°*
- *BK7 ϕ50 PCXf+200; AR1060, 808; i0°*

Mirror

R&G Co.
The mirror was used to co-align the pump and probe beams for transmission through the gain medium.

- *BK7 ϕ50 HRsp@1064 + HTsp@808; i45°*

A3) The Yb:YAG experiment

Fibre-coupled diode module

JenOptik Laserdiode GmbH (JOLD-30-FC-12-940)
The Fibre-coupled diode module was used to pump the Yb:YAG gain medium.

- Central wavelength: 938 nm at 25°C
- Spectral bandwidth: 4 nm at 25°C (FWHM)
- Full power: 30 W
- Current at full power: 47 A
- Core diameter: 200 μm
- Fibre NA: 0.22
- Operation mode: CW

Power supply

OsTech Diosource (DS11E)
The power supply was used to drive the diode module.

- Compliance voltage: 1.2-5 V
- Output current: 0-55 A
- Rise/Fall time: $<$30 μs

Thermo-electric cooler with temperature controller

TE Technology, Inc. Model TC-24-12
The thermo-electric cooler was used to regulate the temperature of the diode module. The proportional-integral (PI) control was optimized for the temperature region of interest.

- Maximum output current: 11.9 A
- Temperature range: -20°C to 100°C
- Uses *MP-2444* thermistor

CCD Camera

Hitachi Denshi (Europa) GmbH (KP-M2)
The CCD Camera was used for the fluorescence imaging in Chapter 4.

- Sensor active area: 6.45 mm (H) × 4.84 mm (V)
- Number of pixels: 768 (H) × 494 (V)
- Pixel pitch: 8.4 μm (H) × 9.8 μm (V)
- Signal to noise ratio: 56 dB
- Lens mount: C-mount
- Lens: Navitar TC-5028 50 mm telecentric lens (F/2.8)
- Software: *LabView VI (National Instruments)*

Lenses

All the lenses, except the *R&G Co.* lens, were used to obtain the required pump and probe beam waist sizes. The *R&G Co.* lens was used to gather the spontaneous emission from the crystal.
Thorlabs

- Aspheric *A397TM-B*: *TAC4 f+11; NA0.3; uncoated*

Edmund Optics

- *lens ACH-NIR 50×100*
- *lens ACH-NIR 50×150*
- *lens ACH-NIR 50×200*

R&G Co.

- *BK7 ϕ50 PCXf+75; AR1060, 808; i0°*

Mirrors

R&G Co.
The mirrors were used to discriminate against light at the pump wavelength to avoid saturation of the spectrometer.

- *BK7 D25×6 HRsp@(1040-1150) + HTsp@940/ARsp; i45°*
- *BK7 D25×6 HRsp@940 + HTsp@(1040-1150)/ARsp; i45°*

A4) Software

GLAD Ver.5.2

Applied Optics Research, Copyright, 1998-2005. All rights reserved.

LAS-CAD

LAS-CAD GmbH, Copyright, 1996-2006.

OSLO LT (OSLO EDU)

Lambda Research Corporation

MATLAB 6.5

The Mathworks, Inc. Copyright, 1994-2007.

Bibliography

[1] S. Balsamo. Dynamic beam propagation method for flared semiconductor power amplifiers. *IEEE Journal of selected topics in Quantum Electronics*, 2(2), June 1996.

[2] A. Dienes, J.P. Heritage, M.Y. Hong, and Y.H. Chang. Time- and spectral-domain evolution of subpicosecond pulses in semiconductor optical amplifiers. *Optics Letters*, 17(22), November 1992.

[3] Edeltraud Gehrig. Spatio-temporal dynamics of light amplification and amplified spontaneous emission in high-power tapered semiconductor laser amplifiers. *IEEE Journal of Quantum Electronics*, 37(10), October 2001.

[4] M.Y. Hong, Y.H. Chang, A. Dienes, J.P. Heritage, and P.J. Delfyett. Subpicosecond pulse amplification in semiconductor laser amplifiers: Theory and experiment. *IEEE Journal of Quantum Electronics*, 30(4), April 1994.

[5] M. V. D. Vermelho, Ulf Peschel, and J. Stewart Aitchison. Simple and accurate procedure for modeling erbium-doped waveguide amplifiers with high concentration. *Journal of lightwave technology*, 18(3), March 2000.

[6] A. Dienes, J. P. Heritage, C. Jasti, and M. Y. Hong. Femtosecond optical pulse amplification in saturated media. *Journal of the Optical Society of America B*, 13(4), April 1996.

[7] A. Icsevgi and W.E. Lamb. Propagation of light pulses in a laser amplifier. *Physical Review*, 185(2), September 1969.

[8] M. Wittmann, A. Penzkofer, and G. Gossl. Experimental and theoretical investigation of a multipass, plane mirror, femtosecond dye laser amplifier. *Applied Optics*, 34(24), August 1995.

[9] Mirvais Yousefi, Alberto Barsella, Daan Lenstra, Geert Morthier, Roel Baets, Stefan McMurtry, and Jean-Pierre Vilcot. Rate equations model for semiconductor lasers with multilongitudinal mode competition and gain dynamics. *IEEE Journal of Quantum Electronics*, 39(10), October 2003.

[10] M. Buhr and R. Fedosejevs, editors. *Proceedings of the 1999 IEEE Canadian Conference on Electrical and Computer Engineering: Computer Modelling of Solid State Laser Systems*, 1999.

[11] Richard Bellman, George Birnbaum, and William G. Wagner. Transmission of monochromatic radiation in a two-level material. *Journal of Applied Physics*, 34(4(1)), April 1963.

[12] Earl L. Steele and Walter C. Davis. Laser amplifiers. *Journal of Applied Physics*, 36(2), February 1965.

[13] D. Y. Shen, J. K. Sahu, and W. A. Clarkson. Highly efficient in-band pumped er:yag laser with 60w of output at 1645nm. *Optics Letters*, 31(6):754–756, March 2006.

[14] Gilbert L. Bourdet. Numerical simulation of a high-average-power diode-pumped ytterbium-doped yag laser with an unstable cavity and a super-gaussian mirror. *Applied Optics*, 44(6), February 2005.

[15] Jun Dong. Numerical modeling of cw-pumped repetitively passively q-switched yb:yag lasers with cr:yag as saturable absorber. *Optics Communications*, 226:337–344, September 2003.

[16] Gilbert L. Bourdet. Comparison of pulse amplification performances in longitudinally pumped ytterbium doped materials. *Optics Communication*, 200:331–342, October 2001.

[17] Gilbert L. Bourdet. Numerical simulation of the amplification of a short laser pulse by a ytterbium doped amplifier longitudinally pumped by short pump pulses. *Applied Optics*, 45(19), July 2006.

[18] Peter W. Milonni and Joseph H. Eberly. *Lasers*. John Wiley & Sons, 1988.

[19] Anthony E. Siegman. *Lasers*. University Science Books, 1986.

[20] A. E. Siegman. How to (maybe) measure laser beam quality. OSA TOPS, 1998.

[21] A. E. Siegman. Defining, measuring, and optimizing laser beam quality. In *Laser Resonators and Coherent Optics: Modeling, Technology, and Applications*. Proceedings of SPIE, January 1993.

[22] D.C. Jones and A.M. Scott. A model of a fibre amplifier incorporating amplified spontaneous emission. *Proceedings of SPIE*, 5335, 2004.

[23] L. Allen and G.I. Peters. Amplified spontaneous emission and external signal amplification. *Physical Review A*, 8(4), April 1973.

[24] G. Marowsky, F.K. Tittel, W.L. Wilson, and E. Frenkel. Laser gain measurements by means of amplified spontaneous emission. *Applied Optics*, 19(1), January 1980.

[25] Laura D. Deloach, Stephen A. Payne, L.L. Chase, Larry K. Smith, Wayne L. Kway, and William F. Krupke. Evaluation of absorption and emission properties of yb-doped crystals for laser applications. *IEEE Journal of Quantum Electronics*, 29(4), April 1993.

[26] Xuelu Zou and Hisayoshi Toratani. Evaluation of spectroscopic properties of yb-doped glasses. *Physical Review B*, 52(22), December 1995.

[27] R. John Koshel and I.A. Walmsley. Modeling of the gain distribution for diode pumping of a solid-state laser rod with nonimaging optics. *Applied Optics*, 32(9), March 1993.

[28] Takunori Taira, William M. Tulloch, and Robert L. Byer. Modeling of quasi-three-level lasers and operation of cw yb:yag lasers. *Applied Optics*, 36(9), March 1997.

[29] Mali Gong, Yanyang Yuan, Chen Li, Ping Yan, Haitao Zhang, and Suying Liao. Numerical modeling of transverse mode competition in strongly pumped multimode fiber lasers and amplifiers. *Optics Express*, 15(6), March 2007.

[30] A. Forbes, L.R. Botha, H.J. Strydom, F.J. Prinsloo, and E. Ronander. Beam perturbation through a mopa chain. In A. Lapucci and M. Ciofini, editors, *XIII International Symposium on Gas Flow and Chemical Lasers and High Power Lasers*, volume 4184, pages 386–489. Proceedings of SPIE, September 2000.

[31] Justin L. Blows. Heat generation in nd:yvo with and without laser action. *IEEE Photonics Technology Letters*, 10(12), December 1998.

[32] S. Pearce and C.L.M. Ireland. Performance of a cw-pumped nd:yvo4 amplifier with khz pulses. *Optics & Laser Technology*, 35:375–379, January 2003.

[33] M. J Esser. Diode-end-pumped solid-state lasers. Master's thesis, University of Stellenbosch, 2005.

[34] Christoph Czeranowsky. *Resonatorinterne Frequenzverdopplung von diodengepumpten Neodym-Lasern mit hohen Ausgangsleistungen im blauen Spektralbereich*. PhD thesis, Universität Hamburg, 2002.

[35] X. Wang, J. Song, H. Sun, and Z. Xu. Multiphoton-excited upconversion luminescence of nd:yvo4. *Optics Express*, 15(3):1384, February 2007.

[36] Y.F. Chen, L.J. Lee, T.M. Huang, and C.L. Wang. Study of high-power diode-end-pumped nd:yvo4 laser at 1.34 micro m: influence of auger upconversion. *Optics Communications*, 163:198–202, May 1999.

[37] Y.F. Chen, C.C. Liao, Y.P. Lan, and S.C. Wang. Determination of the auger upconversion rate in fibre-coupled diode end-pumped nd:yag and nd:yvo4 crystals. *Applied Physics B: Lasers and Optics*, 70:487–490, 2000.

[38] Lee M. Frantz and John S. Nodvik. Theory of pulse propagation in a laser amplifier. *Journal of Applied Physics*, 34(8), August 1963.

[39] Yi-Yuh Hwang, Chau-Hwang Lee, and Jyhpyng Wang. Dynamic model of multipass ultrashort-pulse laser amplifiers and its application. *Applied Optics*, 36(30), October 1997.

[40] C. LeBlanc, G. Grillon, J.P. Chambaret, A. Migus, and A. Antonetti. Compact and efficient multipass ti:sapphire system for femtosecond chirped-pulse amplification at the terawatt level. *Optics Letters*, 18(2), January 1993.

[41] W.H. Lowdermilk and J.E. Murray. The multipass amplifier: Theory and numerical analysis. *Journal of Applied Physics*, 51(5), May 1980.

[42] D. M. Pennington, D. Milam, and D. Eimerl. Gain saturation studies in lg-750 and lg-770 amplifier glass. *2nd Annual International Conference on Solid-State Lasers for Applications to Inertial Confinement Fusion*, 1997.

[43] Andrew M. Scott, Gary Cook, and Andrew P.G. Davies. Efficient high-gain laser amplification from a low-gain amplifier by use of self-imaging multipass geometry. *Applied Optics*, 40(15), May 2001.

[44] Chen Li, Qiang Liu, Mali Gong, Gang Chen, and Ping Yan. Modeling of end-pumped cw yb:yag lasers exhibiting non-uniform temperature distribution. *Optical and Quantum Electronics*, 36:745–758, April 2004.

[45] Falgun D. Patel, Eric C. Honea, Joel Speth, Stephen A. Payne, Ralph Hutcheson, and Randy Equall. Laser demonstration of ybag and materials properties of highly doped yb:yag. *IEEE Journal of Quantum Electronics*, 37(1), January 2001.

[46] Xiaodan Wang, Xiaodong Xu, Xionghui Zeng, Zhiwei Zhao, Benxue Jiang, Xiaoming He, and Jun Xu. Effects of yb concentration on the spectroscopic properties of yb:yag. *Spectrochimica Acta Part A*, 63:49–54, April 2006.

[47] David C. Brown, Rufus L. Cone, Yongchen Sun, and Randy W. Equall. Yb:yag absorption at ambient and cryogenic temperatures. *IEEE Journal of selected topics in Quantum Electronics*, 11(3), May 2005.

[48] G.J. Spühler, R. Paschotta, M.P. Kullberg, M. Graf, M. Moser, E. Mix, G. Huber, C. Harder, and U. Keller. A passively q-switched yb:yag microchip laser. *Applied Physics B: Lasers and Optics*, 72:285–287, February 2001.

[49] William F. Krukpe. New laser materials for diode pumped solid state lasers. *Current Opinion in Solid State and Materials Science*, 4:197–201, 1999.

[50] S. Chenais, F. Druon, S. Forget, F. Balembois, and P. Georges. On thermal effects in solid-state lasers: The case of ytterbium-doped materials. *Progress in Quantum Electronics*, 30:89–153, 2006.

[51] Walter Koechner. *Solid-state laser engineering*. Springer, 1999.

[52] T.Y. Fan. Heat generation in nd:yag and yb:yag. *IEEE Journal of Quantum Electronics*, 29(6), June 1993.

[53] Wenjie Xie, Young Kwon, Siu-Chung Tam, and Yee-Loy Lam. Diffraction losses of nd :yag and yb :yag laser crystals. *Optics & Laser Technology*, 33:129–134, January 2001.

[54] X. Peng, L. Xu, and A. Asundi. Power scaling of diode-pumped nd:yvo4 lasers. *IEEE Journal of Quantum Electronics*, 38(9), September 2002.

[55] Xiaodong Xu, Zhiwei Zhao, Jun Xu, and Peizhen Deng. Thermal diffusivity, conductivity and expansion of yb:yag single crystals. *Solid State Communications*, 130:529–532, March 2004.

[56] Shengzhi Zhao, Alexandra Rapaport, Jun Dong, Bin Chen, Peizhen Deng, and Michael Bass. Temperature dependence of the 1.03 micro m stimulated emission cross section of cr:yb:yag crystal. *Optical Materials*, 27:1329–1332, September 2005.

[57] David C. Brown. Nonlinear thermal and stress effects and scaling behavior of yag slab amplifiers. *IEEE Journal of Quantum Electronics*, 34(12), December 1998.

[58] M. Schmid, Th. Graf, and H.P. Weber. Analytical model of the temperature distribution and the thermal induced birefringence in laser rods with cylindrically symmetric heating. *Journal of the Optical Society of America B*, 17(8), August 2000.

[59] R. Weber, B. Neuenschwander, and H.P. Weber. Thermal effects in solid-state laser materials. *Optical Materials*, 11:245–254, January 1999.

[60] William H. Press, Saul A. Teukolsky, William T. Vetterling, and Brian P. Flannery. *Numerical Recipes in C: The Art of Scientific Computing*. Cambridge University Press, 1992.

[61] S.P. Timoshenko and J.N. Goodier. *Theory of Elasticity*. McGraw-Hill Book Company, 1970.

[62] A.K. Cousins. Temperature and thermal stress scaling in finite-length end-pumped laser rods. *IEEE Journal of Quantum Electronics*, 28(4), April 1992.

[63] John E. Marion. Appropriate use of the strength parameter in solid-state slab laser design. *Journal of Applied Physics*, 62(5), September 1987.

[64] Y.-F. Chen. Design criteria for concentration optimization in scaling diode end-pumped lasers to high power: Influence of thermal fracture. *IEEE Journal of Quantum Electronics*, 35(2), February 1999.

[65] NIST. Fracture toughness of yag..... Ceramics web book, http://www.ceramics.nist.gov/srd/summary/ftgyag.htm, 2001.

[66] Robert E. Fischer and Biljana Tadic-Galec. *Optical System Design*. McGraw-Hill, 2000.

[67] G. Boulon, L. Laversenne, C. Goutaudier, Y. Guyot, and M.T. Cohen-Adad. Radiative and non-radiative energy transfers in yb-doped sesquioxide and garnet laser crystals from a combinatorial approach based on gradient concentration fibers. *Journal of Luminescence*, 102-103:417–425, 2003.